



저작자표시-비영리-변경금지 2.0 대한민국

이용자는 아래의 조건을 따르는 경우에 한하여 자유롭게

- 이 저작물을 복제, 배포, 전송, 전시, 공연 및 방송할 수 있습니다.

다음과 같은 조건을 따라야 합니다:



저작자표시. 귀하는 원저작자를 표시하여야 합니다.



비영리. 귀하는 이 저작물을 영리 목적으로 이용할 수 없습니다.



변경금지. 귀하는 이 저작물을 개작, 변형 또는 가공할 수 없습니다.

- 귀하는, 이 저작물의 재이용이나 배포의 경우, 이 저작물에 적용된 이용허락조건을 명확하게 나타내어야 합니다.
- 저작권자로부터 별도의 허가를 받으면 이러한 조건들은 적용되지 않습니다.

저작권법에 따른 이용자의 권리는 위의 내용에 의하여 영향을 받지 않습니다.

이것은 [이용허락규약\(Legal Code\)](#)을 이해하기 쉽게 요약한 것입니다.

[Disclaimer](#)

공학박사 학위논문

**Design Sensitivity Analysis of
Nanomaterials considering
Uncertainties of Ensemble and Potential
Parameters**

앙상블과 포텐셜 변수들의 불확실성을 고려한
나노재료의 설계민감도 해석

2015년 8월

서울대학교 대학원

산업·조선공학부

김 현 석

**Design Sensitivity Analysis of
Nanomaterials considering Uncertainties of
Ensemble and Potential Parameters**

양상블과 포텐셜 변수들의 불확실성을 고려한
나노재료의 설계민감도 해석

지도 교수 조 선 호

이 논문을 공학박사 학위논문으로 제출함
2015년 8월

서울대학교 대학원
산업·조선공학부
김 현 석

김현석의 공학박사 학위논문을 인준함
2015년 6월

위 원 장 _____ (인)

부위원장 _____ (인)

위 원 _____ (인)

위 원 _____ (인)

위 원 _____ (인)

**Design Sensitivity Analysis of
Nanomaterials considering
Uncertainties of Ensemble and
Potential Parameters**

by

Hyun-Seok Kim

A dissertation submitted for the degree of
DOCTOR OF PHILOSOPHY

in the
Department of Industrial Engineering and Naval
Architecture
of
SEOUL NATIONAL UNIVERSITY, KOREA

August 2015

I dedicate this dissertation
to my family
to many friends
and
to God

Abstract

Hyun-seok Kim

Department of Industrial Engineering and Naval Architecture

College of Engineering

Seoul National University

A design sensitivity analysis (DSA) method considering uncertainty from ensemble and potential parameters in molecular dynamics (MD) is developed. By utilizing the first-order reliability method (FORM) concept based on the developed design sensitivity, impact of the uncertainty to both MD simulation and DSA of MD is evaluated efficiently and accurately. For practical application to nanoscale design problems, constant temperature MD simulation is considered under Nose-Hoover thermostat.

Recently, in both academic and industrial environment of naval architecture and ocean engineering, atomistic level simulation and design is essential to overcome the limits in conventional continuum based approach. It is well known that to study dynamical and thermo-dynamical properties of a system in real time by experimental approach at nanoscales is significantly difficult or impossible. However, the molecular dynamics simulations provide a suitable framework for elucidating physically complex phenomena at the atomic level with femtosecond resolution. Generally, uncertainty have a significant impact on observations and predictions in both simulation and design of nanomaterials. We identify the origin of uncertainty as ensemble and potential parameters. The uncertainty from ensemble parameters is inherently present in atomistic systems due to the random initial velocities. The potential parameter uncertainty arises when some parameters defining the

interatomic interactions in MD simulations are unknown. Normally, the influences of uncertainty to the MD simulation is evaluated through a tedious repetition of MD simulations with different initial conditions or by fitting the potential parameters to the desired bulk properties.

In this study, we perform the FORM analysis based on the developed analytical first and second order sensitivities with respect to random and design variables to evaluate the effect of uncertainty in MD simulation and DSA of MD. For accuracy and efficiency in the DSA of MD system, analytical sensitivity methods such as direct differential method (DDM) and adjoint variable method (AVM) are employed. The approximated DSA methods such as finite difference method (FDM) are impractical in nanoscale problems since MD simulations are highly nonlinear to design variables and computationally costly.

Various nanomaterial structures are applied in broad fields. For instance, nanoparticles are utilized for antifouling of marine structures. Through some numerical examples, the accuracy and efficiency of the developed DSA method considering the uncertainty is demonstrated for various nanoscale problems. The variances of performance measure in MD simulation and sensitivity due to the uncertainty is evaluated through FORM analysis based on the developed sensitivities. We further extend to a design optimization problem based on sensitivity to find unknown potential parameters between nanoparticle and nanostructure.

Keywords: Molecular Dynamics (MD), Ensemble Uncertainty, Potential Uncertainty, Nanomaterial, Design Sensitivity Analysis (DSA), Design Optimization

Student Number: 2008-21214

Contents

Abstract	i
Contents	iii
List of Tables	vii
List of Figures	x
Nomenclature	xiv
Chapter 1. Introduction	1
1.1 Motivation	1
1.1.1 Various applications of versatile nanomaterials	1
1.1.2 Uncertainty in molecular dynamics (MD) and nanomaterial design	5
1.1.3 Design sensitivity of molecular dynamics considering uncertainty	8
1.2 Purpose and Scope	11
1.3 Literature survey	15
1.3.1 Molecular dynamic simulations	15
1.3.2 DSA of transient dynamics	18
1.3.3 Reliability analysis	20
1.3.4 Applications of nanomaterials	21

1.3.5 Organizations of thesis	24
Chapter 2. Molecular Dynamics Simulations	25
2.1 Equation of motion.....	26
2.1.1 Lagrangian and Hamiltonian equations of motion	26
2.1.2 NVT ensemble.....	29
2.2 Interatomic potentials.....	32
2.2.1 Lennard-Jones (LJ) potentials	33
2.2.2 Embedded Atom Method (EAM) for metallic systems.....	34
2.2.3 Tersoff bond-order potential for covalent bond.....	38
2.2.4 Cut-off radius of potentials.....	39
2.3 Periodic boundary conditions.....	40
Chapter 3. Reliability Analysis	41
3.1 Descriptions of Random Variables	41
3.1.1 Mean Value.....	42
3.1.2 Variance and Standard Deviation	42
3.2 Probability Distributions	43
3.2.1 Normal Distribution	43
3.2.2 Lognormal Distribution.....	45
3.3 Limit State Function.....	47
3.4 Reliability Index.....	47
3.5 Second-Moment Theory of Reliability Analysis.....	47
3.5.1 Geometric measure of reliability.....	48

3.5.2 First-Order Reliability Moment (FORM) Method	54
Chapter 4. Design Sensitivity Analysis	57
4.1 Design sensitivity analysis of MD	57
4.1.1 Adjoint variable method for NVE ensemble	57
4.1.2 Adjoint variable method for NVT ensemble	60
4.1.3 Discontinuity problems introduced by cut-off	62
4.2 Design Sensitivity Analysis considering Uncertainty	71
4.2.1 FORM based approach.....	71
4.2.2 Design sensitivity considering uncertainty in MD simulation	72
4.2.3 Design sensitivity considering uncertainty in DSA of MD	73
4.3 Design sensitivity analysis for reliability analysis	75
4.3.1 Reliability based design sensitivity analysis	75
Chapter 5. Numerical Examples	78
5.1 Uncertainty effect in MD simulation.....	79
5.1.1 MD simulation of nanoparticle synthesis.....	80
5.1.2 Uncertainty effect to MD simulation of nanoparticle synthesis	86
5.1.3 Experiment of nanoparticle synthesis.....	93
5.2 Design optimization: unknown potential parameters	102
5.2.1 Optimization of nanoparticle-substrate force field parameters ...	103
5.2.2 Verification of developed design sensitivity.....	122
5.2.3 Uncertainties from random initial velocity	128
5.3 Atomic Mass Uncertainty: 3-D Gas Diffusion Problem.....	132

5.3.1 Verification of developed design sensitivity.....	133
5.3.2 Uncertainties from random atomic mass.....	136
5.4 1-Dimensional Harmonic Oscillator Problem.....	138
5.4.1 Verification of developed design sensitivity.....	141
5.4.2 Uncertainties from random initial velocity	144
5.4.3 Reliability based sensitivity analysis.....	148
5.5 Agglomeration of nanoparticles on a substrate	151
5.5.1 Experimental observation of nanoparticle agglomeration.....	151
5.5.2 Uncertainties from random initial velocity	156
5.5.3 Reliability based design sensitivity analysis	169
Chapter 6. Conclusions and Future Works	170
6.1 Conclusions	170
6.2 Future works.....	171
Bibilography	172
초 록	180

List of Tables

Table 5.1 Average of weighted mean diameters and error analysis.....	88
Table 5.2 Average of weighted mean diameters and error analysis for 5 independent MD simulations for representative cases	88
Table 5.3 Computation costs	89
Table 5.4 Mean particle size (nm) of AuNPs green synthesized using various concentrations of caffeic acid (mM)	96
Table 5.5 Pairwise force field parameters	106
Table 5.6 Harmonic bond force field parameters	106
Table 5.7 Harmonic angle force field parameters	107
Table 5.8 Comparison of initial and optimal design with mica model.....	110
Table 5.9 Comparison of optimization results with LAMMPS.....	110
Table 5.10 Comparison of initial and optimal force field parameters.....	110
Table 5.11 Optimization results.....	111
Table 5.12 Radius of gyration comparison.....	112
Table 5.13 Comparison of optimal designs with mica substrate model	115
Table 5.14 Computational cost comparison	115
Table 5.15 Comparison of optimization results.....	119
Table 5.16 Radius of gyration comparison.....	120
Table 5.17 Computational cost comparison	121
Table 5.18 Verification of random initial velocity design sensitivity (9,000-10,000 steps)	123

Table 5.19 Verification of design variable ε design sensitivity (9,000-10,000 steps)	124
Table 5.20 Verification of design variable σ design sensitivity (9,000-10,000 steps)	124
Table 5.21 Verification of 2 nd order analytical sensitivity (9,000-10,000 steps)	125
Table 5.22 Verification of random initial velocity design sensitivity (80,000-100,000 steps)	126
Table 5.23 Verification of design variable ε design sensitivity (80,000-100,000 steps)	126
Table 5.24 Verification of design variable σ design sensitivity (80,000-100,000 steps)	127
Table 5.25 Verification of 2 nd order analytical sensitivity (80,000-100,000 steps)	127
Table 5.26 Accuracy of FORM analysis for performance measure	130
Table 5.27 Accuracy of FORM analysis for sensitivity	131
Table 5.28 Verification of random initial velocity design sensitivity	134
Table 5.29 Verification of design variable ε design sensitivity	134
Table 5.30 Verification of second order analytical sensitivity.....	135
Table 5.31 Accuracy of FORM analysis for performance measure	137
Table 5.32 Accuracy of FORM analysis for sensitivity	137
Table 5.33 Comparison of computation cost.....	137
Table 5.34 Verification of random initial velocity design sensitivity	142
Table 5.35 Verification of second order analytical sensitivity.....	143

Table 5.36 Accuracy of FORM analysis for performance measure	146
Table 5.37 Accuracy of FORM analysis for sensitivity	147
Table 5.38 Comparison of computational cost.....	147
Table 5.39 Verification of design variable ε design sensitivity (80,000-100,000 steps)	150
Table 5.40 Verification of random initial velocity design sensitivity (9,000-10,000 steps)	159
Table 5.41 Verification of design variable ε design sensitivity (9,000-10,000 steps)	160
Table 5.42 Verification of design variable σ design sensitivity (9,000-10,000 steps)	160
Table 5.43 Verification of 2 nd order analytical sensitivity (9,000-10,000 steps)	161
Table 5.44 Accuracy of FORM analysis for performance measure	163
Table 5.45 Accuracy of FORM analysis for sensitivity	164
Table 5.46 Comparison of computational cost.....	165
Table 5.47 Verification of random initial velocity design sensitivity (80,000-100,000 steps)	166
Table 5.48 Verification of design variable ε design sensitivity (80,000-100,000 steps)	167
Table 5.49 Verification of design variable σ design sensitivity (80,000-100,000 steps)	167
Table 5.50 Verification of 2 nd order analytical sensitivity (80,000-100,000 steps)	168
Table 5.51 Verification of β sensitivity ($\Delta b=10^{-9}$ for FDM).....	169

List of Figures

Figure 1.1 Examples of studies on versatile nanomaterials	4
Figure 1.2 Uncertainty affecting the MD simulation result	7
Figure 1.3 Efficiency and accuracy in design sensitivity analysis	10
Figure 1.4 Variation of sensitivity affected by ensemble parameter uncertainty	10
Figure 1.5 Schematic figure of NVT ensemble.....	13
Figure 1.6 Examples of nanoparticles on a substrate and agglomeration	14
Figure 2.1 L-J potential (red), L-J force (green), and the derivative of force (blue).....	34
Figure 2.2 Graphs of the embedding energy $F(\rho)$, electron density $\rho(r)$, and pair potential $\phi(r)$ functions of copper which are obtained from the spline fitting. The green solid lines denote the corresponding derivatives. ...	37
Figure 2.3 Illustration of periodic boundary conditions.....	40
Figure 3.1 PDF and CDF of normal distribution.....	44
Figure 3.2 PDF and CDF of lognormal distribution	46
Figure 3.3 Linearization of limit state surface at arbitrary point.....	52
Figure 3.4 Hasofer and Lind reliability index	54
Figure 4.1 Switching function $S(r)$ ($r_l = 2.25$ and $r_u = 2.5$).....	65
Figure 4.2 Shifted and shifted-force potential and potential with switching function	65

Figure 4.3 Conservation of total energy	66
Figure 4.4 Comparison of the three numerical techniques. (top) potential (mid) force and (bottom) 1st order derivative of force	68
Figure 4.5 Diffusion of argon gas in NVE ensemble	69
Figure 4.6 Numerical study of design perturbation amount.....	70
Figure 5.1 Schematic of caffeic acid redox reaction.....	80
Figure 5.2 Randomly packed initial configuration of each cases: yellow, red, white, and blue corresponds to gold, oxygen, hydrogen, and carbon atoms, respectively	85
Figure 5.3 Measured average weighted mean diameters of gold nanoparticles with various number of reducing agent at 0.5 ns	89
Figure 5.4 Representative configurations at terminal time of MD simulation	92
Figure 5.5 Digital images of AuNPs. The final concentration of caffeic acid is (a) 0.008 mM, (b) 0.04 mM, (c) 0.08 mM, (d) 0.12 mM, (e) 0.16 mM, (f) 0.2 mM, (g) 0.24 mM, (h) 0.28 mM, (i) 0.4 mM, (j) 0.48 mM and (k) 0.56 mM. The concentration of Au ³⁺ ions is fixed at 0.2 mM. The detailed reaction procedure is described in the experimental section.....	95
Figure 5.6 Relationship between mean particle size (nm) and caffeic acid concentration (mM).....	96
Figure 5.7 HR-TEM images of AuNPs. The final concentration of caffeic acid is (a) 0.008 mM, (b) 0.04 mM, (c) 0.08 mM, (d) 0.12 mM, (e) 0.16 mM, (f) 0.2 mM, (g) 0.24 mM, (h) 0.28 mM, (i) 0.4 mM, (j) 0.48 mM and (k) 0.56 mM. The scale bar for each image represents 100 nm (left) and 10 nm (right)	100
Figure 5.8 HR-TEM and MD simulation images of AuNPs. The final TEM image of caffeic acid is (a) 0.04 mM, (b) 0.12 mM, (c) 0.24 mM, (d) 0.24 mM and (e) 0.28 mM and final MD atomic configuration is (f) 1 OXCA, (g) 3	

OXCAs, (h) 6 OXCAs, (i) 10 OXCAs and (j) 24 OXCAs. The scale bar for each image represents 100 nm and 10 nm.....	101
Figure 5.9 Qualitative comparison of (a) experiment and (b) MD simulation	101
Figure 5.10 Two models of a gold nanoparticle on a substrate	106
Figure 5.11 Gold nanoparticle after 10,000 steps of MD simulation	109
Figure 5.12 Optimization history of objective function	111
Figure 5.13 Time history of gold nanoparticle potential energy of initial and optimal design of potential wall and mica substrate model	112
Figure 5.14 Time history of radius of gyration of initial and optimal design of potential wall and mica substrate model	113
Figure 5.15 Time history of gold nanoparticle potential energy of optimal designs and mica substrate model	115
Figure 5.16 Comparison of 116 and 959 gold atoms mica substrate model..	118
Figure 5.17 Optimization history of objective function	119
Figure 5.18 Time history of gold nanoparticle potential energy of initial and optimal design of potential wall and mica substrate model	120
Figure 5.19 Time history of radius of gyration of initial and optimal design of potential wall and mica substrate model	121
Figure 5.20 Performance measure histogram of 1,000 MD simulations and its normal distribution graph.....	130
Figure 5.21 Sensitivity histogram of 1,000 MD simulations and its normal distribution graph	131
Figure 5.22 Initial configuration of 3-dimensional gas atoms	133
Figure 5.23 1-D harmonic oscillator with impulse at the center	138

Figure 5.24 Displacement profile of 1-dimensional harmonic oscillator.....	140
Figure 5.25 Performance measure histogram of 1,000 MD simulations and its normal distribution graph.....	146
Figure 5.26 Sensitivity histogram of 1,000 MD simulations and its normal distribution graph	147
Figure 5.27 Morphology observation of AuNPs with various microscopes	154
Figure 5.28 Morphology observation of AgNPs with various microscopes	156
Figure 5.29 Cold welding of gold nanoparticles on a potential wall substrate	159
Figure 5.30 Performance measure histogram of 1,000 MD simulations and its normal distribution graph.....	163
Figure 5.31 Sensitivity histogram of 1,000 MD simulations and its normal distribution graph	164

Nomenclature

ε	Energy depth in LJ potential
λ	Adjoint variable vector
σ	Collision diameter in LJ potential
$\Phi^m(\mathbf{r}_i, \mathbf{r}_j, \dots)$	m -body potential
$\Phi(r)$	Pair-wise potential
$\Phi^h(r)$	Harmonic potential
$\Phi^{\text{cut-off}}(r)$	Cut-off radius potential
ψ	Performance measure
\mathbf{b}	Design variable vector
b_i	i -th design variable
\mathbf{f}	Inter-atomic force vector
H	Hamiltonian
L	Lagrangian
m_α	Mass matrix of an atom α
m_A	Atomic mass
\mathbf{n}	Lattice site vector
n_a	The number of atoms
n_d	The number of dimension
p_α	Generalized momentum
r	Distance between two atoms
r_{ij}	Distance between atoms i and j

\mathbf{r}_i	Position vector of atom i
r_{cut}	Cut-off radius
$U(\mathbf{r}_1, \mathbf{r}_2, \dots, \mathbf{r}_N)$	Inter-atomic potential energy
$F(r)$	Inter-atomic force
k_B	Boltzmann constant
T	Temperature
ξ	Thermostat variable
\mathbf{x}	Random variable vector
$(\dot{\bullet})$	Time derivative
$(\bullet)'$	First order design variation
AFM	Atomic Force Microscopy
AgNP	Silver Nanoparticles
AuNP	Gold Nanoparticles
AVM	Adjoint Variable Method
CDF	Cumulative Distribution Function
CNT	Carbon Nanotube
DDM	Direct Differentiation Method
DSA	Design Sensitivity Analysis
FCC	Face Centered Cubic
FDM	Finite Difference Method
FE-SEM	Field Emission Scanning Electron Microscopy
FORM	First-Order Reliability Method
HR-TEM	High Resolution Transmission Electron Microscopy
MD	Molecular Dynamics
NP	Nanoparticle
NW	Nanowire
PDF	Probability Density Function

Chapter 1. Introduction

1.1 Motivation

1.1.1 Various applications of versatile nanomaterials

Development of new materials with extraordinary and outstanding performance leads to the improvement of engineering devices. A study of the mechanical properties of nanoscale materials has been of significant interest to researchers due to nanotechnological development. Nanomaterials such as nanoparticles, nanowires, and nanotubes have a potential to exhibit extraordinary combinations of properties. Due to their remarkable mechanical, electrical, thermal, and magnetic properties, nanomaterials have drawn considerable attention to the scientific community for the past decades.

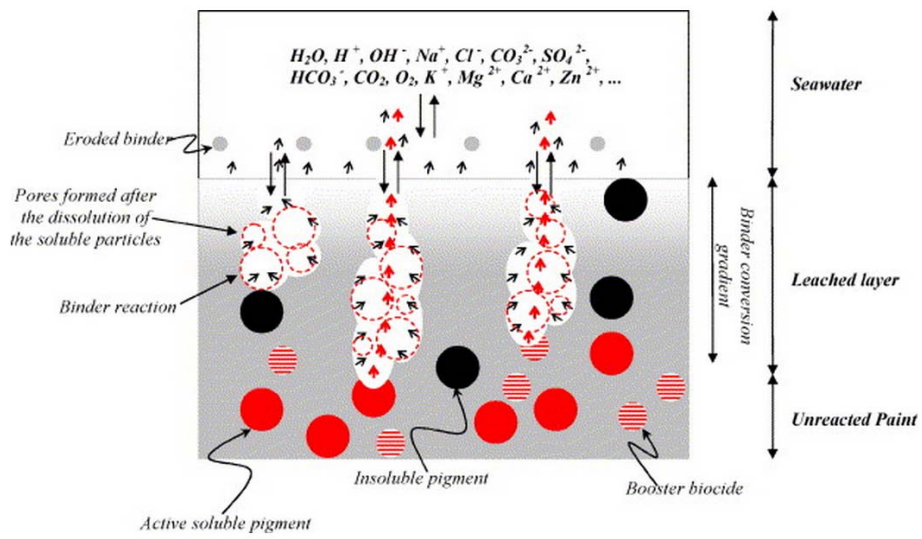
Nanoparticles have been used in a variety of research fields, including drug delivery, catalysis, biosensing and antifouling, due to their numerous potential applications. Nanoparticles possess numerous advantages, such as low cytotoxicity, facile modification of their surfaces, straightforward synthetic processes, and excellent biocompatibility. Especially in naval architecture and ocean engineering, by releasing of several biocides embedded in a film-forming nanocomposites, antifouling can be achieved by slowing the growth of subaquatic organisms as shown in Figure 1.1-(a). Furthermore, by varying the size, shape, and coverage of the nanoparticles, nanoparticles can be used to control the efficiency of drug delivery.

There have been many researches made on the temperature and strain-rate effects on nanoscale wires. It is known that the Young's modulus, fatigue stress, tensile strength and buckling mode of nanowires can be significantly modified under the temperature and size control in nanoscale by utilizing molecular dynamics simulations. Extremely high strain rate effect is expected on the mechanical properties of nanowires with different cross-sectional sizes.

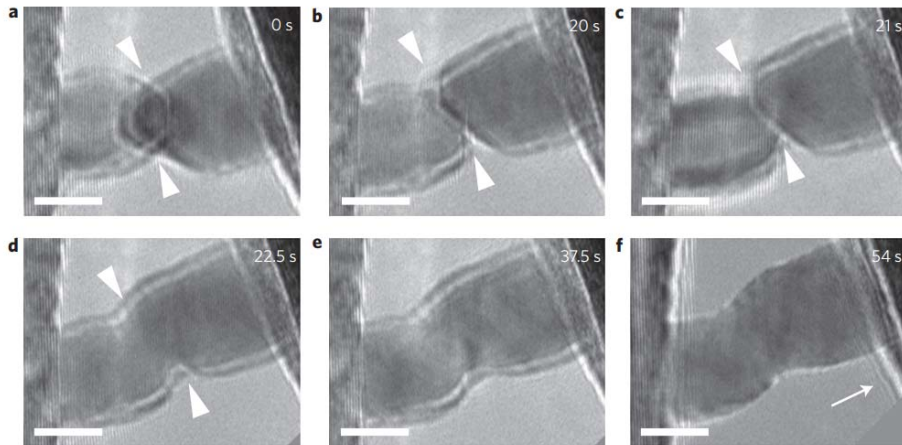
In nanoscale experiment, it is shown that the thin gold and silver nanowires can be welded under low applied pressures, ambient temperature, and ambient atmospheres (Figure 1.1-(b)).

Since Iijima (1991) first discovered carbon nanotubes (CNTs) in 1991, it has become an important material in thermal sciences. A significant amount of effort has been put into the theoretical and experimental study of these structures. There is immense interest in nanoscale graphitic structures and CNTs not only for their mechanical and electrical properties, but also for their thermal properties, which are fundamentally important in controlling system performance. Thermal conductivity of a single-walled CNT has been reported to be extremely high as 6000 W/m K at room temperature. However, extremely low thermal conductivities of CNTs are discovered when the CNTs have certain chirality, isotope impurity, and defects as shown in Figure 1.1-(c). By controlling the characteristics, it is possible to utilize CNTs in both very efficient thermal conductor and thermal insulation materials.

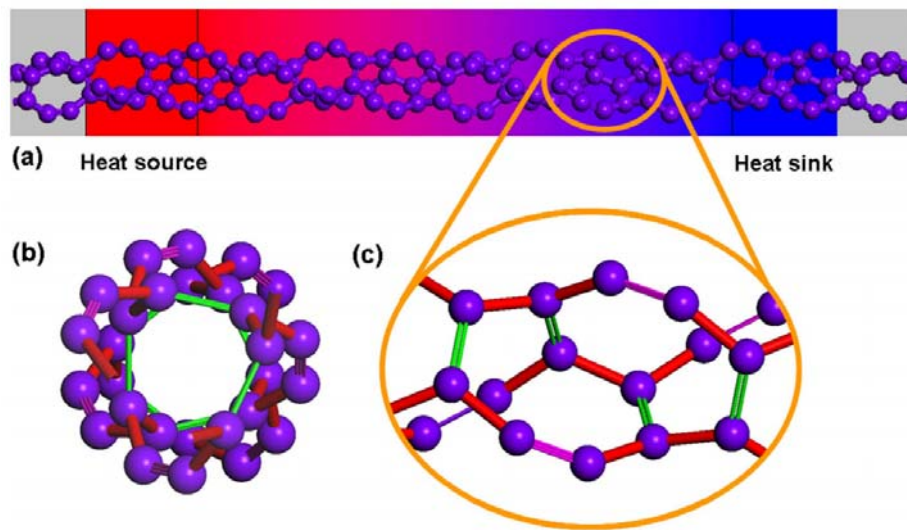
As above mentioned, the size and morphology of nanomaterials play crucial roles in controlling the physical, chemical, optical and electronic properties. Therefore, we develop an analytical design sensitivity analysis method of MD simulations considering uncertainty. For its applications to the practical nanomaterial design, we employ the constant temperature MD simulation by using Nose-Hoover thermostat. Further extension to the design optimization problems of nanomaterials are formulated and solved using gradient based optimization algorithm.



(a) antifouling of organisms using nanoparticles (Yebra et al., 2004)



(b) cold welding of gold nanowires (Lu et al., 2010)



(c) low thermal conductivity of CNT with reconstructed structure (Zhu and Li, 2014)

Figure 1.1 Examples of studies on versatile nanomaterials

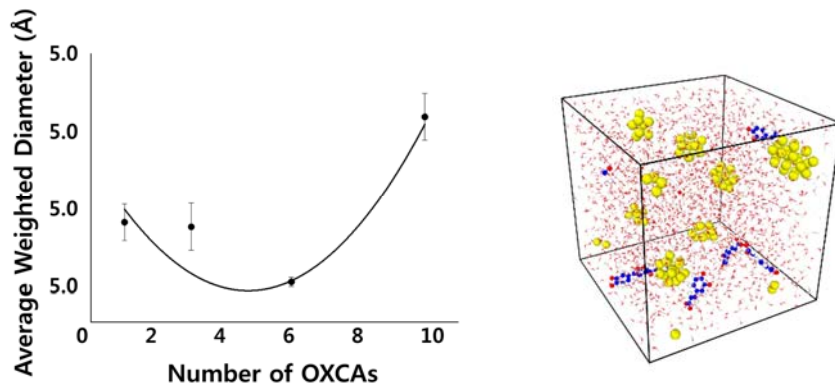
1.1.2 Uncertainty in molecular dynamics (MD) and nanomaterial design

In recent years, interest in the molecular dynamics (MD) analysis methods has rapidly increased and the MD based simulations have been one of the first choice of researchers in a large variety of fields to overcome the limits of conventional continuum based approach. Furthermore, due to the increasing computational performance and development of various efficient parallel computing methods, the molecular dynamics simulations are now widely utilized in academic and industrial environments to study a large variety of mechanical, chemical, and biological systems.

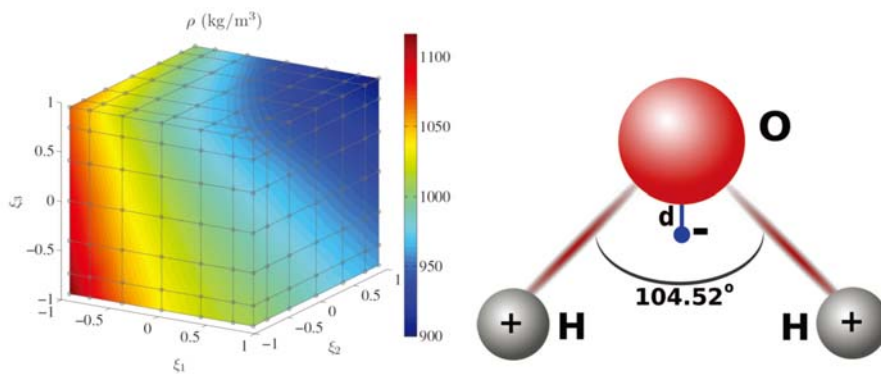
In general, it is well known that to study dynamical and thermodynamical properties of a system in real time by experimental approach in a nano- or macro-scales is significantly difficult or even impossible. On the other hand, the molecular dynamics simulations provide a suitable framework for exploring and elucidating physically complex phenomena at the atomic level with femtosecond resolution. However, the success of such atomic level simulations is partially limited by the accessible length and time scales due to the large computational cost, thus constraining the analysis to relatively small systems and short times compared to experimental approach.

In most of situations, uncertainty may have a huge impact on observations or predictions in the simulation and also in the design of nanomaterials. We can identify the main sources of uncertainty in three categories: ensemble parameters, potential parameters, and configurations in design of nanomaterials. The uncertainty from ensemble parameters is inherently present in atomistic systems due to the random initial velocities which are scaled from the initial temperature. A different source of uncertainty is potential parameter uncertainty which arises when some parameters defining the interatomic interactions in the molecular dynamics simulations are not precisely known or due to the empirical nature of fitting the force field parameters to experimental observations. The other uncertainty comes from the randomness in configuration when designing the nanomaterials with arbitrary locations.

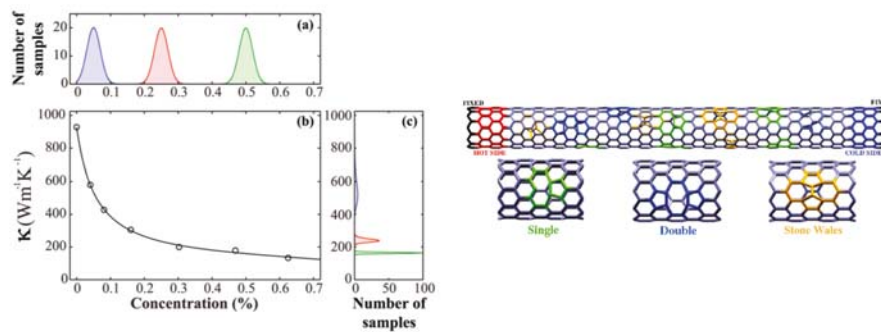
Representative examples of uncertainties from ensemble parameters, potential parameters, and configuration in nanomaterial design affecting on the results of molecular dynamics simulations are shown in Figure 1.2. The standard error analysis results in Figure 1.2-(a) shows the effect of ensemble parameter uncertainty, meaning different random initial velocities, on the average of weighted mean diameters of gold nanoparticles aggregated at various reducing agent concentration. Figure 1.2-(b) presents the 3D functional plot of molecular dynamics simulation predictions of water density with potential parameter uncertainty in TIP4P water molecule model parameterized by ξ (Sevik et al., 2011). In Figure 1.2-(c), uncertainty from the configuration in the design of carbon nanotube (CNT) is shown. We can see that the randomness in the concentration and the location of defects in carbon nanotube significantly influence the thermal conductivity value and its distribution (Rizzi et al., 2012). To quantify the effect from these uncertainties, as shown through several examples, a sufficient series of molecular dynamics simulations are necessary with corresponding conditions. As mentioned above, one of the weakness of molecular dynamics simulation is the large computational cost. Therefore, a development of an efficient and accurate method to predict the influence of the uncertainty in atomic level simulations is essential.



(a) Uncertainty from ensemble parameters



(b) Uncertainty from potential parameters (Rizzi et al., 2012)



(c) Uncertainty from configuration in nanomaterial design (Sevik et al., 2011)

Figure 1.2 Uncertainty affecting the MD simulation result

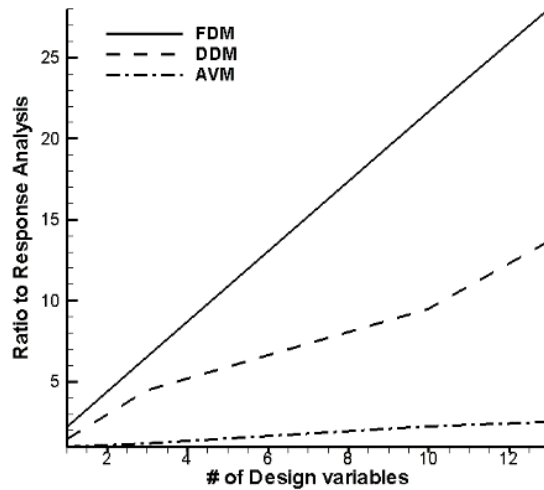
1.1.3 Design sensitivity of molecular dynamics considering uncertainty

Design sensitivity analysis (DSA) aims to describe how much model output values are affected by the changes in the model input values. To facilitate the merits of molecular dynamics simulation methods in multidisciplinary, a further extension to an efficient and accurate design optimization based on the sensitivity at the atomistic level is crucial for designing new materials and investigating physically complex phenomena.

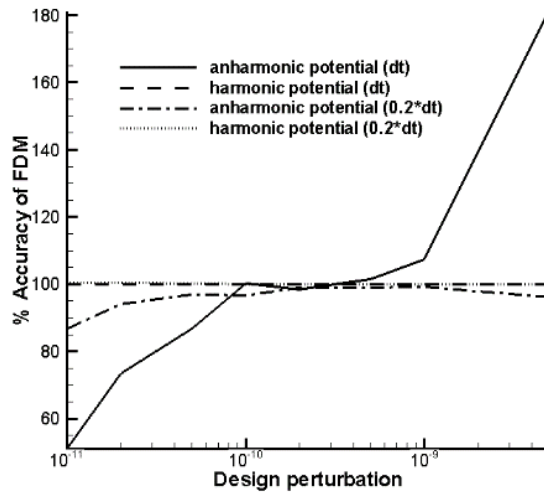
In general, an expansive computational cost is expected for the molecular dynamics simulations since they are transient dynamic problems. Moreover, when large number of the design variables are considered, a tremendous computational cost is asked for the approximated DSA methods such as the finite difference method (FDM) due to repetition of the analysis procedure. In addition to the efficiency problem, it is impractical from the viewpoint of accuracy since the MD simulations usually include highly nonlinear design parameters. For example, consider an MD simulation of a 1-dimensional atomic chain. Performance measure is time averaged temperature. Design variables are selected as the collision diameters of Lennard-Jones (LJ) potential, just for the demonstration purpose. Figure 1.3-(a) shows the comparison of design sensitivity computational costs between the FDM, an analytical direct differentiation method (DDM), and another analytical adjoint variable method (AVM). It turns out that the AVM is the best choice for the efficiency in design sensitivity analysis when the number of design variables is large. In the accuracy point of view, as shown in Figure 1.3-(b), when we employ an anharmonic potential, which is highly nonlinear with respect to the design variables, the approximated design sensitivity obtained from FDM is extremely sensitive to design perturbations compared to the harmonic potential case. Too much or too less design perturbations in the FDM might lead to an inaccurate design sensitivities analysis results. Therefore, to perform an efficient and accurate design sensitivity analysis in atomistic level, an analytical DSA method is essential.

Furthermore, as same as in the analysis with molecular dynamics

simulation, the design sensitivity in MD is also affected from the uncertainties. To perform a molecular dynamic simulation, a specification of initial velocities for all particles in the system is necessary. The velocities of all particles in the system may be set to random values corresponding to a certain initial temperature. Figure 1.4 shows the distribution of sensitivities in molecular dynamics due to the uncertainty in ensemble parameter, the random initial velocity. Alike to the molecular dynamics simulation, a development of efficient and accurate prediction method to estimate the effect from the uncertainty to design sensitivity is essential.



(a) Comparison of computation costs for design sensitivity analysis in MD



(b) Accuracy of FDM sensitivity for harmonic and anharmonic cases
 Figure 1.3 Efficiency and accuracy in design sensitivity analysis

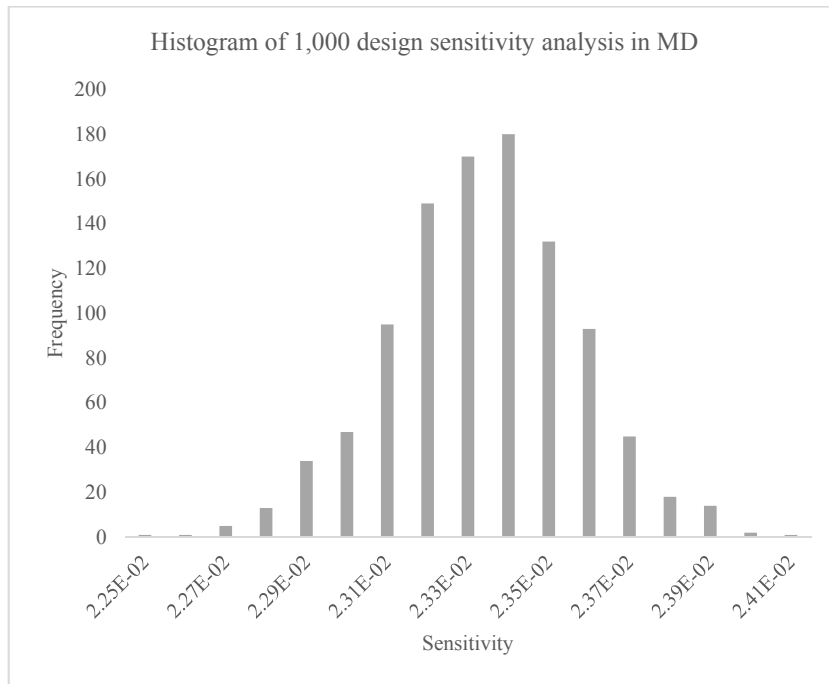


Figure 1.4 Variation of sensitivity affected by ensemble parameter uncertainty

1.2 Purpose and Scope

In the fields of naval architecture and ocean engineering, a demand for designing new nanomaterials with extraordinary and outstanding performance has never been so high. This is because the limit of continuum based approach for such problems as corrosion, fracture, thermal induced deformation in welding process, and antifouling. The continuum based approach cannot capture and represent the physical complexity in such phenomena. To overcome and to elucidate these problems, atomistic level analysis method such as molecular dynamic simulation is inevitable. Also, nanomaterials such as nanotubes, nanowires, and nanoparticles have a potential for applications in the field of marine engineering due to their remarkable mechanical, chemical, electrical, thermal, and magnetic properties. For instance, organisms such as algae and barnacles sticking on the lower structure of ships influences the propulsion power by increasing the ship resistance. This might not be too serious on small boats and yachts. However, for large sized ships such as cruisers, tankers, carriers and container, which frequently crosses all over the world, it is a major problem in engineering, economic, and environmental point of view. A commonly employed remedy for the problems occurred by the adhesion of foreign substances is to move the ship to a dry dock and remove all debris on the surface at the lower part of the vessel. This procedure causes enormous cost since the ship is unable while in maintenance. Furthermore, as time goes on, after scraping the debris, the resistance of the ship again increases due to the adhesion of biofouling resulting a decrease in the propulsion efficiency. Even with a small increase in the portion of resistance, it may severely damage the economic feasibility in ship operations since a container ship with 140,000 gross ton consumes about 1,000kg of fuel per an hour. To overcome the economic lost and maintain the propulsion efficiency of the ship, a new coating method is employed in the maritime industry which utilizes nanomaterials such as manganese oxide polystyrene nano-composite, zinc oxide polystyrene nano-composite, silica nano-coating, and carbon nano-tube structures.

The purpose of this research is to develop an efficient and accurate design sensitivity analysis method to evaluate the effect of uncertainty from ensemble and potential parameters in both MD simulation and DSA of MD. Such method can save tremendous computation cost from numerous repetition of MD simulations and DSA of MD to insure the results due to the uncertainties. This research can be a cornerstone to the further extension in designing nanomaterials which have variety of applications in naval architecture and ocean engineering.

In practical nanoscale systems, thermal effects are very important. Furthermore, the random initial velocity is closely related to the desired initial temperature. In this point of view, we need to consider a statistical concept to deal with macroscopic behaviors due to the variations of microscopic variables since there are numerous cases for the microscopic states that can represent identical macroscopic properties (Frenkel and Smit, 2001). A canonical ensemble is used to represent the possible states of a system which is in thermal equilibrium with a heat bath so that the resulting temperature is constant as shown in Figure 1.5. The thermodynamic variables of the canonical ensemble are the number of particle N , the volume V , and the temperature T , therefore, the canonical ensemble is called the NVT ensemble since each of these three quantities is fixed. Several approaches for MD simulations in NVT ensemble have been proposed by researchers to maintain the desired temperature of a system. To develop a DSA method of constant temperature MD simulation, the Nose-Hoover thermostat is introduced since it is known that the correct canonical distribution in phase space can be obtained the proper way by using that method.

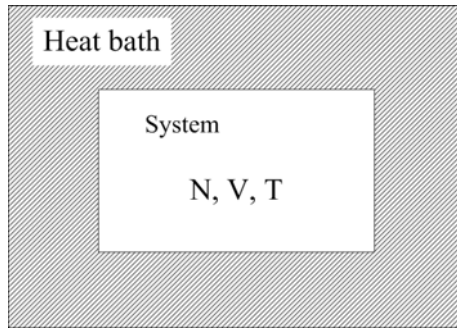
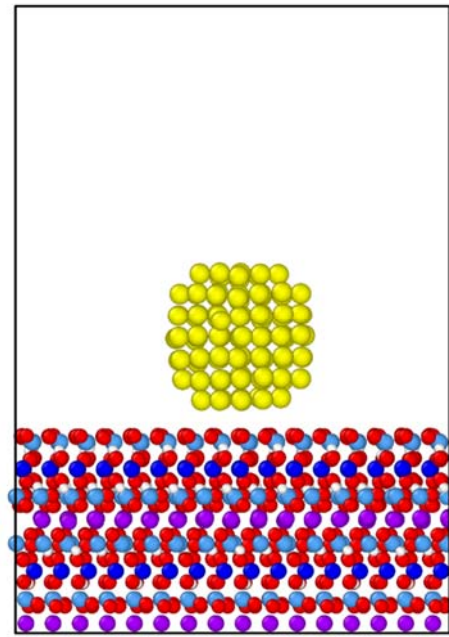
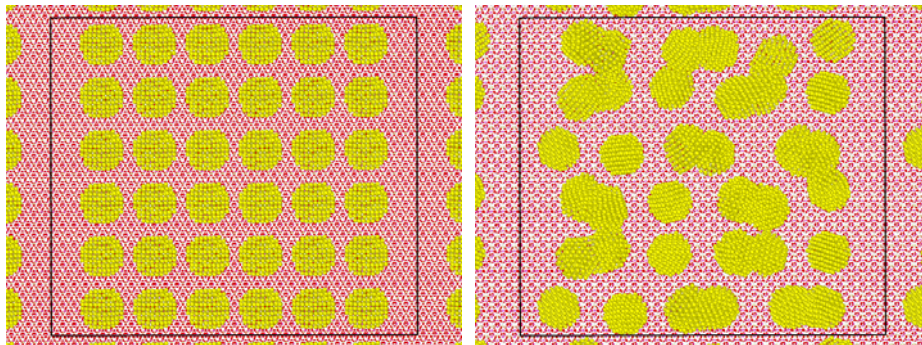


Figure 1.5 Schematic figure of NVT ensemble

In this research, among various nanomaterials, we focus on the metallic nanoparticle problems and agglomeration phenomenon as shown in Figure 1.6. For the MD simulation of metallic nanoparticles, the Embedded Atom Method (EAM) is widely utilized to describe the interaction between atoms since the EAM potential is known to be suitable for the metallic system due to the local electron density consideration in that potential. We perform the developed DSA method for the MD simulations of a gold nanoparticle on a substrate system and agglomeration of gold nanoparticles to investigate the influences of the uncertainty in ensemble and potential parameters to the prediction and observation in MD simulations are analyzed. The effect of uncertainty in MD simulations is estimated by utilizing first-order reliability method (FORM) analysis based on the developed analytical first order sensitivity of random variables. For the assessment of uncertainties in DSA of MD, we employ the developed analytical first and second order sensitivities with respect to the random and design variables in same concept. The uncertainty from the potential parameters is taken into account for the interactions between the substrate and the nanoparticles. More precisely, by solving an design optimization problem based on the developed design sensitivity, a proper force field parameters is proposed which replaces the interactions between a structurally complex and computationally costly substrate structure and nanoparticles.



(a) gold nanoparticle on a mica substrate



(b) agglomeration of gold nanoparticles on a mica (top view)

Figure 1.6 Examples of nanoparticles on a substrate and agglomeration

1.3 Literature survey

1.3.1 Molecular dynamic simulations

The MD simulation is the most famous tool in investigating mechanical behaviors. It is used to describe the instantaneous atomic behavior of material systems. It is a deterministic numerical solution of Newton's equations of motion for the system of particles. In thermo-dynamics and physical chemistry, the average thermo-chemical properties is the most interesting thing rather than individual atomic motions, since random variables are included in the simulations. We obtain an average of all possible states on the system by using random variables as ensemble average. In realistic simulation, we can take a time average instead of an ensemble average by the ergodicity assumption (Frenkel and Smit, 2001). This is based on the intuition that every particle can visit all the states for a sufficient amount of time.

The interaction between atoms can be described by inter-atomic potentials. There are various kinds of inter-atomic potentials according to bonding and interaction types between the atoms. The most simple and famous one is the Lennard-Jones (LJ) potential which describes the pair-wise interaction (Jones, 1924a, Jones, 1924b), which is composed of the repulsion and attraction of atomic interactions having two parameters such as a collision diameter and an energy depth. Tersoff (1986) developed multi-body potentials for covalent materials to consider the bonding order of atoms. He got the parameters of potentials for silicon (Tersoff 1988a) and carbon (Tersoff 1988b). For metallic systems, the embedded atom method (EAM) works well (Daw et al. 1993). To describe the metallic bonding, the embedding energy, which means the amount of energy required to insert one atom into the electron gas of a given density, are used. The potential includes this embedding energy and electro-static Coulomb interaction energy.

The simulated system using the MD is usually treated as an isolated system with conservation of total energy, since the equations of motion follow

Hamiltonian. However, it is convenient to keep the temperature constant in real experiments. Therefore performing constant temperature MD simulation is of great importance for the investigation of physical, chemical and biological problems. Several approaches have been proposed for this purpose. Since the temperature is related to the kinetic energy, the velocities of atoms in the system must be rescaled in order to maintain the temperature at the desired value. One crude way is to directly rescale the velocities at each time step or after a certain number of time steps. However, this direct velocity rescaling does not sample the phase space in the proper way as prescribed for a canonical ensemble since the condition of constant temperature is not equivalent to the condition that the kinetic energy per atom is constant from a statistical mechanical point of view (Frenkel and Smit 2002). Andersen (1980) proposed a constant temperature MD simulation method which is a hybrid of MD and Monte Carlo (MC) methods since the velocities of the atoms are changed by stochastic collision to induce Boltzmann distribution. The stochastic collisions introduce drastic change to the dynamics in a way that is not realistic, and it also lacks a well-defined conserved quantity. In the Berendsen method (Berendsen 1984), the velocities of atoms are rescaled more gradually than the Anderson method. The thermostat suppresses fluctuations of the kinetic energy of the system and therefore cannot generate a correct canonical ensemble rigorously. Based on the extended Lagrangian approach which is introduced by Andersen (1980), Nose introduced an extended Hamiltonian which consists an additional degree of freedom of the heat bath that acts as a time scaling factor (Nose 1984a, b). Nose's method is simplified by Hoover (1985) by introducing a thermodynamic friction coefficient. Hoover's formulation of Nose's method is so-called the Nose-Hoover thermostat. If an ergodic dynamic behavior is assumed, the correct canonical distribution can be obtained by utilizing the Nose-Hoover thermostat. However, for small or stiff systems, the Nose-Hoover dynamics is not ergodic (Hoover 1985; Tuckerman et al. 2001). Martyna and co-workers (Martyna et al. 1992; Tobias et al. 1993) proposed the Nose-Hoover chain method in order to fix these problems. However, for the system that is large enough to be sufficiently chaotic, the ergodicity is guaranteed so that the

performance of Nose-Hoover thermostat is usually satisfactory (Frenkel and Smit 2002). The generalized Langevin equation (GLE) proposed by Adelman and Doll (1974, 1976) is also used for the constant temperature MD simulation (Ceriotti et al. 2009; Evstigneev and Reimann 2010). The random force and frictional force in the GLE are balanced to maintain the desired system temperature (Hu and Sinnott 2004; Kim et al 2013).

To reduce the computation of MD simulations to the locally confined region of interest considering the effect of surrounding, reduced MD models are proposed. In such reduced MD models, it is very important to impose the appropriate boundary conditions that could replace the effect of eliminated degrees of freedom (DOFs) and to suppress the spurious wave reflections at the interface between the domain of interest and the outer region. Holian and Ravelo (1995) imposed uniaxial and homogeneously expanding periodic boundary conditions on a simulation box that can be expanded according to initial strain rate to prevent unrealistic wave reflection in crack propagation problems. Adelman and Doll (1974, 1976) tried to eliminate the unnecessary atomic DOFs to analyze inelastic atomic motion when gas collisions occur in a solid surface. They derived the generalized Langevin equations (GLE), where the effects of the eliminated atoms are treated at the boundary as a damping force consisting of a damping kernel matrix and the velocity of atoms. Wagner and Liu (2003) employed the damping kernel matrix terms as a dynamic multiscale boundary condition to prevent the wave reflection of fine scale at the molecular-continuum boundaries. However, the analytical damping kernel function is only available for one-dimensional problems and its size should be equal to the eliminated number of DOFs. Cai et al. (2000) calculated each term of damping kernel matrix numerically, performing several MD simulations for the perturbed displacement of an atom in the region of interest. However, a somewhat larger domain than that of interest is necessary and the size of damping kernel matrix is equal to the number of atomic DOFs along the boundary of the domain of interest. E and Huang (2001, 2002) used a discrete summation form of damping forces together with the optimally determined coefficients to minimize the reflection of phonons at the boundary between the atomistic and continuum regions. Li and E (2006)

tried to find the variational boundary conditions which minimize the total phonon reflection by minimizing the energy flux due to the phonon reflections. In the approach of E, Li, and their coworkers, the geometry of lattice must be considered explicitly, which implies that a new formulation for each different lattice structure is required. Karpov et al. (2005) derived the boundary conditions, based on the concept of lattice dynamics using Green's functions together with Laplace and Fourier transformations. Due to the translation symmetry of lattice structures, they obtain a compact time history kernel which is composed of time derivatives of damping kernel matrix. The time history kernel can be predetermined for a given lattice structure and its size could be equal to the number of DOFs in a unit cell. This method is successfully applied to the boundary conditions for a multi-dimensional bridging scale method (Wagner et al. 2004; Park et al. 2005).

1.3.2 DSA of transient dynamics

Mathematically, DSA methods have well developed based on continuum mechanics for structural systems (Choi and Kim 2004a, b). Until now, most of researches on the DSA have been devoted to static problems. Recently, efficient and accurate DSA methods for transient dynamic problems are attracting researchers' attention in various disciplines. Since the MD is one of the transient dynamic problems, DSA for transient dynamic problems is indispensable for the design of nano- and micro- scale problems.

Dynamic problems require the time integration of partial differential equations to compute dynamics responses. For the DSA of dynamic problems, the time-history of design sensitivity of state variables is required to calculate the sensitivity at a given time t . For such path dependent problems, the history of design sensitivity over loading paths is needed up to the load level at which the sensitivity is desired. The response sensitivity at a given time and position depends on both response and response sensitivities of all the previous time steps and locations of the structure. In other words, the exact paths of response and its sensitivity are needed. Thus, the AVM is not appropriate for

path-dependent problems because each adjoint solution yields the sensitivity of only one performance measure, rather than the sensitivities of the full response fields (Cho and Choi 2000a). For transient dynamic problems with large deformation elastic-plastic materials, an analytical DSA method (Cho and Choi 2000b) is developed in the updated Lagrangian formulation using the direct differentiation method (DDM). Hsieh and Arora (1984) developed DSA methods for the dynamic problems of point-wise constraints; the DDM and the AVM were used in their research. Tortorelli et al. (1989) derived the design sensitivity for nonlinear transient thermal systems, based on the adjoint approach using the Lagrange multiplier method and the convolution theory. Tsay and Arora (1990) derived nonlinear DSA for path-dependent problems in the frame of total Lagrangian formulation considering both geometrical and material nonlinearities. Gao et al. (2008) performed shape optimization for time-dependent Navier-Stokes flows. They used the Piola transformation to bypass the divergence-free condition for the shape DSA. In the MD system in this paper, we kept only the time history of kinematics for all the atoms since the tangent stiffness can be easily recovered directly from the original responses.

Extension of DSA methods to the atomic level transient dynamics was never attempted due to the limitation of computational resources and lack of efficient DSA method even though the MD simulations were already established. When the performance measure is only dependent on the terminal time state and the internal force term is linear with respect to the displacement due to the harmonic approximation of the inter-atomic potential, the adjoint equation of motion can be independently solved from the original system. In that case, there is an advantage of saving the computational storage to keep the original response history (Kim et al. 2013a, b). In the case of non-linear internal forces, however, the adjoint equations depend on the path of original responses and thus the tangent stiffness in the adjoint systems changes with each time. In this case, the adjoint problem is time history dependent, which means that we must follow all the history of response analysis for solving that problem.

1.3.3 Reliability analysis

Structural reliability analysis requires more information than in deterministic analysis. Theoretically, if the probability density function (PDF) or the joint PDF of state variables is available, the corresponding failure probability can be evaluated directly through a multidimensional integration. However accurate and efficient numerical integration is often an insurmountable task in practice for given distributions, to say nothing that there are many cases where the complete probabilistic information is unknown for want of sufficient data or knowledge. As a result, normal distribution is often resorted to as a practical alternative. Since the first two moments, namely, the mean value, the variance and the covariance, are sufficient to describe a normal random vector, and can be evaluated easily from the available information, it is often preferable to perform reliability analysis in the normal space. Based on this very concept, the second-moment reliability theory is established.

A variety of second-moment based researches were carried out before the sixties. The cornerstone was laid by Freudenthal (1956) who used complete probability models. However, it is the work of Cornell (1969) that heralded popular acceptance of second moment concept. Later, among many other researchers, Shinozuka (1983) presented a brand new interpretation to the theory. To date, second-moment approaches have become so popular that it always takes an important place in the text books concerning structural safety. Typical of them are those by Alfredo and Wilson (1975), Madsen et al. (1986), Ditlevsen and Madsen (1996), and Robert (1999). With reference to the works mentioned above, second moment theory is discuss in detail. Especially, the first-order reliability method (FORM) for random variables with normal distribution is given due consideration.

1.3.4 Applications of nanomaterials

Nanoparticles have been used in a variety of research fields, including drug delivery, catalysis, biosensing and imaging, due to their numerous potential applications (Sperling et al., 2008). Gold and silver nanoparticles have brought interest in nanomedicine due to their versatile applications including drug delivery, medical diagnostics, biosensors, and cancer therapeutics (Dreaden et al., 2011, Sekhon and Kamboj, 2010). Especially, gold nanoparticles (AuNPs) possess numerous advantages, such as low cytotoxicity, facile modification of their surfaces, straightforward synthetic processes, and excellent biocompatibility. The most common methods for the synthesis of AuNPs use chemical reducing agents to convert Au ions to AuNPs. Current sustainability initiatives require the use of green (eco-friendly or environment-friendly) reducing agents for the synthesis of AuNPs. The green reducing agents include a large number of natural products. Examples of green reducing agents for the synthesis of AuNPs include plant extracts, phytochemicals, polysaccharides and microorganisms (Park et al., 2011b); (Hulkoti and Taranath, 2014). The particle size and morphology play crucial roles in controlling the physical, chemical, optical and electronic properties of these materials (Whitesides and Boncheva, 2002) and for the synthesis of nanoparticle of designed size and shape, surface chemistry, morphology and mechanism research were imperative.

When the metallic nanoparticles were exposed to biological systems, many biological entities interact with the surface of nanoparticles through physical adsorptions. Therefore, the geometrical properties of metallic nanoparticles influence the binding and structure of biological entities which are closely related to their biological activities. The size and morphology of metallic nanoparticles are known to have significant effects on the structure and stability of the adsorbed proteins (Chakraborty et al., 2011, Gagner et al., 2011, Kaur and Forrest, 2012, Park et al., 2011a, Pal et al., 2007). Chakraborty et al. reported that gold nanorods induce protein unfolding at their surface compared with gold nanospheres that used bovine serum albumin as a model compound (Chakraborty et al., 2011). Both nanoparticle

morphology and protein properties determine the final form of nanobioconjugates (Gagner et al., 2011).

There have been many researches made on the temperature and strain-rate effects on nanoscale wires via molecular dynamic simulation. Chang and Fang (2003) investigated tensile and fatigue behavior of nanoscale copper wire at various temperature. The modulus was larger than that obtained by previous studies and decreased with increasing temperature. From the fatigue test, the stress increased with increasing temperature. Also, Jiang et al. (2009) showed that the torsional buckling mode is dependent on both wire length and temperature. Fu et al. (2013) found that the ultimate tensile strength and Young's modulus will decrease as the temperature and size of the CdSe nanowire increase.

Koh et al. (2005) investigated temperature and strain-rate effects on properties of solid platinum nanowire. Sutrakar and Mahapatra (2009) discussed about effects of isothermal and adiabatic thermal loadings on size and strain rate dependence of copper nanowire. Huang et al. (2011) discovered extremely high strain rate effect on the mechanical properties of nickel nanowires with different cross-sectional sizes. Liang and Zhou (2004) analyzed the size and strain effects in the tensile deformation of single-crystal copper nanowires and found that the yield stress decreases with specimen size and increases with loading rate. Lu et al. (2001) observed abnormal strain rate effect on the tensile ductility in an electrodeposited nanocrystalline Cu. Park and Zimmerman (2005) investigated inelasticity and failure of gold nanowires according to strain rate. Wang et al. (2013) showed tensile properties dependence of ultrathin nickel nanowires at different temperature and strain rates. Wen et al. (2008) analyzed strain rate effects on mechanical responses and deformation behavior of nickel nanowires.

Using MD simulation, unusual mechanical properties of metallic nanowire such as pseudoelasticity, shape memory, and cold welding are also reported. Liang and Zhou (2005) discovered rubber-like pseudoelastic behavior in face-centered-cubic (FCC) Cu nanowires in atomistic simulations.

Under tensile loading and unloading, the nanowires exhibit recoverable strains up to over 50% which is well beyond the typical recoverable strains of 5-8% for most bulk shape memory alloys. Park and Ji (2006) presented uniaxial thermomechanical deformation of single-crystal silver shape memory nanowires. The simulations show that the resulting mechanical response of the shape memory nanowires depends strongly upon the temperature during deformation and can be fundamentally different from that observed in bulk polycrystalline shape memory alloys. Pereira and da Silva (2011) investigated the cold welding of gold and silver nanowires at room temperature via molecular dynamics study. They have shown that the cold welding is possible process even after losing their crystalline structure after breaking.

Since Iijima (1991) first discovered CNTs in 1991, it has become an important material in thermal sciences. Since that time, a significant amount of effort has been put into the theoretical and experimental study of these structures. There is immense interest in nanoscale graphitic structures and CNTs not only for their mechanical and electrical properties, but also for their thermal properties, which are fundamentally important in controlling system performance. Thermal conductivity of a SWNT has been reported to be as high as 6000 W/m K at room temperature by Berber et al. (2000) and is higher than both diamond and graphite under the same conditions.

One of the remarkable properties of the CNTs is its thermal conductivity. Thermal conductivity of single-walled and multi-walled CNTs is reported to be about $3,000 \text{ W/mK}$ or higher at room temperature by experimental approaches. Kim et al. (2001) observed that the thermal conductivity of an isolated multi-walled CNT with a diameter of 14 nm is more than $3,000 \text{ W/mK}$ at room temperature. Fujii et al. (2005) presented experimental data of thermal conductivity of single-walled CNT having various diameter. Their results also show that the thermal conductivity of CNT with a diameter of 9.8 nm exceed $2,000 \text{ W/mK}$. Yu et al. (2005) measured the thermal conductivity of a $2.76 \text{ }\mu\text{m}$ -long isolated single-walled CNT and the results are about $3,000 \text{ W/mK}$ which have the same order of magnitude as the measurement results of an isolated multi-walled CNT. The thermal conductivity reported by Pop et al.

(2005) of a single-walled CNT of length $2.6 \mu m$ and diameter $1.7 nm$ is nearly $3,500 W/mK$ at room temperature. Hone et al. (1999) observed that the thermal conductivity of aligned single-walled CNTs crystalline ropes is about $250 W/mK$ at 300 K. In their following works, the thermal conductivity of magnetically aligned single-walled CNT films is measured about $200 W/mK$ in the parallel direction, within a decade of graphite (Hone et al., 2000). A recent measurement on an isolated single-walled CNT by Yu et al. (2003) reveals a higher thermal conductivity than that of multi-walled CNT. Evidently, experimental studies can provide a wealth of meaningful thermal conductivity of CNTs.

1.3.5 Organizations of thesis

In Chapter 2, the MD simulation is reviewed. Starting from Lagrangian and Hamiltonian, Newtonian and Hamiltonian equations of motion are derived for given conserved particle systems. The Nose-Hoover thermostat for constant temperature MD simulations is derived to consider NVT ensemble. Inter-atomic potentials used in this research are also introduced. In Chapter3, basic concepts of the reliability analysis is review. In Chapter 4, we discuss the DSA method of MD simulations considering the uncertainty from ensemble and potential parameters. The effect of uncertainties is evaluated based on the analytical first and second order sensitivities with respect to the random and design variables. In Chapter 5, some numerical examples are demonstrated to show the accuracy and efficiency of the developed DSA method considering the uncertainty for various nanoscale problems. Developed DSA method is further extended to design optimization problem to find unknown potential parameters for the interactions between the nanoparticle and substrate.

Chapter 2. Molecular Dynamics Simulations

In this chapter we review the molecular dynamics (MD) simulation which is a typical transient dynamic problem. In mechanical problems considering continuum-scale materials, the finite element method (FEM) is widely used, which is based on variation formulations assuming that the solution fields are included in continuous functional spaces to meet boundary conditions. However, when we consider the nano-scale phenomena in the nanomaterials, the FEM is not sufficient since the assumption of continuum is not acceptable in the discrete atomic level so that another tool should be employed for the analysis of atomic phenomena.

For investigating mechanical behaviors and extracting material properties of nanomaterials, the MD is one of the most popular tools to simulate nano-scale phenomena in discrete atomic-level. Since atomic structures are governed by the interactions among atoms, inter-atomic potentials need to be defined. The choice of the inter-atomic potential depends on the given MD system. Some potentials which are appropriate to the problem what we concentrated are briefly introduced.

The computational cost for the potentials is very expensive since all of the interactions between atoms should be considered. This problem gets more serious when millions of atoms are considered in simulations so that various computational techniques are developed for reducing the cost of inter-atomic potentials and forces evaluation which is dominant in overall cost of MD simulations. To overcome this difficulty in MD simulations, the periodic boundary conditions is introduced.

This chapter is organized as follows. In Section 2.1, the equations of motion for the molecular dynamics simulation are derived using the classical Lagrangian and Hamiltonian formulations. The equations of motion for constant temperature molecular dynamics are also derived using Nose-Hoover thermostat (Nose 1984a, b; Hoover 1985) to simulate more practical

engineering problems. In Section 2.2, the inter-atomic potentials are introduced. To speed up the simulation, cut-off radius of potential is also introduced. In Section 2.3, the periodic boundary conditions are briefly reviewed.

2.1 Equation of motion

2.1.1 Lagrangian and Hamiltonian equations of motion

The Lagrangian is defined by the difference of kinetic and potential energy in Cartesian coordinates as

$$L = \frac{1}{2} \sum_{i=1}^{n_a} m_i \dot{\mathbf{r}}_i \cdot \dot{\mathbf{r}}_i - U(\mathbf{r}_1, \mathbf{r}_2, \dots, \mathbf{r}_N), \quad (2.1.1)$$

where $\mathbf{r}_i = (x_i, y_i, z_i)$ is the position vector of atom i in 3-dimensional space; superposed dot denotes time derivatives; m_i is the mass of atom i ; and n_a is the total number of atoms. To get the equations of motion for the given systems, we use the following Euler-Lagrange equations as

$$\frac{d}{dt} \frac{\partial L}{\partial \dot{\mathbf{r}}_i} - \frac{\partial L}{\partial \mathbf{r}_i} = 0, \quad i = 1, 2, \dots, n_a. \quad (2.1.2)$$

By substituting Equation (2.1.1) into Equation (2.1.2), the equations of motion can be written in the Newtonian form as

$$m_i \ddot{\mathbf{r}}_i = - \frac{\partial U(\mathbf{r}_1, \mathbf{r}_2, \dots, \mathbf{r}_N)}{\partial \mathbf{r}_i} \equiv \mathbf{f}_i, \quad i = 1, 2, \dots, n_a. \quad (2.1.3)$$

The force vector \mathbf{f}_i is the internal force exerted on atom i .

For a general expression of Equation (2.1.3) in arbitrary coordinates, we can

define s independent variables q_α ($\alpha=1,2,\dots,s$) as generalized coordinates that define the spatial positions of atoms, uniquely. The relationship between the position vectors of Cartesian coordinates and generalized coordinates can be expressed by the following transformation equations,

$$\mathbf{r}_i = \mathbf{r}_i(q_1, q_2, \dots, q_s), \quad i = 1, 2, \dots, n_a, \quad (2.1.4)$$

which are the representation of the position vector \mathbf{r}_i in terms of the generalized co-ordinates q_α . The total degrees of freedom are $s = 3n_a$ in 3-dimensional space. Using Equation (2.1.4), the velocities can be expressed as

$$\dot{\mathbf{r}}_i = \sum_{\alpha=1}^s \frac{\partial \dot{\mathbf{r}}_i}{\partial q_\alpha} \dot{q}_\alpha, \quad i = 1, 2, \dots, n_a, \quad (2.1.5)$$

and Lagrangian of (2.1.1) can be re-written in generalized coordinates as

$$L = \frac{1}{2} \sum_{\alpha=1}^s \sum_{\beta=1}^s a_{\alpha\beta}(q_1, q_2, \dots, q_s) \dot{q}_\alpha \dot{q}_\beta - U(q_1, q_2, \dots, q_s), \quad (2.1.6)$$

where the transformed mass matrix is written as

$$a_{\alpha\beta}(q_1, q_2, \dots, q_s) = \sum_{i=1}^{n_a} m_i \frac{\partial \dot{\mathbf{r}}_i}{\partial q_\alpha} \cdot \frac{\partial \dot{\mathbf{r}}_i}{\partial q_\beta}. \quad (2.1.7)$$

Then, the corresponding Euler-Lagrange equations in generalized coordinates are expressed as

$$\frac{d}{dt} \frac{\partial L}{\partial \dot{q}_\alpha} - \frac{\partial L}{\partial q_\alpha} = 0, \quad \alpha = 1, 2, \dots, s. \quad (2.1.8)$$

Description of mechanical systems in terms of generalized coordinates and velocities is not unique. Alternative formulation in terms of generalized coordinates and momenta can be utilized. This formulation is used in

statistical mechanics to get the macroscopic properties from the microscopic results. Legendre's Transformation is the passage from one set of independent variables to another like $(q_\alpha, \dot{q}_\alpha)$ to (q_α, p_α) where p_α is the generalized momenta of α degree of freedom defined as

$$p_\alpha = \frac{\partial L}{\partial \dot{q}_\alpha}, \quad \alpha = 1, 2, \dots, s, \quad (2.1.9)$$

The classical Hamiltonian of system can be derived from the following Legendre transformation of Lagrangian given in Equation (2.1.6) as

$$H = \sum_{\alpha=1}^s \dot{q}_\alpha p_\alpha - L. \quad (2.1.10)$$

This transformation changes the variables \dot{q}_α to p_α , mathematically. The complete differential of Hamiltonian is written as

$$\begin{aligned} dH &= \sum_{\alpha=1}^s \dot{q}_\alpha dp_\alpha + \sum_{\alpha=1}^s p_\alpha d\dot{q}_\alpha - dL \\ &= \sum_{\alpha=1}^s \dot{q}_\alpha dp_\alpha - \sum_{\alpha=1}^s \dot{p}_\alpha dq_\alpha \\ &= \sum_{\alpha=1}^s \frac{\partial H}{\partial p_\alpha} dp_\alpha + \sum_{\alpha=1}^s \frac{\partial H}{\partial q_\alpha} dq_\alpha, \end{aligned} \quad (2.1.11)$$

Then, Hamiltonian equations of motion are obtained by

$$\dot{q}_\alpha = \frac{\partial H}{\partial p_\alpha} \quad \text{and} \quad \dot{p}_\alpha = -\frac{\partial H}{\partial q_\alpha}. \quad (2.1.12)$$

Equations (2.1.12) are the first order ordinary differential equations with respect to time. The number of equations and unknowns are instead double, compared with Newtonian equations given in Equation (2.1.3).

Since there are no explicit time terms in Hamiltonian, the total time derivative of Hamiltonian gives the following.

$$\frac{dH}{dt} = \frac{\partial H}{\partial t} + \sum_{\alpha=1}^s \frac{\partial H}{\partial p_{\alpha}} d\tilde{p}_{\alpha} + \sum_{\alpha=1}^s \frac{\partial H}{\partial q_{\alpha}} d\tilde{q}_{\alpha} = \frac{\partial H}{\partial t} = 0. \quad (2.1.13)$$

Equation (2.1.13) implies that the value of Hamiltonian function is an integral of motion for conservative systems since Hamiltonian is defined to be the total energy of system in terms of the generalized co-ordinates and momenta. The MD systems which are governed by classical Newtonian equations conserve the total energy E , the number of particles N and the volume V , so that they are so-called NVE ensembles.

2.1.2 NVT ensemble

To perform a molecular dynamics simulation on a system where the number of particles N , the volume V , and the temperature T are fixed, the physical system is considered that contacts with a heat bath. Hamiltonian for the extended system in terms of the extended variables can be written as

$$H(\tilde{p}, q, \tilde{p}_s, s) = \sum_{i=1}^{3N} \frac{\tilde{p}_i^2}{2m_i s^2} + \frac{\tilde{p}_s^2}{2Q} + V_{pot}(q) + z \ln s, \quad (2.1.14)$$

where q , \tilde{p} and V_{pot} are atomic position, the momenta conjugate to q , and potential energy function respectively. s , \tilde{p}_s and Q denote the additional degree of freedom for heat bath, the momentum conjugate to s , and an effective mass associated to s . z is a factor for sampling a canonical distribution. The upper tilde denotes the extended variables corresponding to the scaled time τ .

The equation of motion of the extended system variables are found to be

$$\frac{d\tilde{p}_i}{d\tau} = F_i, \quad (2.1.15)$$

$$\frac{dq_i}{d\tau} = \frac{\tilde{p}_i}{m_i s^2}, \quad (2.1.16)$$

$$\frac{d\tilde{p}_s}{d\tau} = \sum_{i=1}^{3N} \frac{\tilde{p}_i^2}{m_i s^3} - z \frac{1}{s}, \quad (2.1.17)$$

$$\frac{ds}{d\tau} = \frac{\tilde{p}_s}{Q}. \quad (2.1.18)$$

It can be considered that the real (physical) time t is scaled to the scale time τ in the extended system according to

$$d\tau = s dt. \quad (2.1.19)$$

If we sample the canonical distribution or calculate the ensemble average with the extended variable τ , the sampling is done at integer multiples of the extended time step $\Delta\tau$ that are not constant. Therefore, for the sampling at equal intervals in physical time, it will be convenient to do the integrations in terms of the physical system variables by means of the transformations $p_i = \tilde{p}_i / s$ and Equation (2.1.19). Using the transformations, we can come up with the equation of motion for physical system variables and heat bath variables

$$\dot{p}_i = F_i - p_i \frac{\dot{s}}{s}, \quad (2.1.20)$$

$$\dot{q}_i = \frac{p_i}{m_i}, \quad (2.1.21)$$

$$\dot{p}_s = \sum_{i=1}^{3N} \frac{p_i^2}{m_i} - z, \quad (2.1.22)$$

$$\dot{s} = s \frac{p_s}{Q}. \quad (2.1.23)$$

We can obtain the second order Lagrangian equation of motion in terms of physical variables which most often are used in molecular dynamics simulations by combining the first order equations of motion. By introducing the friction coefficient $\zeta = \dot{s}/s$ proposed by Hoover (1985), the equation of motion according to

$$\ddot{q}_i = \frac{F_i}{m_i} - \dot{q}_i \zeta, \quad (2.1.24)$$

$$\dot{\zeta} = \frac{1}{Q} \left(\sum_{i=1}^{3N} m_i \dot{q}_i^2 - z \right). \quad (2.1.25)$$

The factor z is determined in order to recover a canonical sampling

$$z = 3Nk_B T. \quad (2.1.26)$$

Notice that the number of atoms N is used in Equation (2.1.26) since Equations (2.1.24) and (2.1.25) are written in physical variable formulation.

2.2 Interatomic potentials

The interactions between atoms can be defined through inter-atomic potential $U(\mathbf{r}_1, \mathbf{r}_2, \dots, \mathbf{r}_N)$ defined in Equation (2.1.1). To describe accurate atomic interactions within the simulated system, we consider subatomic level nature such as the complicated quantum effects that are responsible for the bonding and breaking of atoms and spatial arrangement of atomic valence. In order to obtain reliable results from the MD simulations, the classical inter-atomic potential should include these quantum mechanical processes. Even though it is difficult and complicated, we can express the general structure of potential energy as

$$U(\mathbf{r}_1, \mathbf{r}_2, \dots, \mathbf{r}_N) = \sum_i \Phi^1(\mathbf{r}_i) + \sum_{i,j>i} \Phi^2(\mathbf{r}_i, \mathbf{r}_j) + \sum_{i,j>i,k>j} \Phi^3(\mathbf{r}_i, \mathbf{r}_j, \mathbf{r}_k) + \dots, \quad (2.2.1)$$

where Φ^m is the m -body potential. The first term is the potential energy due to the gravity and the electrostatic force. The second term is due to the pair-wise interactions of particles and the third is due to the three-body inter-atomic potential energy. Generally, the pair-wise interaction is employed, truncating the sum of Equation (2.2.1) after the second term. The potential is instead designed to include the multi-body effects in the pair-wise potential Φ^2 .

2.2.1 Lennard-Jones (LJ) potentials

The most well-known pair-wise potential is the Lennard-Jones (LJ) potential given as

$$\Phi^2(\mathbf{r}_i, \mathbf{r}_j) = \Phi(r) = 4\varepsilon \left\{ \left(\frac{\sigma}{r} \right)^{12} - \left(\frac{\sigma}{r} \right)^6 \right\}, \quad r = |\mathbf{r}_i - \mathbf{r}_j|. \quad (2.2.2)$$

ε is the energy depth which shows the bonding/dislocation of particles; the work required to be done in order to remove one of two coupled atoms from its equilibrium position. This means that the value of ε is the minimum value of Equation (2.2.2). σ is the collision diameter; the distance at which $\Phi_{LJ}(r) = 0$ and related with the equilibrium bond length. The equilibrium length is found such that the following inter-atomic force is equal to zero.

$$F(r) = -\frac{\partial\Phi(r)}{r} = 24\frac{\varepsilon}{\sigma} \left\{ \left(\frac{\sigma}{r} \right)^{13} - \left(\frac{\sigma}{r} \right)^7 \right\}. \quad (2.2.3)$$

The equilibrium length is $\rho = 2\sqrt[6]{\sigma}$. The dimensionless potential and force functions in Equations (2.2.2) and (2.2.3) are shown according to the inter-atomic distance in Figure 2.1. Typically, the unit of ε is Joule (J) or electron volt (eV) and the magnitude is around 10^{-19} to 10^{-18} J. σ has the length scale unit and has several Angstroms (Å).

Physically, the first term of this potential represents the atomic repulsion while the second term shows the attraction between atoms. The repulsion force rapidly increases as the distance decreases while the attraction force slowly increases as the distance increases from the equilibrium distance, since the order of repulsion terms is higher than that of attraction. As the distance increases from the equilibrium distance, the inter-atomic potential and force almost approaches zero, which implies that breaking of interaction occurs between the two atoms.

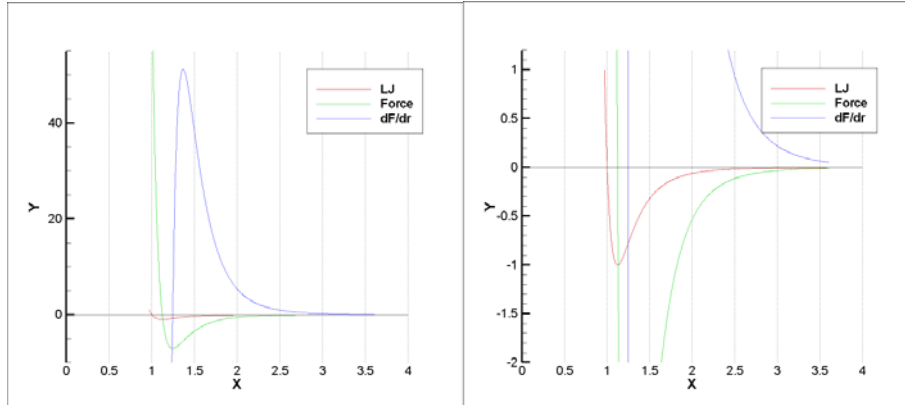


Figure 2.1 L-J potential (red), L-J force (green), and the derivative of force (blue)

2.2.2 Embedded Atom Method (EAM) for metallic systems

Many body effects are important in real materials. It became clear that there are certain things we could not get right with pair potentials because of problems of the ‘wrong form’ rather than problems of ‘wrong parameters’. Pair potentials do not have environmental dependence. Pair potentials also have quantitative problems; the vacancy formation energy and the ratio between cohesive energy and the melting temperature are overestimated or underestimated since metals have some “extra cohesion”. The EAM potential is known to be suitable for the metallic MD system since the local electron densities are considered to describe the bonding in metallic systems.

In the EAM potential, the potential energy of an atom i is given by

$$E_i = F_i(\bar{\rho}_i) + \frac{1}{2} \sum_{j \neq i} \phi_{ij}(r_{ij}), \quad E_{total} = \sum_i E_i, \quad (2.2.4)$$

where F_i is the embedding energy which is a function of the atomic electron density $\bar{\rho}_i$ which is given by

$$\bar{\rho}_i = \sum_{j \neq i} \rho_j(r_{ij}). \quad (2.2.5)$$

ϕ is a pair potential interaction which has the form of

$$\phi_{ij}(r_{ij}) = z_i(r_{ij}) z_j(r_{ij}) / r_{ij}, \quad (2.2.6)$$

where z_i is effective charge function of an atom i .

EAM force acting on the atom i is derived from Equation (2.2.4).

$$\vec{f}_i = -\frac{\partial E_{total}}{\partial \vec{u}_i} \frac{\partial r}{\partial \vec{u}_i} = -\sum_{j \neq i} \left[\frac{\partial F_i}{\partial \rho_i} \frac{\partial f_j}{\partial r} + \frac{\partial F_j}{\partial \rho_j} \frac{\partial f_i}{\partial r} + \frac{\partial \phi_{ij}}{\partial r} \right]_{r=r_{ij}} \frac{(\vec{u}_i - \vec{u}_j)}{r_{ij}}. \quad (2.2.7)$$

In the public MD simulation packages such as LAMMPS (Large-scale Atomic/Molecular Massively Parallel Simulator), the functions $F(\rho)$, $\rho(r)$, $z(r)$ which do not have analytical forms are given as a table of data points that result from fitting to experimental data. Given the data points $\{f_i\}$, the cubic Hermite interpolant is defined for $1 \leq i < n$ as

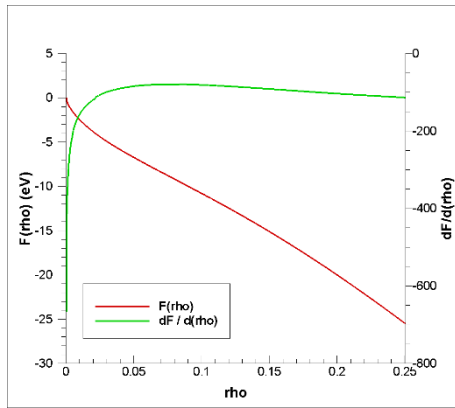
$$P(x) = c_1 + (x - x_i) c_2 + (x - x_i)^2 c_3 + (x - x_i)^3 c_4, \quad (2.2.8)$$

where $x_i \leq x \leq x_{i+1}$,

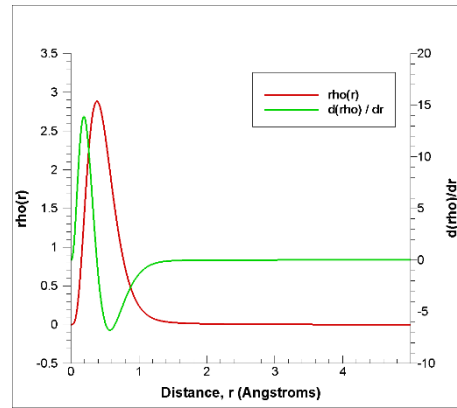
$$c_1 = f_i, \quad c_2 = \dot{f}_i, \quad c_3 = \frac{3S_{i+1/2} - \dot{f}_{i+1} - 2\dot{f}_i}{\Delta x_{i+1/2}}, \quad c_4 = -\frac{2S_{i+1/2} - \dot{f}_{i+1} - \dot{f}_i}{\Delta x_{i+1/2}^2}. \quad (2.2.9)$$

The local mesh spacing is $\Delta x_{i+1/2} = x_{i+1} - x_i$, and the slope of the piecewise linear interpolant between the data points is $S_{i+1/2} = \Delta f_{i+1/2} / \Delta x_{i+1/2}$. The

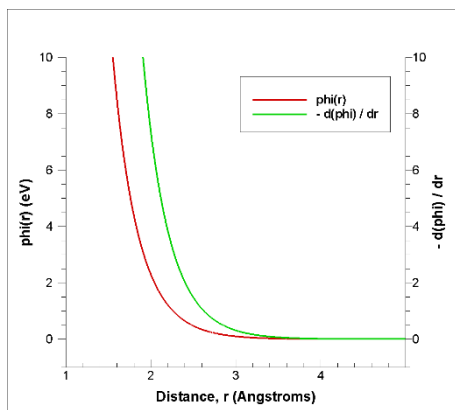
slope $\{\dot{f}_i\}$ is numerical approximated at x_i utilizing the fourth-order finite difference. This is a local approximation, so that the interpolant (2.2.8) has a continuous first derivative, $p(x) \in C^1$, but the second derivative is not continuous. The non-local approximation for $\{\dot{f}_i\}$ is inevitable for $p(x) \in C^2$, which is necessary for calculation of the sensitivity of the interatomic force. Figure 2.2 shows the interpolated embedding energy, electron density, and pair potential energy of copper with corresponding 1st derivatives.



(a) $F(\rho)$, $dF/d\rho$



(b) $\rho(r)$, $d\rho/dr$



(c) $\phi(r)$, $-\phi(r)/dr$

Figure 2.2 Graphs of the embedding energy $F(\rho)$, electron density $\rho(r)$, and pair potential $\phi(r)$ functions of copper which are obtained from the spline fitting. The green solid lines denote the corresponding derivatives.

2.2.3 Tersoff bond-order potential for covalent bond

Tersoff (1988) first developed the basis for the potential which is appropriate to the covalently bonded system for his simulation of covalent silicon. The Tersoff bond-order potential is widely used to describe Carbon-Carbon bond in Carbon nanotubes.

The Tersoff bond-order potential is given in the form of

$$E = \frac{1}{2} \sum_i \sum_{j \neq i} V_{ij}, \quad (2.2.10)$$

where the potential energy for i-j pair is given as

$$V_{ij} = f_C(r_{ij}) \left[f_R(r_{ij}) + b_{ij} f_A(r_{ij}) \right]. \quad (2.2.11)$$

$f_C(r)$ is a cut-off function which has the form of

$$f_C(r) = \begin{cases} 1, & r \leq R - D \\ \frac{1}{2} - \frac{1}{2} \sin \left[\frac{\pi(r - R)}{2D} \right], & R - D \leq r \leq R + D \\ 0 & r \geq R + D \end{cases}. \quad (2.2.12)$$

The repulsive and attractive terms are defined as

$$f_R(r) = A \exp(-\lambda_1 r), \quad (2.2.13)$$

$$f_A(r) = -B \exp(-\lambda_2 r). \quad (2.2.14)$$

The repulsive term can be treated as a pair-wise term. However, the attractive term includes a three-body interaction.

$$b_{ij} = \left(1 + \beta^n \zeta_{ij}^n \right)^{-\frac{1}{2n}}, \quad (2.2.15)$$

$$\zeta_{ij} = \sum_{k \neq i, j} f_c(r_{ik}) g(\theta_{ijk}) \exp\left[\lambda_3^m (r_{ij} - r_{ik})^m\right], \quad (2.2.16)$$

$$g(\theta) = \gamma_{ijk} \left(1 + \frac{c^2}{d^2} - \frac{c^2}{\left[d^2 + (\cos \theta - h)^2 \right]} \right). \quad (2.2.17)$$

For the given atom pair $i - j$, we need to calculate the interatomic forces which is acting on the atoms i, j and k ($k \neq i, j$) due to the bond angle term $g(\theta_{ijk})$.

2.2.4 Cut-off radius of potentials

One critical issue in the molecular dynamics is the computational cost for inter-atomic force given in Equation (2.1.3). Even if the pair-wise interactions are used, $N(N-1)/2$ times calculations of potential energy are required, where N is the total number of atoms. Since the interaction forces are almost equal to zero from a certain distance as shown in Figure 2.1, interactions of atoms away from that distance can be ignored. The distance is called the cut-off radius and the potential energy can be expressed as

$$\Phi^{cut-off}(r) = \begin{cases} \Phi(r), & r \leq R_{cut} \\ 0 & , r > R_{cut} \end{cases} \quad (2.2.18)$$

for a given cut-off radius R_{cut} .

2.3 Periodic boundary conditions

Periodic boundary conditions enable a simulation to be performed using a relatively small number of particles, in such a way that the particles experience forces as if they were in bulk. Figure 2.3 shows the interaction between the i -th atom in simulation box with j -th atom in the image when performing the periodic boundary condition. Half the dimension of the simulation box must be larger than the cutoff radius.

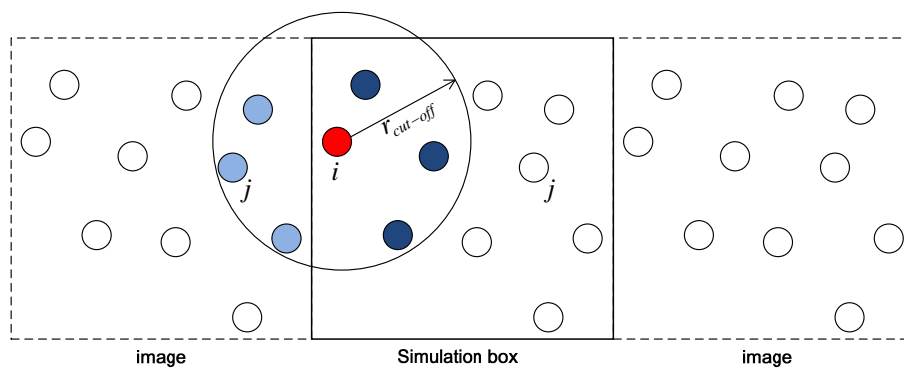


Figure 2.3 Illustration of periodic boundary conditions

Chapter 3. Reliability Analysis

In this chapter, an introduction to conventional reliability analysis methods and an overview on basic statistics are presented. The field of reliability analysis is in its nature probabilistic, and thus, some statistical knowledge are important. After a brief survey of the theory behind, some common solution strategies to problems involving failure probability are reviewed. Most notably, the concept of first-order reliability method (FORM) is introduced and is extended to molecular dynamics simulation problems to handle the uncertainties laying under the simulation by utilizing the sensitivity of performance measure with respect to random variables.

3.1 Descriptions of Random Variables

A random variable is a variable whose value is uncertain or nondeterministic, such as the material property, loading condition and any other material or physical quantity. There are two types of random variables, a discrete random variable is defined as an integer value, which its probability is given by the probability mass function (PMF). The other type of a random variable is the continuous random variable defined as a value of an interval of real numbers, which its probability is given by the probability density function (PDF). If the form of the distribution function and its associated parameters were specified, the statistic parameters of a random variable would be described completely. The probabilistic characteristics of a random variable may be determined in terms of the mean value, variance and standard deviation.

3.1.1 Mean Value

The mean value can be defined as the first moment about the origin. For a continuous random variable, the mean is defined as

$$\mu = \int_{-\infty}^{+\infty} x f_x(x) dx, \quad (3.1.1)$$

where $f_x(x)$ is PDF of continuous random variable x .

For a discrete random variable, the mean is given by

$$\mu = \sum_{i=1}^n x_i P_x(x_i), \quad (3.1.2)$$

where $P_x(x_i)$ is PMF of discrete random variable x .

If all n observations are given equal weights, then the sample mean would be the average of the observed values for a discrete random variables as

$$\mu = \frac{1}{n} \sum_{i=1}^n x_i. \quad (3.1.3)$$

3.1.2 Variance and Standard Deviation

The variance is the second moment about the mean, denoted by σ^2 . The standard deviation is the square root of the variance, denoted as σ . For an continuous random variable, the variance is defined as

$$\sigma^2 = \int_{-\infty}^{+\infty} (x - \mu)^2 f_x(x) dx. \quad (3.1.4)$$

For a discrete random variable, the variance is given by

$$\sigma^2 = \sum_{i=1}^n (x_i - \mu)^2 P_x(x_i). \quad (3.1.5)$$

3.2 Probability Distributions

There are two types of probability distributions, classified as discrete and continuous distributions. In this thesis, only the most common types of continuous distributions, as normal and lognormal, are presented. Further details about other distribution types are found in, Leitch (1995).

3.2.1 Normal Distribution

The normal distribution is the most widely used probability distribution, also known as Gaussian distribution. The probability density function (PDF) for a normal distribution is given as

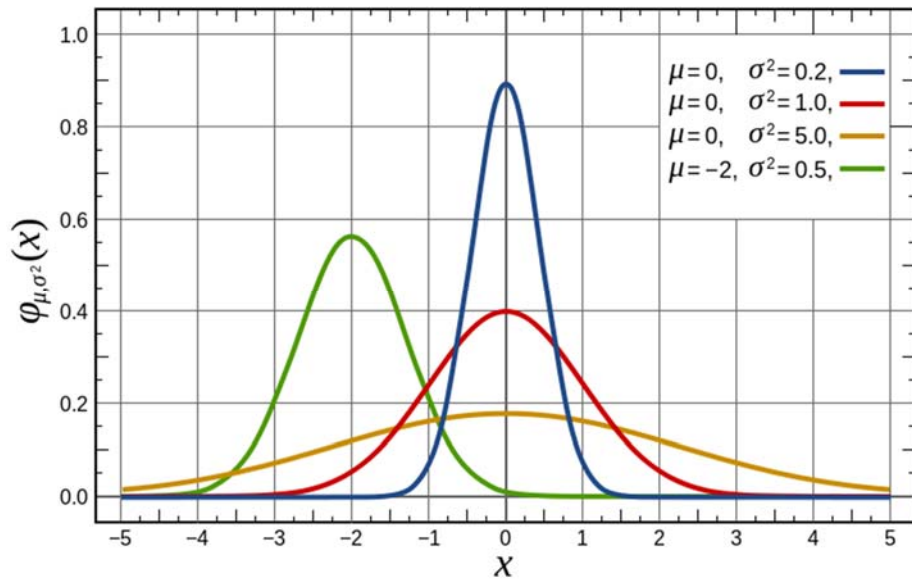
$$f_x(x) = \frac{1}{\sigma\sqrt{2\pi}} \exp\left[-\frac{1}{2}\left(\frac{x-\mu}{\sigma}\right)^2\right], \quad (3.2.1)$$

where μ is the mean value and σ is the standard deviation which are the parameters of the distribution.

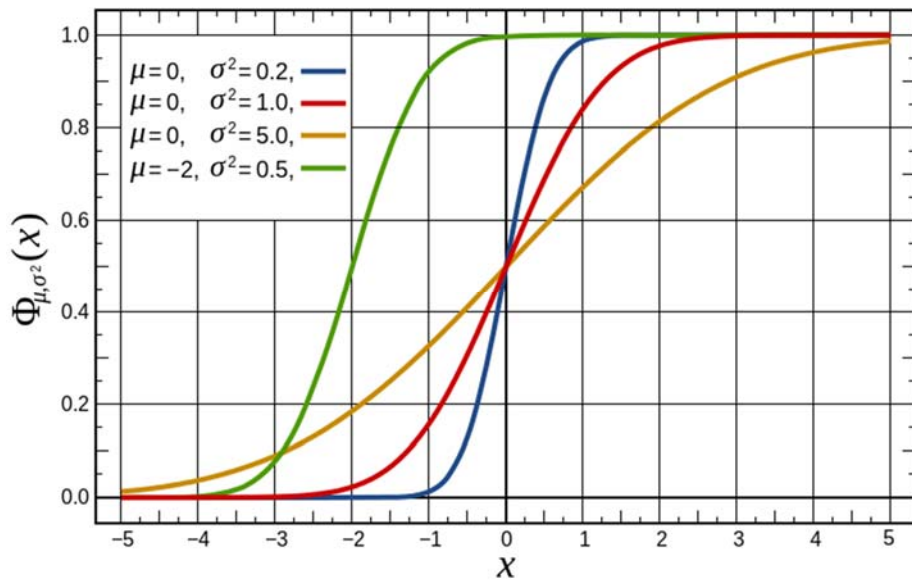
The cumulative distribution function (CDF) of the normal distribution is defined as

$$F_x(x) = \int_{-\infty}^x \frac{1}{\sigma\sqrt{2\pi}} \exp\left[-\frac{1}{2}\left(\frac{x-\mu}{\sigma}\right)^2\right] dx. \quad (3.2.2)$$

The PDF and CDF of a normal distribution for a random variables are presented in Figure 3.1



(a) PDF of normal distribution



(b) CDF of normal distribution

Figure 3.1 PDF and CDF of normal distribution

3.2.2 Lognormal Distribution

The lognormal distribution is used for general reliability analysis, such as the random variable x is lognormal distributed if the logarithm of the random variable is normally distributed as $y = \ln(x)$.

The probability density function (PDF) of the lognormal distribution is defined as

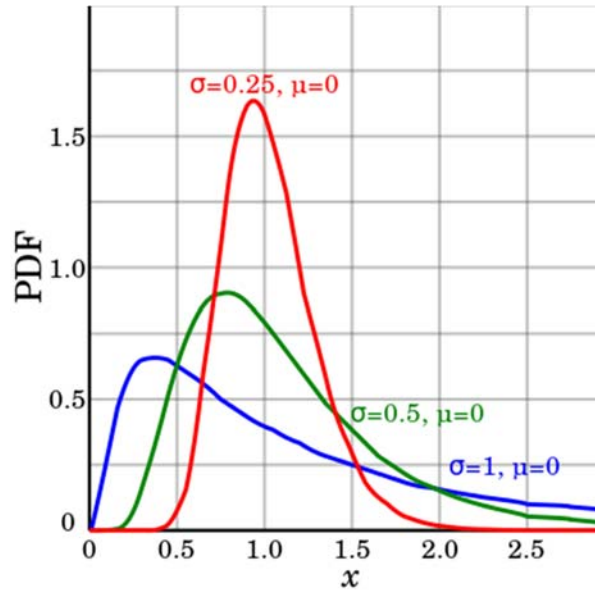
$$\begin{aligned} f_x(x) &= \frac{1}{x\sigma_{\ln(x)}} \phi\left(\frac{\ln(x) - \mu_{\ln(x)}}{\sigma_{\ln(x)}}\right) \\ &= \frac{1}{x\sigma_y} \exp\left[-\frac{1}{2}\left(\frac{\ln(x) - \mu_y}{\sigma_y}\right)^2\right], \end{aligned} \quad (3.2.3)$$

where μ_y and σ_y are the mean and the standard deviation of lognormal distribution.

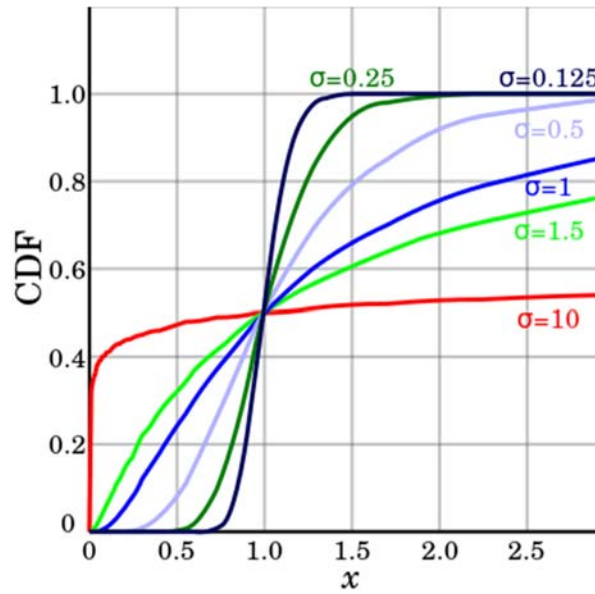
The cumulative distribution function (CDF) of the lognormal distribution can be determined as

$$F_x(x) = F_y(x) = \Phi\left(\frac{y - \mu_y}{\sigma_y}\right). \quad (3.2.4)$$

The PDF and CDF of the lognormal distribution are shown in Figure 3.2.



(a) PDF of lognormal distribution



(b) CDF of lognormal distribution

Figure 3.2 PDF and CDF of lognormal distribution

3.3 Limit State Function

A limit state function is a boundary between desired and undesired performance measure. The limit state function can be defined as the performance function when all loads are assigned to the variable Q , and the capacity is assigned to the resistance, R . the formulation of the limit state function is expressed as

$$g(R, Q) = R - Q. \quad (3.3.1)$$

3.4 Reliability Index

The reliability index, β , can be defined as the safety index. Then, the reliability index can be calculated from Cornell (1969) as

$$\beta = \frac{\mu_R - \mu_Q}{\sqrt{\sigma_R^2 + \sigma_q^2}}. \quad (3.4.1)$$

3.5 Second-Moment Theory of Reliability Analysis

Structural reliability analysis requires more information than in deterministic analysis. Theoretically, if the PDF or the joint PDF of state variables is available, the corresponding failure probability can be evaluated directly through a multidimensional integration. However accurate and efficient numerical integration is often an insurmountable task in practice for given distributions, to say nothing that there are many cases where the complete probabilistic information is unknown for want of sufficient data or knowledge. As a result, normal distribution is often resorted to as a practical

alternative. Since the first two moments, namely, the mean value, the variance and the covariance, are sufficient to describe a normal random vector, and can be evaluated easily from the available information, it is often preferable to perform reliability analysis in the normal space. Based on this very concept, the second-moment reliability theory is established.

A variety of second-moment based researches were carried out before the sixties. The cornerstone was laid by Freudenthal (1956) who used complete probability models. However, it is the work of Cornell (1969) that heralded popular acceptance of second moment concept. Later, among many other researchers, Shinozuka (1983) presented a brand new interpretation to the theory. To date, second-moment approaches have become so popular that it always takes an important place in the text books concerning structural safety. Typical of them are those by Alfredo and Wilson (1975), Madsen et al. (1986), Ditlevsen and Madsen (1996), and Robert (1999). With reference to the works mentioned above, second moment theory is discuss in detail. Especially, the first-order second moment (FOSM) method for random variables with normal distribution is given due consideration.

3.5.1 Geometric measure of reliability

It is now a common sense that geometry and algebra are closely related to each other. In fact, this kinship is the foundation on which the building of modern applied mathematics is constructed. In some sense, almost all the problems in practice may finally be converted equivalently to a problem of minimum distance in certain space, for example, the well known light traveling problem in Euclidian space, the least square problem in Hilbert space, and the variational problem in Soblevian space. Little wonder this also holds true of reliability analysis.

To illustrate this point, let us consider a system with limit state function

$$G(\mathbf{X}) = G(X_1, X_2, \dots, X_n), \quad (3.5.1)$$

where \mathbf{X} is the vector of state variables, which are assumed to be uncorrelated normal distributed ones. Geometrically, the limit state equation $G(\mathbf{X})=0$ is an n-dimensional surface in random space. It is termed failure surface, with one side $G(\mathbf{X})>0$ defining the safe state and the other side $G(\mathbf{X})<0$ the failure state. It follows that the failure probability is

$$P_f = P[G(\mathbf{X}) \leq 0], \quad (3.5.2)$$

if $M = G(\mathbf{X})$, the safety margin, happen to be a normal variable then

$$P_f = P[M \leq 0] = F_M(0) = \Phi\left(-\frac{\mu_M}{\sigma_M}\right), \quad (3.5.3)$$

where F_M is the cumulative density function (CDF) of M , Φ is the CDF of standard normal variable, and μ_M and σ_M are the mean value and the standard deviation of M . Defining

$$\beta = \frac{\mu_z}{\sigma_z} = \frac{E[G(\mathbf{X})]}{D[G(\mathbf{X})]}, \quad (3.5.4)$$

we obtain

$$P_f = \Phi(-\beta), \quad (3.5.5)$$

Where β is termed reliability index or safety index. The Equation (3.5.4) is the distance of location $E[G(\mathbf{X})]$ to the failure surface $M=0$ in the unit of $D[G(\mathbf{X})]$.

As is always the case, $G(\mathbf{X})$ may not be a linear function of \mathbf{X} ; that is, M is not necessarily normal. For convenience, a hyper-plane $R(\mathbf{X})=0$ tangent to the failure surface may be adopted as an approximate limit state by expanding $G(\mathbf{X})$ in Taylor series at a point \mathbf{X}_0 on the actual failure

surface and retaining the first order items only. Considering that $G(\mathbf{X}_0) = 0$, this yields

$$R(\mathbf{X}) = \mathbf{G}_0^T (\mathbf{X} - \mathbf{X}_0), \quad (3.5.6)$$

where

$$\mathbf{G} = \nabla G = \left(\frac{\partial G}{\partial X_1}, \frac{\partial G}{\partial X_2}, \dots, \frac{\partial G}{\partial X_n} \right)^T, \quad (3.5.7)$$

Introducing the standardized vector

$$\bar{\mathbf{X}} = s^{-1} (\mathbf{X} - \mathbf{m}), \quad (3.5.8)$$

with

$$\mathbf{m} = E[\mathbf{X}], \quad (3.5.9)$$

and

$$\mathbf{s} = \text{diag}(\sigma_{X_1}, \sigma_{X_2}, \dots, \sigma_{X_n}). \quad (3.5.10)$$

We have

$$\mathbf{X} = \mathbf{s}\bar{\mathbf{X}} + \mathbf{m}, \quad (3.5.11)$$

Substituting Equation (3.5.11) into Equation (3.5.6) gives a linear failure surface in standardized form

$$\bar{R}(\bar{\mathbf{X}}) = \mathbf{G}_0^T \mathbf{s}\bar{\mathbf{X}} + \mathbf{G}_0^T (\mathbf{m} - \mathbf{X}_0) = 0, \quad (3.5.12)$$

and the corresponding safety index is, according to Equation (3.5.4),

$$\beta = \frac{E[\bar{R}(\bar{\mathbf{X}})]}{D[\bar{R}(\bar{\mathbf{X}})]} = \frac{\mathbf{G}_0^T (\mathbf{m} - \mathbf{X})}{(\mathbf{G}_0^T \mathbf{s}^2 \mathbf{G}_0)^{\frac{1}{2}}}. \quad (3.5.13)$$

Let us transform Equation (3.5.12) into

$$-\frac{\text{sign}[\mathbf{G}_0^T (\mathbf{m} - \mathbf{X}_0)]}{(\mathbf{G}_0^T \mathbf{s}^2 \mathbf{G}_0)^{\frac{1}{2}}} \mathbf{G}_0^T \mathbf{s} \bar{\mathbf{X}} - \frac{|\mathbf{G}_0^T (\mathbf{m} - \mathbf{X}_0)|}{(\mathbf{G}_0^T \mathbf{s}^2 \mathbf{G}_0)^{\frac{1}{2}}} = 0. \quad (3.5.14)$$

Comparing with the standard form of a linear surface

$$\mathbf{N}_0^T \bar{\mathbf{X}} - d = 0, \quad (3.5.15)$$

where \mathbf{N}_0 is the unit vector normal to the surface, and $d(\geq 0)$ is the distance from the origin to the surface, we obtain

$$d = \frac{|\mathbf{G}_0^T (\mathbf{m} - \mathbf{X}_0)|}{(\mathbf{G}_0^T \mathbf{s}^2 \mathbf{G}_0)^{\frac{1}{2}}} = |\beta|, \quad (3.5.16)$$

and

$$\mathbf{N}_0^T = -\frac{\text{sign}[\mathbf{G}_0^T (\mathbf{m} - \mathbf{X}_0)]}{(\mathbf{G}_0^T \mathbf{s}^2 \mathbf{G}_0)^{\frac{1}{2}}} \mathbf{G}_0^T \mathbf{s}. \quad (3.5.17)$$

This proves that if \mathbf{X} is an uncorrelated normal vector, the absolute value of safety index in the first order approximation is exactly the distance from the origin to one of the tangent planes of the actual failure surface in the standardized random space. Figure 3.3 gives a graphical interpretation of β for two-dimensional problem.

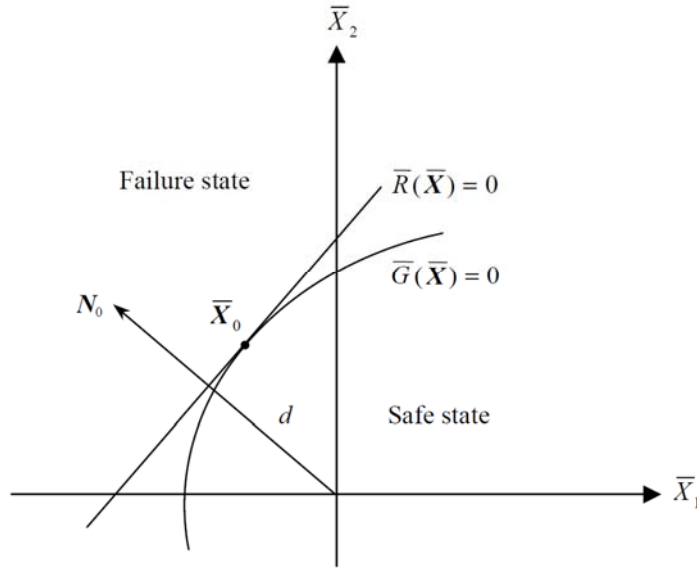


Figure 3.3 Linearization of limit state surface at arbitrary point

Certainly, the linearization of $G(\mathbf{X})$ will induce in P_f a truncation error. If $\bar{G}(\bar{\mathbf{X}})$ is concave to the origin and $\beta > 0$, the error can be expressed by

$$\begin{aligned} \Delta P_f &= \int_{\bar{G}(\bar{\mathbf{x}}) \leq 0} \bar{f}_{\bar{\mathbf{x}}}(\bar{\mathbf{x}}) d\bar{\mathbf{x}} - \int_{\bar{R}(\bar{\mathbf{x}}) \leq 0} \bar{f}_{\bar{\mathbf{x}}}(\bar{\mathbf{x}}) d\bar{\mathbf{x}}, \\ &= P_f - \Phi(-d) \end{aligned} \quad (3.5.18)$$

Where $\bar{f}_{\bar{\mathbf{x}}}(\bar{\mathbf{x}})$ is the joint CDF of the standard normal variables. In order to reduce $|\Delta P_f|$, d should be decreased, hence, the least absolute error $|\Delta P_f|_{\min}$ will be achieved when d is the minimum distance from the origin to the failure surface $\bar{G}(\bar{\mathbf{X}}) = 0$. The corresponding safety index β thus obtained is due to Hasofer and Lind (1974). It has been widely adopted as a practical measure of structural safety, and the relevant point $\bar{\mathbf{X}}^*$ in the standardized random space and its counterpart \mathbf{X}^* in the original space at

which $G(\mathbf{X})=0$ is expanded are termed design point. According to Freudenthal (1956) an effective checking point in design should be the most probable failure point or a point of the maximum likelihood. Design point is such a point in standard space, about which $\bar{f}_{\bar{\mathbf{x}}}(\bar{\mathbf{x}})$ is symmetric. Likewise, the same conclusion can be drawn, when $\beta < 0$ or $G(\mathbf{X})=0$ is convex. For the present case, an interval estimation of P_f is given by Hasofer (1974) as follows

$$\Phi(-\beta) < P_f < 1 - \chi_n^2(\beta^2), \quad (3.5.19)$$

where is the CDF of the chi-square distribution with n degrees of freedom. This is a natural conclusion if we take the safe state as bounded between the space with hyperplane $\bar{R}(\bar{\mathbf{X}}^*)$ and the hyper-sphere of radius β , while noticing the fact that the sum of squares of a set of uncorrelated standard normal variables has a chi-square distribution with n degrees of freedom. Here we assume there is only one design point and that the failure surface is concave to the origin. Figure 3.4 illustrates the implication of design point $\bar{\mathbf{X}}^*$, the Hasofer and Lind safety index β , and the error ΔP_f for two-dimensional problem.

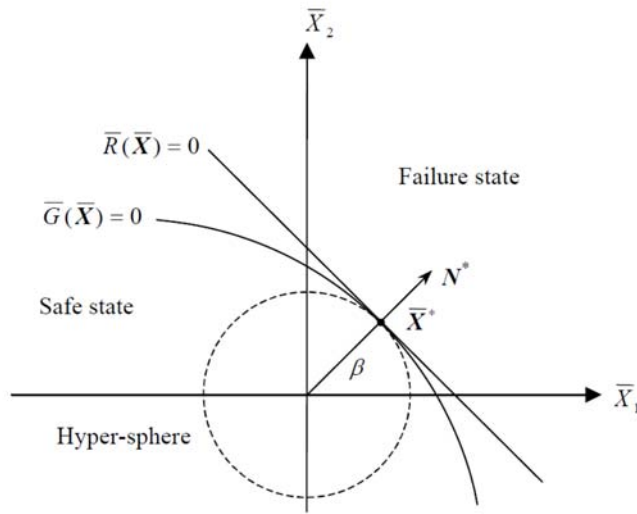


Figure 3.4 Hasofer and Lind reliability index

3.5.2 First-Order Reliability Moment (FORM) Method

For a performance indicator $I = F(Y)$, which is function $F(\cdot)$ of model outputs Y , which are in turn a function $g(P)$ of input parameters P , one can use a multivariate Taylor series approximation of F to obtain the expected value and variance of the indicator:

$$E[I] = F(\text{mean values of input parameter}) + \frac{1}{2} \left\{ \sum_i \sum_j \left[\frac{\partial^2 F}{\partial P_i \partial P_j} \right] \text{Cov}[P_i, P_j] \right\}, \quad (3.5.20)$$

and

$$\text{Var}[I] = \sum_i \sum_j \left(\frac{\partial F}{\partial P_i} \right) \left(\frac{\partial F}{\partial P_j} \right) \text{Cov}[P_i, P_j], \quad (3.5.21)$$

where $\frac{\partial F}{\partial P_i}$ are the partial derivatives of the function F with respect to P_i evaluated at the mean value of the input parameters P_i , and $\frac{\partial^2 F}{\partial P_i \partial P_j}$ are the second partial derivatives. The covariance of two random input parameter P_i and P_j is the expected value of the product of differences between the values and their means:

$$\text{Cov}[P_i, P_j] = E\left[(P_i - E[P_i])(P_j - E[P_j])\right]. \quad (3.5.22)$$

If all the parameters are independent of each other, and the second-order terms in the expression for the mean $E[I]$ are neglected, one obtains

$$E[I] = F(\text{mean values of input parameter}), \quad (3.5.23)$$

and

$$\text{Var}[I] = \sum_i \sum_j \left(\frac{\partial F}{\partial P_i}\right)^2 \text{Var}[P_i]. \quad (3.5.24)$$

For a given function g of a random variable vector \mathbf{X} which has normal distribution, it can be approximated about mean as

$$\tilde{g}(\mathbf{X}) \approx g(\mathbf{X})\Big|_{\mathbf{X}=\boldsymbol{\mu}_X} + \frac{dg}{d\mathbf{X}}\Big|_{\mathbf{X}=\boldsymbol{\mu}_X}^T (\mathbf{X} - \boldsymbol{\mu}_X), \quad (3.5.25)$$

Then the mean and standard deviation are easy to show

$$\mu_{\tilde{g}} = g(\boldsymbol{\mu}_X), \text{ and } \sigma_{\tilde{g}} = \left[\frac{dg}{d\mathbf{X}}\Big|_{\mathbf{X}=\boldsymbol{\mu}_X}^T \boldsymbol{\Sigma} \frac{dg}{d\mathbf{X}}\Big|_{\mathbf{X}=\boldsymbol{\mu}_X} \right]^{1/2}. \quad (3.5.26)$$

where $\boldsymbol{\Sigma}$ is the covariance matrix.

$$\Sigma = \begin{bmatrix} E[(X_1 - \mu_1)(X_1 - \mu_1)] & E[(X_1 - \mu_1)(X_2 - \mu_2)] & \cdots & E[(X_1 - \mu_1)(X_n - \mu_n)] \\ E[(X_2 - \mu_2)(X_1 - \mu_1)] & E[(X_2 - \mu_2)(X_2 - \mu_2)] & & \\ \vdots & & \ddots & \\ E[(X_n - \mu_n)(X_1 - \mu_1)] & & & E[(X_n - \mu_n)(X_n - \mu_n)] \end{bmatrix}. \quad (3.5.27)$$

If all the parameter are independent of each other, only the diagonal terms are left.

Chapter 4. Design Sensitivity Analysis

In this chapter, we review the design sensitivity analysis methodology of molecular dynamics by using an adjoint variable method (AVM). Furthermore, to evaluate the effect of uncertainty to MD simulation and DSA of MD, we develop an analytical design sensitivity method considering the uncertainty. The impact of uncertainty to the predictions of MD simulation and DSA of MD is estimated based on the developed design sensitivity method by utilizing the FORM concept.

In *Section 4.1*, design sensitivity analysis methods for NVE and NVT ensemble MD systems are presented. Some numerical aspects in practical applications are discussed. In *Section 4.2*, the developed design sensitivity method considering uncertainty in MD system is suggested. The variance of performance measure in MD simulation and sensitivity of MD is obtained through FORM analysis based on the developed method. In *Section 4.3*, reliability analysis based sensitivity analysis is introduced for robust and reliable design of MD system.

4.1 Design sensitivity analysis of MD

4.1.1 Adjoint variable method for NVE ensemble

From Equation (2.1.3) for MD systems, the equations of motion can be written, in a matrix-vector form, as

$$\mathbf{M}_A(\mathbf{b})\ddot{\mathbf{u}} = \mathbf{f}(\mathbf{b}, \mathbf{u}), \quad (4.1.1)$$

where \mathbf{M}_A , \mathbf{u} , and \mathbf{b} are the atomic mass matrix, displacement vector, and design variable vector, respectively. The term $\mathbf{f}(\mathbf{b}, \mathbf{u}) = -\partial U(\mathbf{b}, \mathbf{u})/\partial \mathbf{u}$

is the interaction force calculated from the potential energy $U(\mathbf{b}, \mathbf{u})$. Taking the first order variation of Equation (4.1.1) with respect to the design \mathbf{b} leads to the following design sensitivity equation

$$\mathbf{M}_A(\mathbf{b})\ddot{\mathbf{u}}' - \frac{\partial \mathbf{f}(\mathbf{b}, \mathbf{u})}{\partial \mathbf{u}} \mathbf{u}' = -\frac{\partial \mathbf{M}_A(\mathbf{b})}{\partial \mathbf{b}} \delta \mathbf{b} \ddot{\mathbf{u}} + \frac{\partial \mathbf{f}(\mathbf{b}, \mathbf{u})}{\partial \mathbf{b}} \delta \mathbf{b}. \quad (4.1.2)$$

Since the initial conditions are independent of design, the corresponding initial conditions for the design sensitivity are selected as

$$\mathbf{u}'(0) = \dot{\mathbf{u}}'(0) = \mathbf{0}. \quad (4.1.3)$$

For a general performance measure that could include both terminal value and time history quantity for the MD system,

$$\psi = g(\mathbf{b}, \mathbf{u}, \dot{\mathbf{u}}) \Big|_{t=t_r} + \int_0^{t_r} h(\mathbf{b}, \mathbf{u}, \dot{\mathbf{u}}) dt, \quad (4.1.4)$$

taking the first order variation of Equation (4.1.4) with respect to the design \mathbf{b} and integrating the last term in the integrand by parts lead to

$$\begin{aligned} \psi' &= \left(\frac{\partial g}{\partial \mathbf{b}} \delta \mathbf{b} + \frac{\partial g}{\partial \mathbf{u}} \mathbf{u}' + \frac{\partial g}{\partial \dot{\mathbf{u}}} \dot{\mathbf{u}}' \right) \Big|_{t=t_r} + \int_0^{t_r} \left(\frac{\partial h}{\partial \mathbf{b}} \delta \mathbf{b} + \frac{\partial h}{\partial \mathbf{u}} \mathbf{u}' + \frac{\partial h}{\partial \dot{\mathbf{u}}} \dot{\mathbf{u}}' \right) dt \\ &= \left\{ \frac{\partial g}{\partial \mathbf{b}} \delta \mathbf{b} + \left(\frac{\partial g}{\partial \mathbf{u}} + \frac{\partial h}{\partial \mathbf{u}} \right) \mathbf{u}' + \frac{\partial g}{\partial \dot{\mathbf{u}}} \dot{\mathbf{u}}' \right\} \Big|_{t=t_r} + \int_0^{t_r} \left\{ \frac{\partial h}{\partial \mathbf{b}} \delta \mathbf{b} + \left(\frac{\partial h}{\partial \mathbf{u}} - \frac{d}{dt} \frac{\partial h}{\partial \dot{\mathbf{u}}} \right) \mathbf{u}' \right\} dt. \end{aligned} \quad (4.1.5)$$

Note that the notation $(\bullet)' = \frac{d(\bullet)}{d\mathbf{b}} \delta \mathbf{b}$. For the Lagrange multiplier function λ , the equation of motion should hold for all time spans.

$$\int_0^{t_r} \lambda^T (\mathbf{M}_A(\mathbf{b})\ddot{\mathbf{u}} - \mathbf{f}(\mathbf{b}, \mathbf{u})) dt = 0. \quad (4.1.6)$$

Assuming that the Lagrange multiplier function or adjoint response λ is independent of design \mathbf{b} , the first order variation of Equation (4.1.6) is obtained as

$$\int_0^{t_r} \lambda^T \left(\frac{\partial \mathbf{M}_A(\mathbf{b})}{\partial \mathbf{b}} \delta \mathbf{b} \ddot{\mathbf{u}} + \mathbf{M}_A(\mathbf{b}) \ddot{\mathbf{u}}' - \frac{\partial \mathbf{f}(\mathbf{b}, \mathbf{u})}{\partial \mathbf{b}} \delta \mathbf{b} - \frac{\partial \mathbf{f}(\mathbf{b}, \mathbf{u})}{\partial \mathbf{u}} \mathbf{u}' \right) dt = 0. \quad (4.1.7)$$

Integration by parts and using the initial conditions $\mathbf{u}'(0) = \dot{\mathbf{u}}'(0) = 0$, we obtain the following.

$$\begin{aligned} & \left(\lambda^T \mathbf{M}_A \dot{\mathbf{u}}' - \dot{\lambda}^T \mathbf{M}_A \mathbf{u}' \right) \Big|_{t=0}^{t=t_r} + \int_0^{t_r} \left(\dot{\lambda}^T \mathbf{M}_A - \lambda^T \frac{\partial \mathbf{f}(\mathbf{b}, \mathbf{u})}{\partial \mathbf{u}} \right) \mathbf{u}' dt \\ & = - \int_0^{t_r} \lambda^T \left(\frac{\partial \mathbf{M}_A}{\partial \mathbf{b}} \ddot{\mathbf{u}} - \frac{\partial \mathbf{f}(\mathbf{b}, \mathbf{u})}{\partial \mathbf{b}} \right) \delta \mathbf{b} dt \end{aligned} \quad (4.1.8)$$

Comparing Equation (4.1.8) with Equation (4.1.5), an adjoint system is defined as

$$\mathbf{M}_A(\mathbf{b}) \ddot{\lambda} - \frac{\partial \mathbf{f}(\mathbf{b}, \mathbf{u})}{\partial \mathbf{u}} \lambda = \left(\frac{\partial h}{\partial \mathbf{u}} - \frac{d}{dt} \frac{\partial h}{\partial \dot{\mathbf{u}}} \right)^T, \quad (4.1.9)$$

where the corresponding terminal conditions are given as

$$\lambda(t_r) = \mathbf{M}_A^{-1}(\mathbf{b}) \frac{\partial g}{\partial \dot{\mathbf{u}}} \quad \text{and} \quad \dot{\lambda}(t_r) = -\mathbf{M}_A^{-1}(\mathbf{b}) \left(\frac{\partial g}{\partial \mathbf{u}} + \frac{\partial h}{\partial \dot{\mathbf{u}}} \right)^T. \quad (4.1.10)$$

Thus, the adjoint design sensitivity can be obtained by using the analysis and adjoint responses,

$$\psi' = \frac{\partial g}{\partial \mathbf{b}} \delta \mathbf{b} \Big|_{t=t_r} + \int_0^{t_r} \left\{ \frac{\partial h}{\partial \mathbf{b}} - \lambda^T \left(\frac{\partial \mathbf{M}_A}{\partial \mathbf{b}} \ddot{\mathbf{u}} - \frac{\partial \mathbf{f}(\mathbf{b}, \mathbf{u})}{\partial \mathbf{b}} \right) \right\} \delta \mathbf{b} dt. \quad (4.1.11)$$

Thus, the design sensitivity of general performance measure can be obtained using the original response in Equation (2.1.3) and the adjoint response in

Equation (4.1.9) with the terminal conditions of Equation (4.1.10). Note that if the adjoint system is reversible, we can obtain the adjoint response by time integrating the adjoint system in forward direction by changing the sign of the terminal velocity. Even if the original MD system has time reversal symmetry, the time reversibility of adjoint system is not related to the reversibility of the original one but to the type of performance measure

4.1.2 Adjoint variable method for NVT ensemble

The derivation of AVM for the NVT ensemble is similar to that for the NVE ensemble derived in section 4.1.1. The difference is that there is an additional degree of freedom for thermostat variable in both extended Hamiltonian and equations of motion. A general performance measure ψ of Nose-Hoover thermostat can be defined including both terminal time value and time history quantity as

$$\psi = g(\mathbf{b}, \zeta, \mathbf{q}, \dot{\mathbf{q}}) \Big|_{t=t_r} + \int_0^{t_r} h(\mathbf{b}, \zeta, \mathbf{q}, \dot{\mathbf{q}}) dt . \quad (4.1.12)$$

Taking the first order variation of Equation (4.1.12) with respect to design \mathbf{b} and integrating by parts lead to

$$\begin{aligned} \psi' = & \left(\frac{\partial g}{\partial \mathbf{b}} \delta \mathbf{b} + \frac{\partial g}{\partial \zeta} \zeta' + \left(\frac{\partial g}{\partial \mathbf{q}} + \frac{\partial h}{\partial \dot{\mathbf{q}}} \right) \mathbf{q}' + \frac{\partial g}{\partial \dot{\mathbf{q}}} \dot{\mathbf{q}}' \right) \Big|_{t=t_r} \\ & + \int_0^{t_r} \left(\frac{\partial h}{\partial \mathbf{b}} \delta \mathbf{b} + \frac{\partial h}{\partial \zeta} \zeta' + \left(\frac{\partial h}{\partial \mathbf{q}} - \frac{d}{dt} \frac{\partial h}{\partial \dot{\mathbf{q}}} \right) \mathbf{q}' \right) dt . \end{aligned} \quad (4.1.13)$$

Equations of motion for Nose-Hoover thermostat can be re-written in matrix-vector form for convenience as

$$\mathbf{m}_A \ddot{\mathbf{q}}(t) = \mathbf{f} - \zeta(t) \mathbf{m}_A \dot{\mathbf{q}}(t), \quad (4.1.14)$$

$$Q\dot{\zeta}(t) = \dot{\mathbf{q}}(t)^T \mathbf{m}_A \dot{\mathbf{q}}(t) - z, \quad z = 3Nk_B T . \quad (4.1.15)$$

Two adjoint variables $\boldsymbol{\lambda}(t)$ and $\xi(t)$ is introduced. Note that $\boldsymbol{\lambda}(t)$ is a vector function whereas $\xi(t)$ is a scalar function. Multiplying adjoint variables and integrating with respect to time, we have

$$\int_0^{t_r} \boldsymbol{\lambda}^T (\mathbf{m}_A(\mathbf{b})\ddot{\mathbf{q}} - \mathbf{f}(\mathbf{b}, \mathbf{q}) + \mathbf{m}_A(\mathbf{b})\zeta\dot{\mathbf{q}}) dt + \int_0^{t_r} \xi (Q(\mathbf{b})\dot{\zeta} - \dot{\mathbf{q}}^T \mathbf{m}_A(\mathbf{b})\dot{\mathbf{q}} + z(\mathbf{b})) dt = 0. \quad (4.1.16)$$

Assuming that the Lagrange multipliers are independent of design, taking first order variation of the Equation (4.1.16) and integrating by parts yields

$$\begin{aligned} & \left(\boldsymbol{\lambda}^T \mathbf{m}_A \dot{\mathbf{q}}' + (\boldsymbol{\lambda}^T \zeta \mathbf{m}_A - \dot{\boldsymbol{\lambda}}^T \mathbf{m}_A - 2\xi \dot{\mathbf{q}}^T \mathbf{m}_A) \mathbf{q}' + \xi Q \zeta' \right) \Big|_{t=0}^{t=t_r} \\ & + \int_0^{t_r} \left(\ddot{\boldsymbol{\lambda}}^T \mathbf{m}_A - \boldsymbol{\lambda}^T \frac{\partial \mathbf{f}}{\partial \mathbf{q}} - \dot{\boldsymbol{\lambda}}^T \zeta \mathbf{m}_A - \boldsymbol{\lambda}^T \dot{\zeta} \mathbf{m}_A + 2\xi \ddot{\mathbf{q}}^T \mathbf{m}_A + 2\dot{\xi} \dot{\mathbf{q}}^T \mathbf{m}_A \right) \mathbf{q}' dt \\ & + \int_0^{t_r} (\boldsymbol{\lambda}^T \mathbf{m}_A \dot{\mathbf{q}} - \dot{\xi} Q) \zeta' dt \\ & = - \int_0^{t_r} \left\{ \boldsymbol{\lambda}^T \left(\frac{\partial \mathbf{m}_A}{\partial \mathbf{b}} \ddot{\mathbf{q}} - \frac{\partial \mathbf{f}}{\partial \mathbf{b}} + \frac{\partial \mathbf{m}_A}{\partial \mathbf{b}} \zeta \dot{\mathbf{q}} \right) + \xi \left(\frac{\partial z}{\partial \mathbf{b}} + \frac{\partial Q}{\partial \mathbf{b}} \dot{\zeta} - \dot{\mathbf{q}}^T \frac{\partial \mathbf{m}_A}{\partial \mathbf{b}} \dot{\mathbf{q}} \right) \right\} \delta \mathbf{b} dt. \end{aligned} \quad (4.1.17)$$

Matching the resulting identity of Equation (4.1.17) with Equation (4.1.13), we can obtain the following adjoint system with corresponding terminal conditions for NVT ensemble MD systems.

$$\begin{aligned} \ddot{\boldsymbol{\lambda}} &= \zeta \dot{\boldsymbol{\lambda}} + \mathbf{m}_A^{-1} \frac{\partial \mathbf{f}}{\partial \mathbf{q}} \boldsymbol{\lambda} + \dot{\zeta} \boldsymbol{\lambda} - 2\xi \ddot{\mathbf{q}} \\ & - 2\dot{\xi} \dot{\mathbf{q}} + \mathbf{m}_A^{-1} \left(\frac{\partial h}{\partial \mathbf{q}} - \frac{d}{dt} \frac{\partial h}{\partial \dot{\mathbf{q}}} \right)^T, \end{aligned} \quad (4.1.18)$$

$$\dot{\xi} = \frac{1}{Q} \left(\boldsymbol{\lambda}^T \mathbf{m}_A \dot{\mathbf{q}} - \frac{\partial h}{\partial \zeta} \right), \quad (4.1.19)$$

$$\xi(t_T) = \frac{1}{Q} \frac{\partial g}{\partial \zeta}, \quad (4.1.20)$$

$$\lambda(t_T) = \mathbf{m}_A^{-1} \left(\frac{\partial g}{\partial \dot{\mathbf{q}}} \right)^T, \quad (4.1.21)$$

$$\dot{\lambda}(t_T) = \mathbf{m}_A^{-1} \left\{ \zeta \left(\frac{\partial g}{\partial \dot{\mathbf{q}}} \right)^T - \left(\frac{\partial g}{\partial \mathbf{q}} + \frac{\partial h}{\partial \dot{\mathbf{q}}} \right)^T \right\} - \frac{2}{Q} \left(\frac{\partial g}{\partial \zeta} \right) \dot{\mathbf{q}}. \quad (4.1.22)$$

Thus, the adjoint design sensitivity can be obtained by using the analysis and adjoint responses,

$$\begin{aligned} \psi' = & \frac{\partial g}{\partial \mathbf{b}} \delta \mathbf{b} \Big|_{t=t_T} + \int_0^{t_T} \frac{\partial h}{\partial \mathbf{b}} \delta \mathbf{b} dt \\ & - \int_0^{t_T} \left\{ \lambda^T \left(\frac{\partial \mathbf{m}_A}{\partial \mathbf{b}} (\ddot{\mathbf{q}} + \zeta \dot{\mathbf{q}}) - \frac{\partial \mathbf{f}}{\partial \mathbf{b}} \right) + \xi \left(\frac{\partial z}{\partial \mathbf{b}} + \frac{\partial Q}{\partial \mathbf{b}} \dot{\zeta} - \dot{\mathbf{q}}^T \frac{\partial \mathbf{m}_A}{\partial \mathbf{b}} \dot{\mathbf{q}} \right) \right\} \delta \mathbf{b} dt. \end{aligned} \quad (4.1.23)$$

4.1.3 Discontinuity problems introduced by cut-off

A cutoff introduces a discontinuity in both the potential energy and the force near the cutoff value. This creates problems, especially in molecular dynamics simulations where energy conservation is required. In the context of design sensitivity analysis this discontinuity also creates problems when evaluating sensitivities. There are several ways to overcome this issue. We have compared three numerical treatment techniques often used in MD simulation for improving the energy conservation and stability of time integration scheme. One approach is to use a shifted potential, in which a constant term is subtracted from the potential at all values.

$$\begin{aligned}\Phi'(r) &= \Phi(r) - \Phi(r_c) & r \leq r_c \\ \Phi'(r) &= 0 & r > r_c\end{aligned}, \quad (4.1.24)$$

where r_c is cutoff radius. As the additional term is constant, it appears when the potential is differentiated and so does not affect the force calculation in molecular dynamics. Use of the “shifted potential” does improve energy conservation, however, there is an additional problem in discontinuity of force calculated with the shifted potential. This can also give instabilities in a simulation. To avoid this, a linear term can be added to the potential, making the derivative zero at the cutoff (Park et al. 2005).

$$\begin{aligned}\Phi'(r) &= \Phi(r) - \Phi(r_c) - \left. \frac{d\Phi}{dr} \right|_{r=r_c} (r - r_c) & r \leq r_c \\ \Phi'(r) &= 0 & r > r_c\end{aligned}. \quad (4.1.25)$$

The shifted potential in Equation (4.1.25) is called the “shifted-force potential”.

An alternative way to eliminate discontinuities in the energy and force equations is to use a switching function $S(r)$ as

$$\Phi'(r) = \Phi(r)S(r). \quad (4.1.26)$$

An acceptable switching function smoothly changes from a value of 1 to a value of 0 between two cutoff r_l and r_u and satisfies the following requirements

$$S_{r=r_l} = 1, \quad \left(\frac{dS}{dr} \right)_{r=r_l} = 0, \quad \left(\frac{d^2S}{dr^2} \right)_{r=r_l} = 0, \quad (4.1.27)$$

$$S_{r=r_u} = 0, \quad \left(\frac{dS}{dr} \right)_{r=r_u} = 0, \quad \left(\frac{d^2S}{dr^2} \right)_{r=r_u} = 0. \quad (4.1.28)$$

By ensuring that the first derivative is zero at the endpoints the force also approaches zero smoothly. A continuous second derivative is required to ensure that the integration algorithm works properly for both MD simulation and sensitivity equations. If the switch function is assumed to take the following form

$$\begin{aligned}
 S(r) & \\
 &= c_0 + c_1 \left[\frac{r-r_l}{r_u-r_l} \right] + c_2 \left[\frac{r-r_l}{r_u-r_l} \right]^2 + c_3 \left[\frac{r-r_l}{r_u-r_l} \right]^3 + c_4 \left[\frac{r-r_l}{r_u-r_l} \right]^4 + c_5 \left[\frac{r-r_l}{r_u-r_l} \right]^5
 \end{aligned}
 \tag{4.1.29}$$

then the following values of coefficients c_0, \dots, c_5 satisfy the six requirements in Equations (4.1.27) and (4.1.28) (Leach 1996),

$$c_0 = 1, \quad c_1 = c_2 = 0, \quad c_3 = -10, \quad c_4 = 15, \quad c_5 = -6.
 \tag{4.1.30}$$

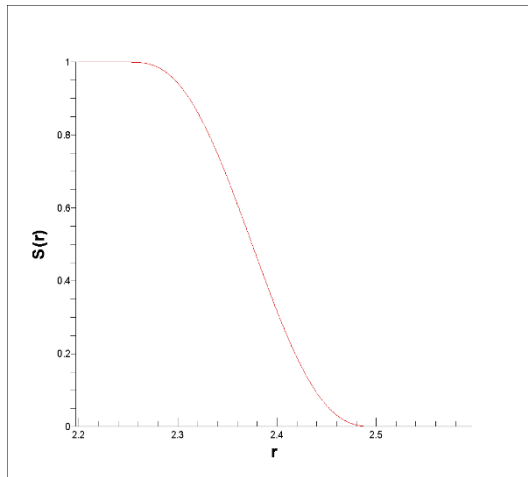


Figure 4.1 Switching function $S(r)$ ($r_l = 2.25$ and $r_u = 2.5$)

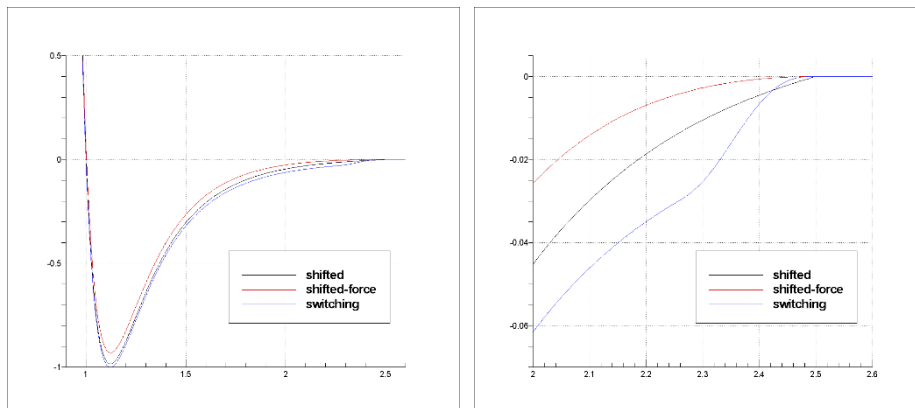
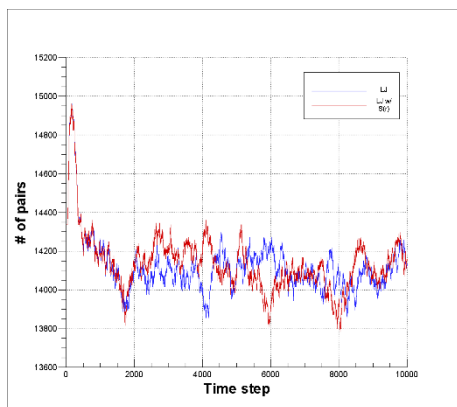
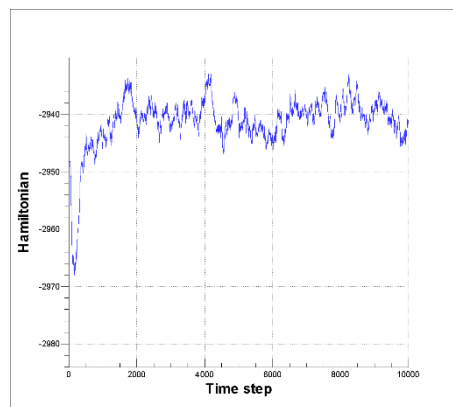


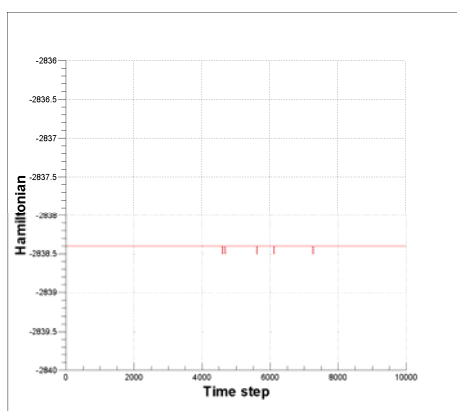
Figure 4.2 Shifted and shifted-force potential and potential with switching function



(a) number of interatomic pairs



(b) standard LJ potential



(c) with switching function

Figure 4.3 Conservation of total energy

The shifted, shifted-force, and switched potentials denote the function of distance r which have C^0 , C^1 , and C^2 continuities near the cutoff respectively. The potential, force and force derivative are given in Figure 4.4. One can easily see the discontinuities near the cutoff.

To investigate the effect of truncated potential to the sensitivity, we performed a simple MD simulation and DSA. As shown in Figure 4.5, 512 argon gas with a simple cubic lattice structure is considered and periodic boundary condition is imposed with cutoff radius $r_c = 2.5\sigma$. The Lennard-Jones 12-6 potential in Equation (2.2.2) is used for describing interaction between atoms. Performance measure is selected as the terminal time diffusivity which is derived as

$$\psi = \frac{1}{3N} \mathbf{u}^T \dot{\mathbf{u}} \Big|_{t=t_T} . \quad (4.1.31)$$

We compared the design sensitivity of terminal time ($t_T = 10,000\Delta t$, $\Delta t = 10^{-3}$ (ps)) diffusivity with respect to the atomic mass m obtained from the FDM and DDM as shown in Figure 4.6. The switched potential (black solid line) show good agreement of numerical (FDM) and analytical (DDM) sensitivities in the interval of $10^{-13} \leq \delta m / m \leq 10^{-11}$ whereas the shifted and shifted-force potentials do not. Due to the long-time evolution and high nonlinearity of the system, the FDM can give inaccurate results with respect to the design perturbation amount. Of course, when the switched potential is utilized, the agreement between the numerical and analytical sensitivities is better than the results from the other potentials in appropriate interval of design perturbation amount.

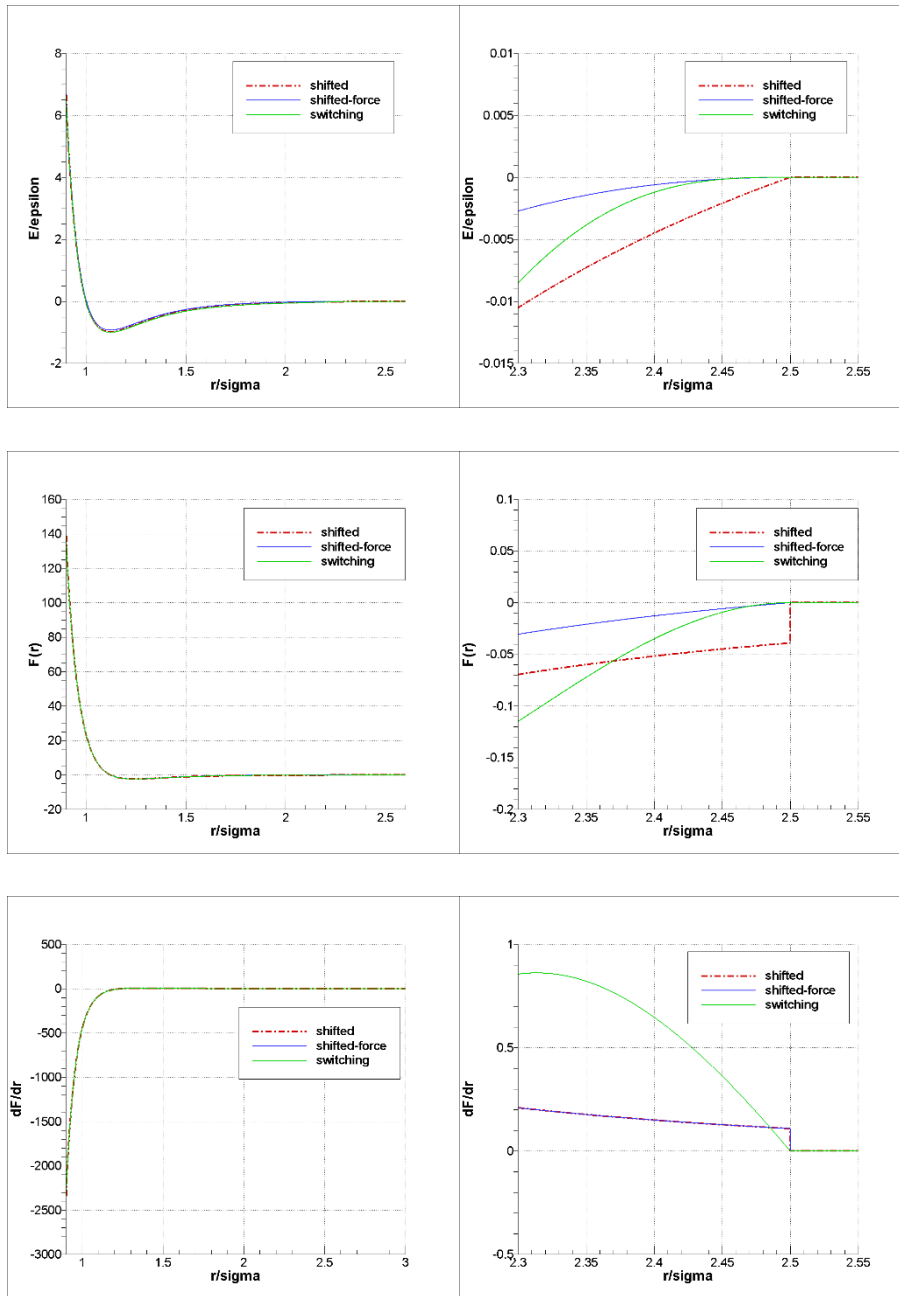
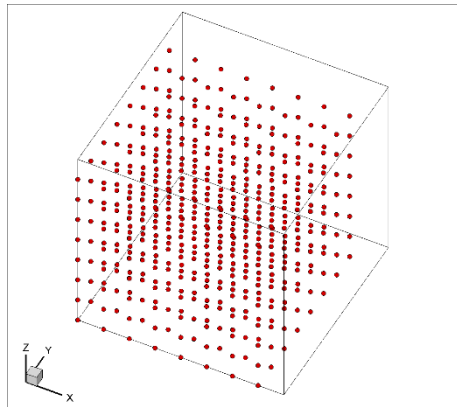
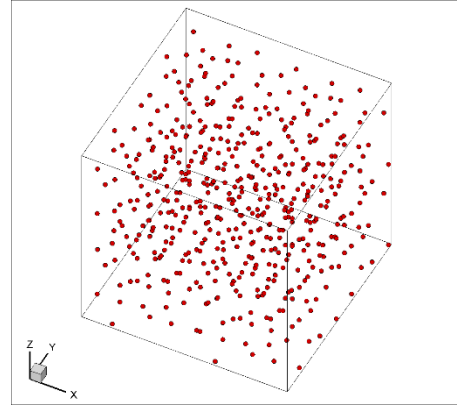


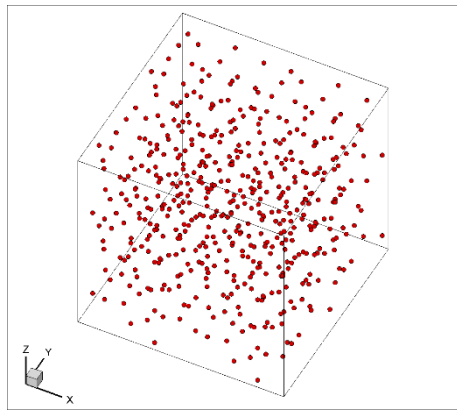
Figure 4.4 Comparison of the three numerical techniques. (top) potential (mid) force and (bottom) 1st order derivative of force



(a) $0\Delta t$



(b) $5,000\Delta t$



(c) $10,000\Delta t$

Figure 4.5 Diffusion of argon gas in NVE ensemble

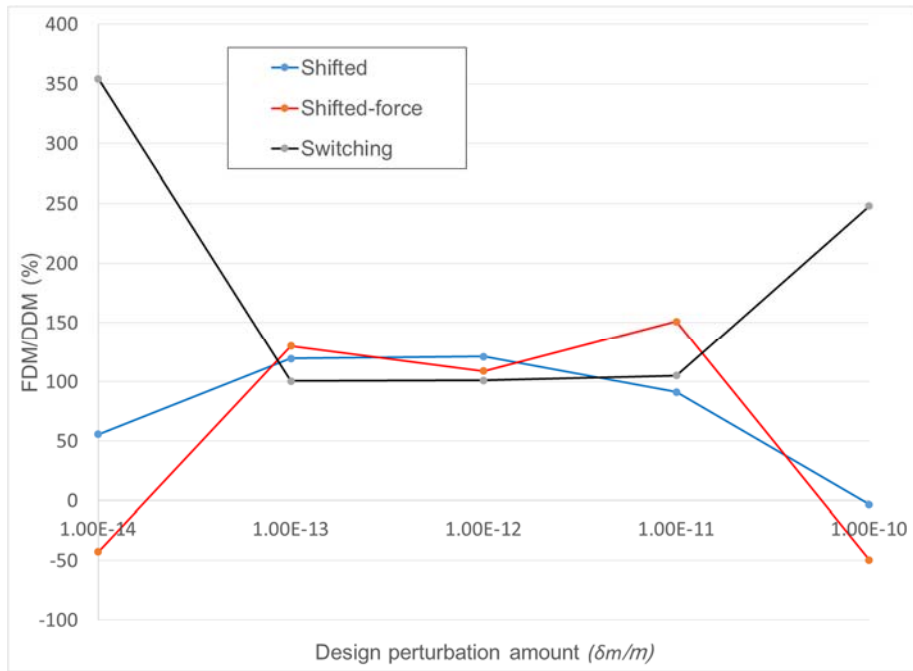


Figure 4.6 Numerical study of design perturbation amount.

4.2 Design Sensitivity Analysis considering Uncertainty

4.2.1 FORM based approach

One can evaluate the impact on the performance measure in MD simulation due to the uncertainty in various parameters based on its sensitivity. As shown below, the impact depends upon the square of the sensitivity coefficients and the variances and covariance of the parameter sets. For a performance measure ψ of a random variable vector \mathbf{X} which is normal can be approximated about mean by Taylor expansion as

$$\tilde{\psi}(\mathbf{X}) \approx \psi(\mathbf{X}) \Big|_{\substack{\mathbf{X}=\boldsymbol{\mu}_X \\ \mathbf{b}=\mathbf{b}_0}} + \frac{d\psi}{d\mathbf{X}} \Big|_{\substack{\mathbf{X}=\boldsymbol{\mu}_X \\ \mathbf{b}=\mathbf{b}_0}}^T (\mathbf{X} - \boldsymbol{\mu}_X), \quad (4.2.1)$$

where \mathbf{b} is design variable.

Then the mean and standard derivation are easy to show as

$$\mu_{\tilde{\psi}} = \psi(\mathbf{X}) \Big|_{\substack{\mathbf{X}=\boldsymbol{\mu}_X \\ \mathbf{b}=\mathbf{b}_0}}, \text{ and } \sigma_{\tilde{\psi}} = \left[\frac{d\psi}{d\mathbf{X}} \Big|_{\substack{\mathbf{X}=\boldsymbol{\mu}_X \\ \mathbf{b}=\mathbf{b}_0}}^T \boldsymbol{\Sigma} \frac{d\psi}{d\mathbf{X}} \Big|_{\substack{\mathbf{X}=\boldsymbol{\mu}_X \\ \mathbf{b}=\mathbf{b}_0}} \right]^{1/2}, \quad (4.2.2)$$

where $\boldsymbol{\Sigma}$ is the covariance matrix

$$\boldsymbol{\Sigma} = \begin{bmatrix} E[(X_1 - \mu_1)(X_1 - \mu_1)] & E[(X_1 - \mu_1)(X_2 - \mu_2)] & \cdots & E[(X_1 - \mu_1)(X_n - \mu_n)] \\ E[(X_2 - \mu_2)(X_1 - \mu_1)] & E[(X_2 - \mu_2)(X_2 - \mu_2)] & & \\ \vdots & & \ddots & \\ E[(X_n - \mu_n)(X_1 - \mu_1)] & & & E[(X_n - \mu_n)(X_n - \mu_n)] \end{bmatrix}. \quad (4.2.3)$$

We can employ the same concept for the effect of uncertainty to the sensitivity in the DSA of MD simulation. For a sensitivity $\frac{d\psi}{d\mathbf{b}}$, the Taylor expansion can be written as

$$\frac{d\tilde{\psi}}{d\mathbf{b}}(\mathbf{X}) \approx \left. \frac{d\psi}{d\mathbf{b}}(\mathbf{X}) \right|_{\substack{\mathbf{X}=\boldsymbol{\mu}_X \\ \mathbf{b}=\mathbf{b}_0}} + \left. \frac{d^2\psi}{d\mathbf{b}d\mathbf{X}} \right|_{\substack{\mathbf{X}=\boldsymbol{\mu}_X \\ \mathbf{b}=\mathbf{b}_0}}^T (\mathbf{X} - \boldsymbol{\mu}_X). \quad (4.2.4)$$

The mean and standard deviation of design sensitivity are obtained as

$$\mu_{\tilde{\psi}} = \left. \frac{d\psi}{d\mathbf{b}}(\mathbf{X}) \right|_{\substack{\mathbf{X}=\boldsymbol{\mu}_X \\ \mathbf{b}=\mathbf{b}_0}}, \text{ and } \sigma_{\tilde{\psi}} = \left[\left. \frac{d^2\psi}{d\mathbf{b}d\mathbf{X}} \right|_{\substack{\mathbf{X}=\boldsymbol{\mu}_X \\ \mathbf{b}=\mathbf{b}_0}}^T \boldsymbol{\Sigma} \left. \frac{d^2\psi}{d\mathbf{b}d\mathbf{X}} \right|_{\substack{\mathbf{X}=\boldsymbol{\mu}_X \\ \mathbf{b}=\mathbf{b}_0}} \right]^{1/2}. \quad (4.2.5)$$

Here, the second order sensitivity with respect to the random and design variable is necessary to obtain the standard deviation of the design sensitivity due to the uncertainty.

4.2.2 Design sensitivity considering uncertainty in MD simulation

From Equation (2.1.3) for MD systems, the equations of motion for Microcanonical (NVE) ensemble considering the uncertainty can be written, in a matrix-vector form, as

$$\mathbf{M}_A(\mathbf{b}, \mathbf{x}) \ddot{\mathbf{u}} = \mathbf{f}(\mathbf{b}, \mathbf{x}, \mathbf{u}), \quad (4.2.6)$$

where \mathbf{M}_A , \mathbf{u} , \mathbf{b} , and \mathbf{x} are the atomic mass matrix, displacement vector, design variable vector, and random variable vector respectively. As shown in Equation (4.2.1) and (4.2.2), to evaluate the effect of uncertainty to the performance measure in MD simulation we need the design sensitivity with respect to the random variable. Therefore, taking the first order variation with respect to random variable \mathbf{x}

$$\mathbf{M} \frac{d\ddot{\mathbf{u}}}{d\mathbf{x}} = \frac{\partial \mathbf{f}}{\partial \mathbf{x}} + \frac{\partial \mathbf{f}}{\partial \mathbf{u}} \frac{d\mathbf{u}}{d\mathbf{x}} - \frac{\partial \mathbf{M}}{\partial \mathbf{x}} \ddot{\mathbf{u}}. \quad (4.2.7)$$

The derivation for the canonical (NVT) ensemble is similar to that for the NVE ensemble. The difference is that there is an additional degree of freedom for thermostat variable in both extended Hamiltonian and equations of motion. Equations of motion for Nose-Hoover thermostat can be re-written in matrix-vector form for convenience as

$$\mathbf{M}_A \ddot{\mathbf{u}}(t) = \mathbf{f}(\mathbf{u}) - \zeta(t) \mathbf{M}_A \dot{\mathbf{u}}(t), \quad (4.2.8)$$

$$Q \dot{\zeta}(t) = \dot{\mathbf{u}}(t)^T \mathbf{M}_A \dot{\mathbf{u}}(t) - z, \quad z = 3Nk_B T. \quad (4.2.9)$$

Again, taking the first order variation with respect to the random variable \mathbf{x}

$$\ddot{\mathbf{u}}_{,x} = \mathbf{M}_A^{-1} \frac{\partial \mathbf{f}}{\partial \mathbf{u}} \mathbf{u}_{,x} - \dot{\zeta} \dot{\mathbf{u}}_{,x} - \zeta_{,x} \dot{\mathbf{u}} + \mathbf{M}_A^{-1} \mathbf{f}_{,x}, \quad (4.2.10)$$

$$\dot{\zeta}_{,x} = \frac{1}{Q} 2\dot{\mathbf{u}}^T \mathbf{M}_A \dot{\mathbf{u}}_{,x}, \quad z = 3Nk_B T, \quad (4.2.11)$$

and

$$\mathbf{u}_{,x}(0) = \dot{\mathbf{u}}_{,x}(0) = \mathbf{0}, \quad \zeta_{,x}(0) = 0. \quad (4.2.12)$$

4.2.3 Design sensitivity considering uncertainty in DSA of MD

As shown in Equation (4.2.5), to estimate the effect of uncertainty to DSA of MD, the second order sensitivity with respect to the design and random variables is required. For NVE ensemble, taking the first order derivation with respect to the design variable \mathbf{b} and the random variable \mathbf{x}

$$\mathbf{M} \frac{d\ddot{\mathbf{u}}}{d\mathbf{b}} = \frac{\partial \mathbf{f}}{\partial \mathbf{b}} + \frac{\partial \mathbf{f}}{\partial \mathbf{u}} \frac{d\mathbf{u}}{d\mathbf{b}} - \frac{\partial \mathbf{M}}{\partial \mathbf{b}} \ddot{\mathbf{u}}, \quad (4.2.13)$$

$$\mathbf{M} \frac{d\ddot{\mathbf{u}}}{d\mathbf{x}} = \frac{\partial \mathbf{f}}{\partial \mathbf{x}} + \frac{\partial \mathbf{f}}{\partial \mathbf{u}} \frac{d\mathbf{u}}{d\mathbf{x}} - \frac{\partial \mathbf{M}}{\partial \mathbf{x}} \ddot{\mathbf{u}}. \quad (4.2.14)$$

Further, taking the second order derivative with respect to design and random variables we get

$$\begin{aligned} \frac{\partial \mathbf{M}}{\partial \mathbf{b}} \frac{d\ddot{\mathbf{u}}}{dx} + \mathbf{M} \frac{d^2 \ddot{\mathbf{u}}}{dx d\mathbf{b}} = \frac{\partial^2 \mathbf{f}}{\partial \mathbf{x} \partial \mathbf{b}} + \frac{\partial^2 \mathbf{f}}{\partial \mathbf{x} \partial \mathbf{u}} \frac{d\mathbf{u}}{d\mathbf{b}} + \left(\frac{\partial^2 \mathbf{f}}{\partial \mathbf{b} \partial \mathbf{u}} + \frac{\partial^2 \mathbf{f}}{\partial \mathbf{u}^2} \frac{d\mathbf{u}}{d\mathbf{b}} \right) \frac{d\mathbf{u}}{dx} \\ + \frac{\partial \mathbf{f}}{\partial \mathbf{u}} \frac{d^2 \mathbf{u}}{dx d\mathbf{b}} - \frac{\partial^2 \mathbf{M}}{\partial \mathbf{x} \partial \mathbf{b}} \ddot{\mathbf{u}} - \frac{\partial \mathbf{M}}{\partial \mathbf{x}} \frac{d\ddot{\mathbf{u}}}{d\mathbf{b}} \end{aligned} \quad (4.2.15)$$

For the NVT ensemble, taking the first order variation with respect to the design variable \mathbf{b} and the random variable \mathbf{x}

$$\ddot{\mathbf{u}}_{,b} = \mathbf{M}_A^{-1} \frac{\partial \mathbf{f}}{\partial \mathbf{u}} \mathbf{u}_{,b} - \zeta \dot{\mathbf{u}}_{,b} - \zeta_{,b} \dot{\mathbf{u}} + \mathbf{M}_A^{-1} \mathbf{f}_{,b}, \quad (4.2.16)$$

$$\dot{\zeta}_{,b} = \frac{1}{Q} 2\dot{\mathbf{u}}^T \mathbf{M}_A \dot{\mathbf{u}}_{,b}, \quad z = 3Nk_B T, \quad (4.2.17)$$

$$\mathbf{u}_{,b}(0) = \dot{\mathbf{u}}_{,b}(0) = \mathbf{0}, \quad \zeta_{,b}(0) = 0, \quad (4.2.18)$$

and

$$\ddot{\mathbf{u}}_{,x} = \mathbf{M}_A^{-1} \frac{\partial \mathbf{f}}{\partial \mathbf{u}} \mathbf{u}_{,x} - \zeta \dot{\mathbf{u}}_{,x} - \zeta_{,x} \dot{\mathbf{u}} + \mathbf{M}_A^{-1} \mathbf{f}_{,x}, \quad (4.2.19)$$

$$\dot{\zeta}_{,x} = \frac{1}{Q} 2\dot{\mathbf{u}}^T \mathbf{M}_A \dot{\mathbf{u}}_{,x}, \quad z = 3Nk_B T, \quad (4.2.20)$$

$$\mathbf{u}_{,x}(0) = \dot{\mathbf{u}}_{,x}(0) = \mathbf{0}, \quad \zeta_{,x}(0) = 0. \quad (4.2.21)$$

By taking the second order derivative with respect to design and random variables, we get the second order sensitivity as

$$\begin{aligned} \ddot{\mathbf{u}}_{,bx} = \mathbf{M}_A^{-1} \frac{\partial^2 \mathbf{f}}{\partial \mathbf{u}^2} \mathbf{u}_{,x} \mathbf{u}_{,b} + \mathbf{M}_A^{-1} \frac{\partial \mathbf{f}}{\partial \mathbf{u}} \mathbf{u}_{,bx} - \zeta_{,x} \dot{\mathbf{u}}_{,b} - \zeta \dot{\mathbf{u}}_{,bx} \\ - \zeta_{,bx} \dot{\mathbf{u}} - \zeta_{,b} \dot{\mathbf{u}}_{,x} + \mathbf{M}_A^{-1} \mathbf{f}_{,bx} \end{aligned}, \quad (4.2.22)$$

$$\dot{\zeta}_{,bx} = \frac{1}{Q} \left(2\dot{\mathbf{u}}_{,x}^T \mathbf{M}_A \dot{\mathbf{u}}_{,b} + 2\dot{\mathbf{u}}^T \mathbf{M}_A \dot{\mathbf{u}}_{,bx} \right), \quad z = 3Nk_B T, \quad (4.2.23)$$

$$\mathbf{u}_{,bx}(0) = \dot{\mathbf{u}}_{,bx}(0) = \mathbf{0}, \quad \zeta_{,bx}(0) = 0. \quad (4.2.24)$$

4.3 Design sensitivity analysis for reliability analysis

4.3.1 Reliability based design sensitivity analysis

The sensitivity of the failure probability includes two parts: the sensitivity of the failure probability with respect to the distributional parameters $\boldsymbol{\theta}$ of random variables, and the sensitivity of the failure probability with respect to the deterministic design variables \mathbf{b} .

The derivative of the estimated failure probability P_f is obtained using FORM (First-Order Reliability Method) with respect to a parameter, which can be either θ_i or b_i , as

$$\frac{\partial P_f}{\partial \eta} = \frac{\partial \Phi(-\beta)}{\partial \eta} = \frac{\partial \Phi(-\beta)}{\partial \beta} \frac{\partial \beta}{\partial \eta} = -\phi(-\beta) \frac{\partial \beta}{\partial \eta}, \quad (4.3.1)$$

where Φ is cumulative distribution function (CDF) of a normal distribution and ϕ is the standard normal density function. Therefore, the sensitivity of the failure probability is computed as

$$\frac{\partial \beta}{\partial \eta} = \frac{\partial \left(\mathbf{U}^{*T} \mathbf{U} \right)^{1/2}}{\partial \eta} = \frac{1}{\beta} \mathbf{U}^{*T} \frac{\partial \mathbf{U}^*}{\partial \eta}, \quad (4.3.2)$$

where \mathbf{U}^* is the most probable point (MPP) found in the U-space.

The sensitivity of the reliability index with respect to a distributional design variable θ_i can be obtained by substituting $\eta = \theta_i$ and

$\mathbf{U}^* = \mathbf{T}(\mathbf{X}^*, \theta)$ in Equation (4.3.2) as

$$\begin{aligned} \frac{\partial \beta}{\partial \theta_i} &= \frac{1}{\beta} \mathbf{U}^{*T} \left[\frac{\partial \mathbf{T}(\mathbf{X}^*, \theta)}{\partial \theta_i} + \frac{\partial \mathbf{T}(\mathbf{X}^*, \theta)}{\partial \mathbf{X}^*} \frac{\partial \mathbf{X}^*}{\partial \theta_i} \right], \\ &= \frac{1}{\beta} \mathbf{U}^{*T} \frac{\partial \mathbf{T}(\mathbf{X}^*, \theta)}{\partial \theta_i} \end{aligned} \quad (4.3.3)$$

since the second term vanishes.

The reliability index β is the distance between the origin and the MPP in the U-space. The MPP vector \mathbf{U}^* on the failure surface can be written as

$$\mathbf{U}^* = -\beta \frac{\nabla g(\mathbf{U}^*, \mathbf{b})}{|\nabla g(\mathbf{U}^*, \mathbf{b})|}, \quad (4.3.4)$$

where $\nabla g(\mathbf{U}^*, \mathbf{b})$ is the gradient of the failure function at the MPP, i.e.

$$\nabla g(\mathbf{U}^*, \mathbf{b}) = \frac{\partial g(\mathbf{U}^*, \mathbf{b})}{\partial \mathbf{U}}, \quad (4.3.5)$$

The MPP vector \mathbf{U}^* is also a function of \mathbf{b} since the failure function g depends on the deterministic design variable \mathbf{b} . Substituting Equation (4.3.4) into Equation (4.3.2) yields

$$\begin{aligned} \frac{\partial \beta}{\partial \mathbf{b}} &= \frac{1}{\beta} \left[-\beta \frac{\nabla^T g(\mathbf{U}^*, \mathbf{b})}{|\nabla g(\mathbf{U}^*, \mathbf{b})|} \right] \frac{\partial \mathbf{U}^*}{\partial \mathbf{b}} \\ &= - \frac{1}{|\nabla g(\mathbf{U}^*, \mathbf{b})|} \frac{\partial g^T(\mathbf{U}^*, \mathbf{b})}{\partial \mathbf{U}} \frac{\partial \mathbf{U}^*}{\partial \mathbf{b}} \end{aligned} \quad (4.3.6)$$

By taking the derivative of $g(\mathbf{X}^*, \mathbf{b})$ with respect to \mathbf{b} ,

$$\frac{\partial g^T(\mathbf{U}^*, \mathbf{b})}{\partial \mathbf{U}} \frac{\partial \mathbf{U}^*}{\partial \mathbf{b}} + \frac{\partial g(\mathbf{U}^*, \mathbf{b})}{\partial \mathbf{b}} = 0. \quad (4.3.7)$$

Substituting Equation (4.3.7) into Equation (4.3.6) yields

$$\frac{\partial \beta}{\partial \mathbf{b}} = \frac{1}{|\nabla g(\mathbf{U}^*, \mathbf{b})|} \frac{\partial g^T(\mathbf{U}^*, \mathbf{b})}{\partial \mathbf{b}}. \quad (4.3.8)$$

Note that evaluation of Equation (4.3.8) needs only the first-order derivative of the failure function with respect to random variables and deterministic design variables.

Chapter 5. Numerical Examples

In chapter 5, the developed adjoint design sensitivity analysis method is verified through several numerical examples. Furthermore, by utilizing the developed method with in concern of the uncertainties in ensemble and force field parameters, the variances of performance measure and its sensitivity due to such uncertainties are efficiently shown.

In Section 5.1, through a comparative MD simulation and experiment study of nanoparticle synthesis problem, the effect of uncertainty to the prediction of MD simulations is shown. The result of MD simulations are obtained from open source code LAMMPS (Plimpton, 1995). In Section 5.2, we further extend to design optimization problem to find unknown potential parameters between interactions of nanoparticle and nanostructure based on the developed sensitivity. In Section 5.3, a 3-dimensional gas diffusion problem is introduced to evaluate the effect of random atomic mass to both MD simulation and DSA of MD results based on the developed first and second order sensitivities of random and design variables. In Section 5.4, a 1-dimensional harmonic oscillator problem is introduced. By utilizing the developed method, we predict the uncertainty effect from random initial velocity and verify the result with Monte Carlo simulation. We further estimate the sensitivity of reliability index considering random initial velocities. In Section 5.5, the developed method is employed to a practical agglomeration problem of nanoparticles on a substrate. The effect of random initial velocity to both MD simulation and DSA of MD is shown. Furthermore, the efficiency and accuracy of the developed method is shown through comparison of computational cost and sensitivity verification for longer terminal MD simulation time.

5.1 Uncertainty effect in MD simulation

In this section, we demonstrate a comparative experimental and MD simulation study of gold nanoparticles (NPs) green synthesis. Through MD simulations of gold NPs sintering, we show the effect of uncertainty to the prediction and observation. The MD simulations are performed with open source LAMMPS (Plimpton, 1995). To insure the results of MD simulation from the impact of uncertainty, we carry out numerous repetition of MD simulations for each cases and estimate the variance of the performance measure through standard error analysis.

The synthesis of metallic nanoparticles is commonly performed with chemical procedures using toxic chemical reducing agents such as sodium borohydride and hydrazine. Green synthetic methods have recently attracted considerable attention in many fields of research. Chemically synthesized NPs that contain toxic chemicals are a major drawback in the environmental, pharmaceutical, and biomedical applications for which they are needed, while green synthetic approaches have many merits. Green-synthesized NPs are biocompatible and reduce toxic chemical waste, contributing to a more sustainable environment. Various categories of biological entities such as carbohydrates, phytochemicals, plant extracts, fungus, algae, and heterotrophic human cell lines have been introduced to green-synthesize diverse metallic NPs (Park et al., 2011b, Hulkoti and Taranath, 2014). Among NPs, gold nanoparticle (AuNPs) possess numerous advantages, such as low cytotoxicity, facile modification of their surfaces, straightforward synthetic processes, and excellent biocompatibility (Sperling et al., 2008, Yeh et al., 2012). In this example, we performed a comparative study of green synthesis of AuNPs by experimental and MD simulation approach.

constants. r_0 and θ_0 are equilibrium bond length and angle, respectively. Periodicity and phase angle are represented as n and γ . Note that the summation over dihedral bonds includes both conventional and improper dihedrals. For the non-bonded interactions, the Lennard-Jones (L-J) parameters of ϵ and σ are introduced to describe repulsive and attractive contributions. The final term in Equation (5.1.1) stands for the Columbic pairwise interaction where q are charges of atoms. To assign initial bonded and non-bonded force field parameters from the GAFF, the open source Antechamber (Wang et al., 2006) is utilized. During this step, atomic point charges were calculated via Antechamber using AM1-BCC (Jakalian et al., 2002) method. The water molecules were described using the TIP3P model (Price and Brooks, 2004) with a long-range Columbic solver. To describe the interactions between gold-gold, we applied embedded atom method (EAM) potential (Foiles et al., 1986). For non-bonded interactions between different types of atoms, Lorentz-Berthelot mixing rules are used to calculate ϵ_{ij} and σ_{ij} as Equation (5.1.2) and Equation (5.1.3)

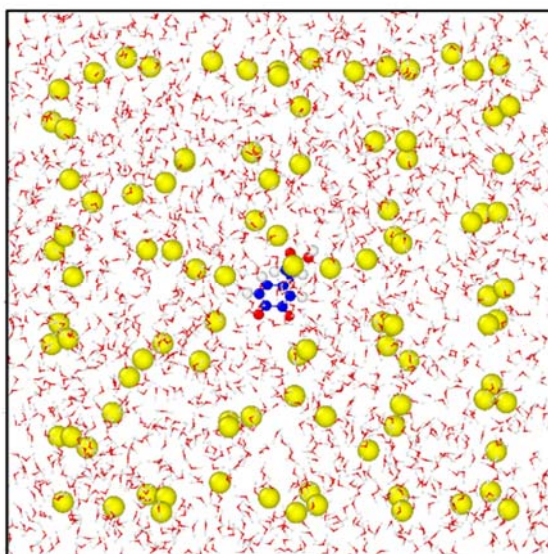
$$\epsilon_{ij} = \sqrt{\epsilon_{ii}\epsilon_{jj}}, \quad (5.1.2)$$

$$\sigma_{ij} = \frac{\sigma_{ii} + \sigma_{jj}}{2}. \quad (5.1.3)$$

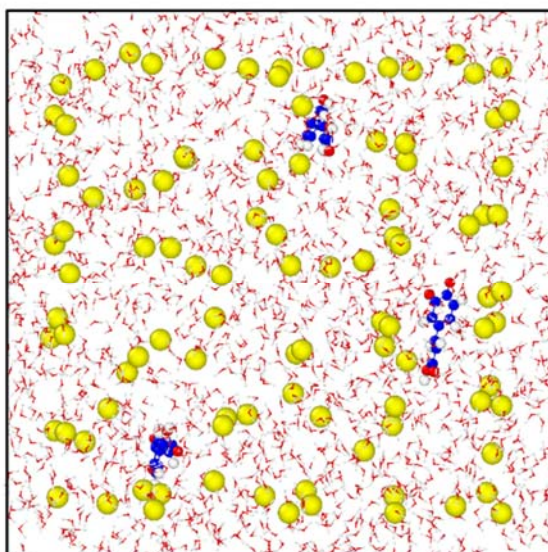
All MD simulations that we consider in this study are performed by utilizing open source LAMMPS (Large-scale Atomic/Molecular Massively Parallel Simulator) code (Plimpton, 1995). To construct an initial low density system, the open source simulation setup tool Packmol (Martinez et al., 2009) is used. The electrostatics were treated using the particle-particle particle-mesh (P³M) technique (Hockney and Eastwood, 1988). The SHAKE constraints scheme (Ryckaert et al., 1977) was applied to water molecules to keep bond length and angle to specified values. By referring a prior MD simulation study on Caffeic acids (Hirano et al., 2013) which constrained all the covalent bonds for hydrogen atoms on it using the linear constraint solver,

the oxidized Caffeic acids are considered as independent rigid body.

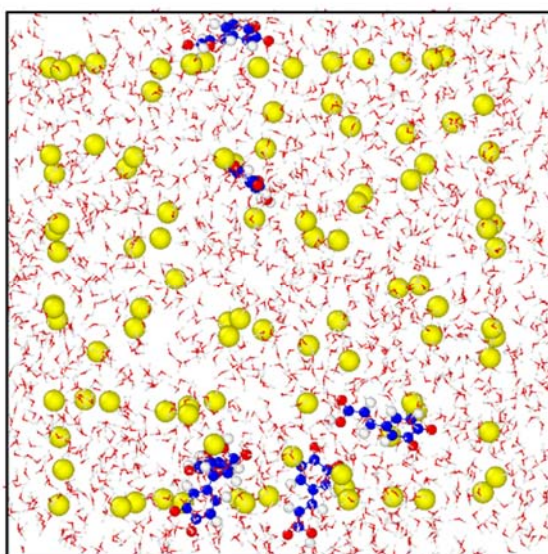
By using Packmol, a given concentration of oxidized Caffeic acids, gold atoms, and water molecules are randomly placed into a cube with size of 60 by 60 by 60 Angstroms. In this study 12 cases are simulated for the green synthesis of AuNPs by varying the number of oxidized Caffeic acids (OXCA) from 1 to 24. For each cases there are 1, 2, 3, 4, 5, 6, 7, 8, 9, 10, 20, and 24 oxidized Caffeic acids with fixed number of 100 gold atoms and 2,000 water molecules. Trough Figure 5.2-(a) to (f), the randomly packed initial configurations of representative cases are shown. The carbon atoms in OXCAs are colored in blue to help the understanding.



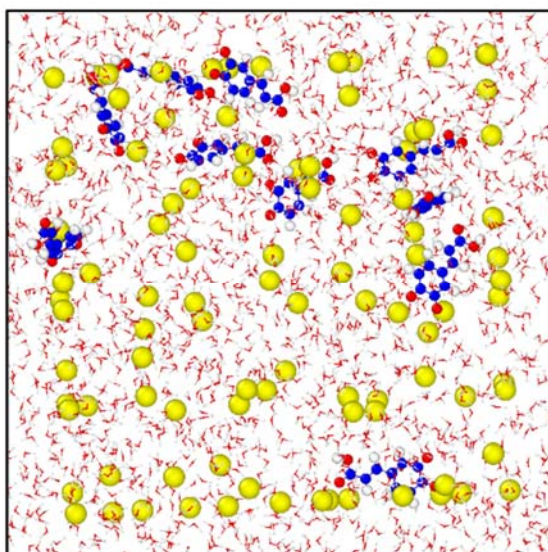
(a) 1 OXCA case



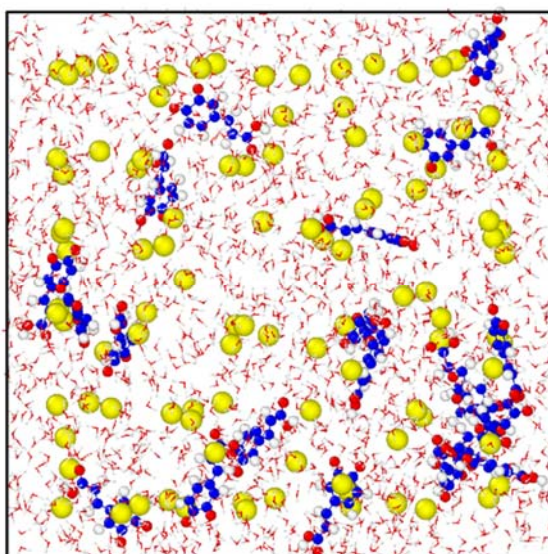
(b) 3 OXCAs case



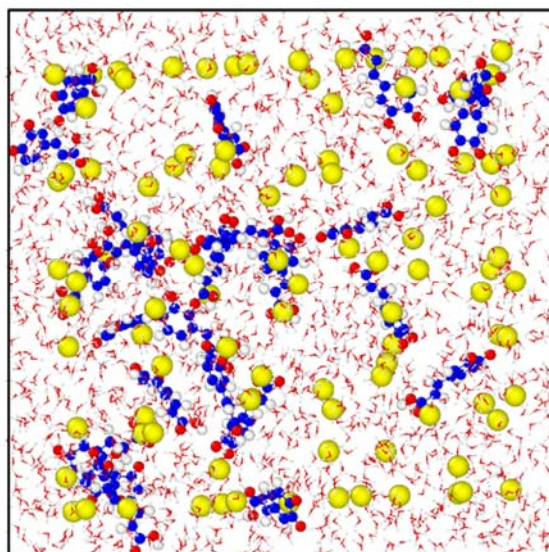
(c) 6 OXCAs case



(d) 10 OXCAs case



(e) 20 OXCAs case



(f) 24 OXCAs case

Figure 5.2 Randomly packed initial configuration of each cases: yellow, red, white, and blue corresponds to gold, oxygen, hydrogen, and carbon atoms, respectively

After randomly packing the molecules, an energy minimization of corresponding system is conducted with steepest descent algorithm. Furthermore, to remove instability of the system, an isothermal-isobaric (NPT) simulation is conducted for 1ps at 358.15K (85 °C) and 1 bar with the timestep of 0.1 fs. Then subsequent NPT simulations (358.15K, 1bar) were started from these initial systems. The terminal NPT simulation time was 0.5 ns with the timestep of 1 fs. For each cases described previously, 5 independent MD simulations are performed with different random initial velocity. The mean diameter of gold clusters is weighted by the number of gold atoms consisting a cluster is measured at the terminal time as shown in Equation (5.1.4). Where d_{i_1} and d_{i_2} are two largest diameters of a cluster i . In this discussion, a cluster consist of even one gold atom is considered

and the atomic radius of gold (Slater, 1964) is utilized for the diameter measurement. The measured weighted mean diameter of gold clusters are averaged over 5 independent MD simulations for each cases.

$$d_{weighted} = \sum_{i=1}^{N_{clusters}} \frac{\left(\frac{d_{i_1} + d_{i_2}}{2} \right) \times N_{number\ of\ gold\ atoms\ consisting\ the\ cluster}}{N_{gold\ atoms\ in\ simulation\ box}}. \quad (5.1.4)$$

From the results obtained in Figure 5.3, we can see that there is a local minimum of average weighted mean diameter when 6 reducing agents are used and similar size of spherical shape Au NPs were well distributed over a wide area of simulation cell. When too much or too less number of reducing agents are used, relatively large gold nanoparticles are aggregated. Representative configurations of each cases at terminal time of the MD simulations are shown in Figure 5.4.

5.1.2 Uncertainty effect to MD simulation of nanoparticle synthesis

To perform molecular dynamic simulations, a specification of initial velocities for all particles in the system is necessary. The velocities of all particles in the system may be set to random values corresponding to a certain initial temperature value. The initial velocities of the system are calculated according to

$$\frac{m_i (\dot{u}_{ix}^2(0) + \dot{u}_{iy}^2(0) + \dot{u}_{iz}^2(0))}{2} = \frac{3}{2} k_B T, \quad (5.1.5)$$

where i is the index of the particle. However, there is no unique set of initial velocity that satisfies the relation in Equation (5.1.5). Therefore, the initial velocities of particles in the system is obtained as

$$\langle \vec{u}_i(0) \rangle = \sqrt{\frac{3k_B T}{2}} \vec{n}, \quad (5.1.6)$$

where \vec{n} is the unit random vector. Due to the randomness of initial velocities of particles consisting the MD system, uncertainty issue arises. In this simulation, to insure the results obtained, we perform 5 independent MD simulations with different random initial velocities of particles for each cases.

In this reason, the performance measure, weighted mean diameter of gold clusters, is averaged over 5 independent MD simulations for each cases. The variance of performance measure due to the uncertainty effect in MD simulation is estimated through standard error analysis as shown in Table 5.1 and Table 5.2. By performing the standard error analysis, we can get the error bar of the performance measures for each cases as shown in Figure 5.3. The computation cost for 1 MD simulation and 5 independent MD simulations for each cases are shown in Table 5.3. The MD simulation is performed with 64bit Intel® Quadcore™ (8thread) i7 CPU 3.70 GHz with 48GB. As we can see, to estimate the effect of uncertainty in the MD simulation and to insure the obtained results, we need tremendous computation time. This is one of the typical obstacles researchers experience when utilizing atomistic level simulation. As a remedy we suggest the develop method, which has high accuracy and efficiency, and demonstrate it through several following numerical examples.

Table 5.1 Average of weighted mean diameters and error analysis

Num of OXCAs	Average of weighted mean diameter (Angstrom)	Standard deviation	Standard error
1	5.40	0.53	0.24
2	5.41	0.36	0.16
3	5.37	0.69	0.31
4	5.65	0.08	0.04
5	5.26	0.36	0.16
6	5.01	0.13	0.06
7	4.95	0.35	0.16
8	5.64	0.36	0.16
9	5.65	0.31	0.14
10	6.09	0.68	0.30
20	6.13	0.80	0.36
24	7.15	0.23	0.10

Table 5.2 Average of weighted mean diameters and error analysis for 5 independent MD simulations for representative cases

MD #	Average of weighted mean diameter (Angstrom)					
	1 OXCA	3 OXCAs	6 OXCAs	10 OXCAs	20 OXCAs	24 OXCAs
1	5.14	5.50	5.11	6.65	7.57	6.73
2	5.77	5.01	5.06	6.29	6.25	7.11
3	4.87	6.66	5.13	4.83	5.38	7.37
4	4.96	4.96	4.94	6.67	6.10	7.34
5	6.25	4.74	4.79	5.99	5.37	7.21
Mean	5.40	5.37	5.01	6.09	6.13	7.15
Standard deviation	0.53	0.69	0.13	0.68	0.80	0.23
Standard error	0.24	0.31	0.06	0.30	0.36	0.10

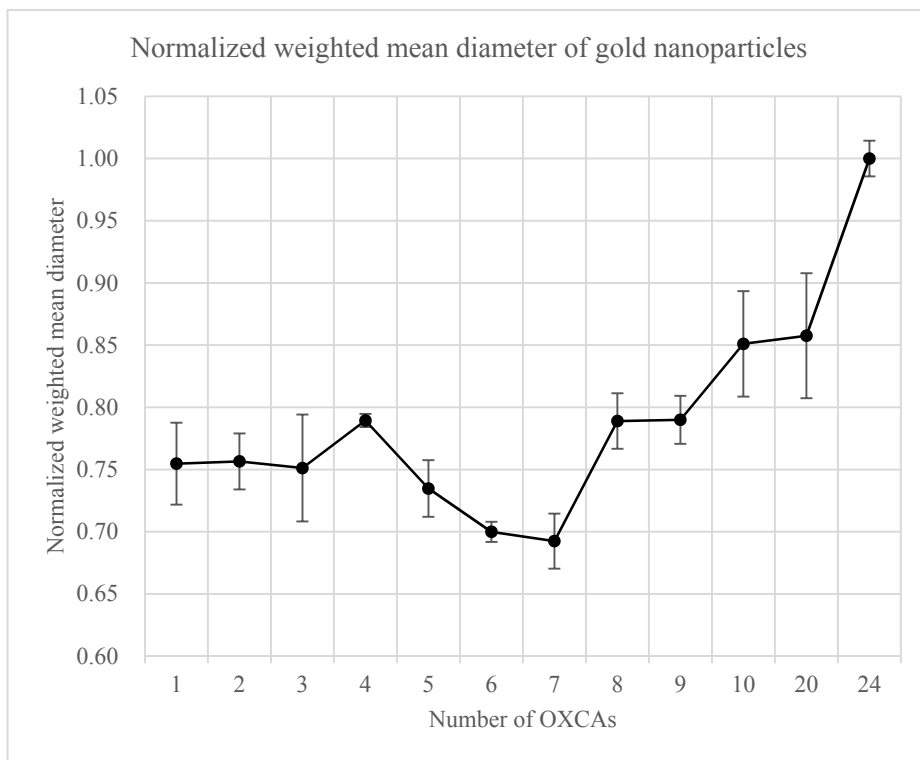
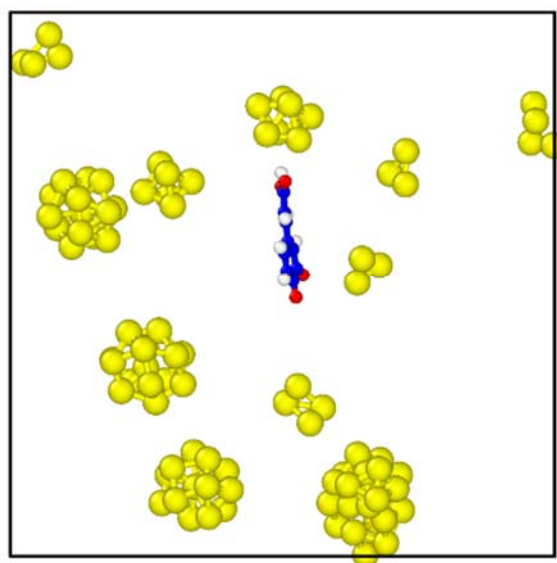


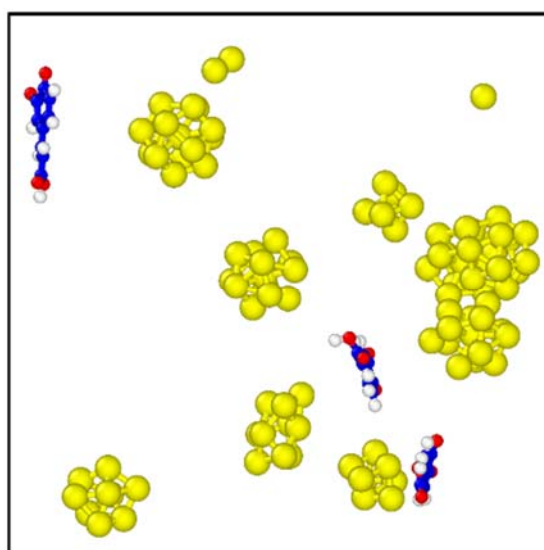
Figure 5.3 Measured average weighted mean diameters of gold nanoparticles with various number of reducing agent at 0.5 ns

Table 5.3 Computation costs

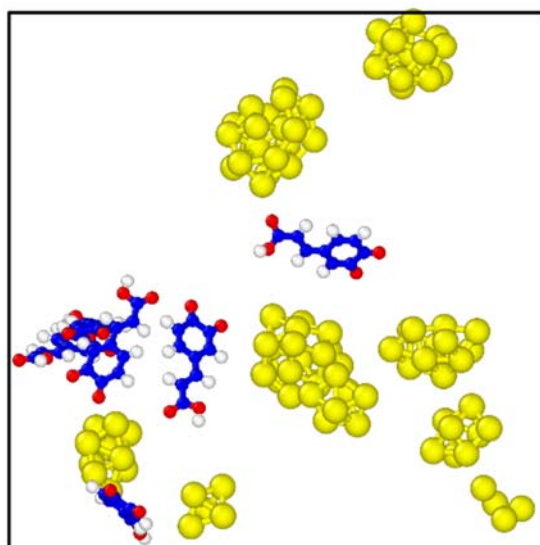
	1 MD simulation	5 MD simulations	Total
Computation cost (hour)	19.95	99.77	1197.23



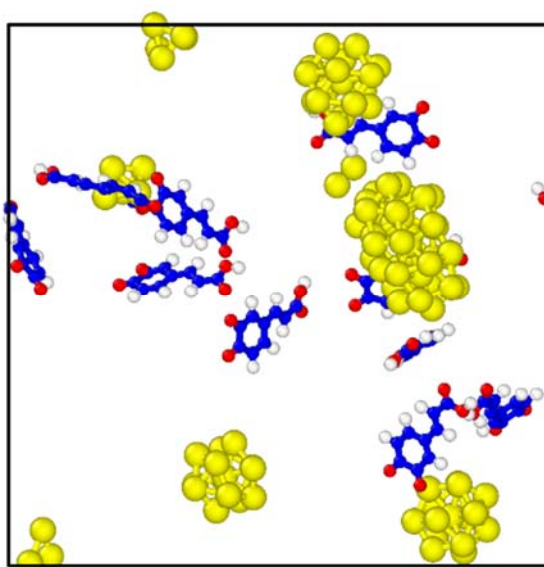
(a) 1 OXCA case



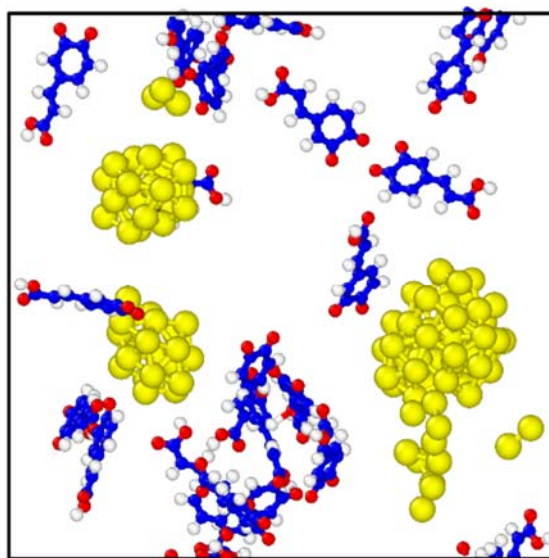
(b) 3 OXCAs case



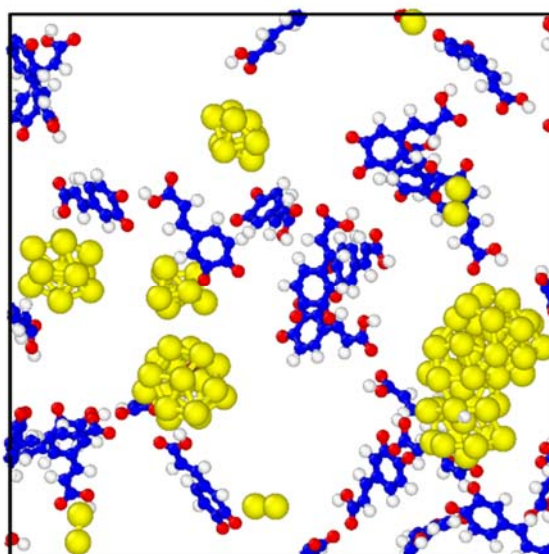
(c) 6 OXCAs case



(d) 10 OXCAs case



(e) 20 OXCAs case



(f) 24 OXCAs case

Figure 5.4 Representative configurations at terminal time of MD simulation

5.1.3 Experiment of nanoparticle synthesis

By utilizing the molecular dynamic (MD) simulation, Caffeic acid is used as green reducing agent to synthesis gold nanoparticles (AuNPs). The redox reaction of Caffeic acid is illustrated in Figure 5.1. Due to the limit of MD simulation, we assume that the Caffeic acid is oxidized into oxidized Caffeic acid and the resulting electrons (e^-) are already used to neutralize gold ions (Au^{3+}) in $HAuCl_4 \cdot 3H_2O$. Therefore in our MD simulations, we will only consider oxidized Caffeic acids and neutralized gold ions to understand the behavior of AuNPs formation

In the experiment of green synthesis of AuNPs, caffeic acid (3,4-dihydroxy cinnamic acid) from plants was used. The objective is to evaluate the green synthesis of AuNPs with various concentrations of caffeic acid. Further, we characterize the prepared AuNPs using high-resolution transmission electron microscopy, and measurements of the mean particle size.

Hydrochloroauric acid trihydrate ($HAuCl_4 \cdot 3H_2O$) and caffeic acid were purchased from Sigma-Aldrich (St. Louis, MO, USA). All other reagents were of analytical grade. Deionized water was used to prepare all of the solutions. A JEM-3010 electron microscope was used to obtain the HR-TEM images at 300 kV (JEOL, Tokyo, Japan). The mean particle size was measured by dynamic light scattering (DLS) on a Brookhaven 90Plus (Brookhaven Instruments Co., Holtsville, NY, USA). The green synthesis of AuNPs with caffeic acid as a reducing agent was performed under a fixed final concentration (0.2 mM) of hydrochloroauric acid trihydrate. While stirring (340 rpm, 220°C) on a hotplate for 2 min, 200 μ L of hydrochloroauric acid trihydrate (1 mM) was added to 800 μ L caffeic acid (variable concentration). The reaction mixture (1 mL) was stirred on a hotplate for an additional 1 min and placed in an oven (85°C) for 12 h. In total, eleven final concentrations of caffeic acid (0.008, 0.04, 0.08, 0.12, 0.16, 0.2, 0.24, 0.28, 0.4, 0.48 and 0.56 mM) were tested for the green synthesis of AuNPs.

The formation of AuNPs is easily detected by a change in the color of

the solution. In our experiments, no visible change in color was detected for caffeic acid solutions at the lowest tested concentrations of 0.008 and 0.04 mM, as shown in Figure 5.5-(a) and (b). However, at higher concentrations, the color of the solution changed to pale gray, violet, wine, purple or gray, as shown in Figure 5.5-(c) through (k).

The mean particle size was measured based on dynamic light scattering, and the results are shown in Table 5.4 and Figure 5.6. Over the range of tested concentrations of caffeic acid (0.008-0.56 mM), the plot of the mean particle size exhibited a parabolic shape, where 0.28 mM caffeic acid resulted in the smallest particle size of 89.4 nm. The mean particle size increased when the concentration of caffeic acid was either higher or lower than 0.28 mM. In particular, the mean particle size was exceptionally high ($\sim 50 \mu\text{m}$) when the concentration of caffeic acid was 0.008 mM. The results presented in Figure 5.6 demonstrate that 0.28 mM was the optimum concentration of caffeic acid to produce the smallest particle size.

HR-TEM is commonly employed to visualize NPs and to obtain information regarding the size, shape and dispersion state of NPs. The lowest concentration of caffeic acid (0.008 mM) was insufficient to reduce Au^{3+} to AuNPs and instead generated micro-sized particles with a mean particle size of $> 50 \mu\text{m}$, as shown in Figure 5.7-(a). As the concentration of caffeic acid increased from 0.04 mM to 0.24 mM, the mean particle size gradually decreased. Interestingly, the shape of the AuNPs became increasingly spherical as the concentration of caffeic acid increased up to 0.24 mM, as shown from Figure 5.7-(b) to Figure 5.7-(g). The minimum particle size was observed at 0.28 mM, and a sea-urchin-like shape began to appear at this concentration, as shown in Figure 5.7-(h). It is noteworthy that the mean particle size of the sea-urchin-like shape was larger when the caffeic acid concentration increased from 0.28 mM to 0.56 mM, as shown through Figure 5.7-(h) and Figure 5.7-(k). The same finding has been reported by Wang and co-workers when excess ascorbic acid was added to HAuCl_4 as a reducing agent (Wang et al., 2012). The addition of excess ascorbic acid generated sea-urchin-like Au particles with an average diameter of 600-800 nm.

A qualitative comparison of results from aforementioned MD simulations and experiments are shown in Figure 5.8 and Figure 5.9. From the results, we can see that there are local minimums of averaged weighted mean diameters and mean diameters of gold nanoparticles. When too much or too less number of reducing agents are used, relatively large gold nanoparticles are aggregated in both experiment and MD simulations which corroborates each other.

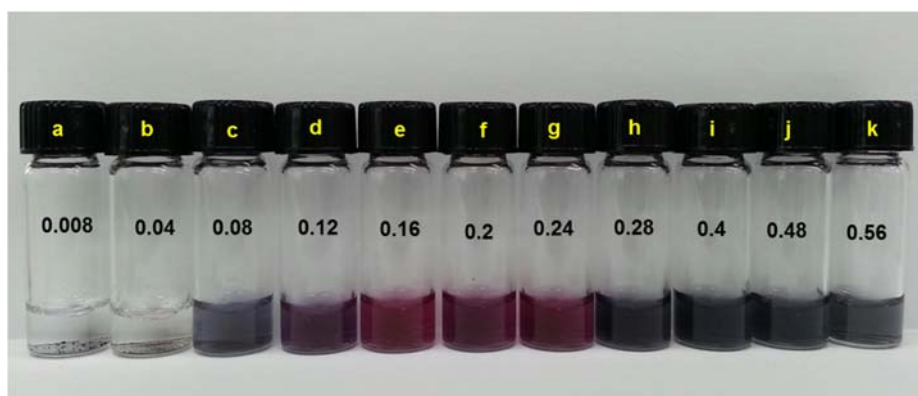


Figure 5.5 Digital images of AuNPs. The final concentration of caffeic acid is (a) 0.008 mM, (b) 0.04 mM, (c) 0.08 mM, (d) 0.12 mM, (e) 0.16 mM, (f) 0.2 mM, (g) 0.24 mM, (h) 0.28 mM, (i) 0.4 mM, (j) 0.48 mM and (k) 0.56 mM. The concentration of Au^{3+} ions is fixed at 0.2 mM. The detailed reaction procedure is described in the experimental section.

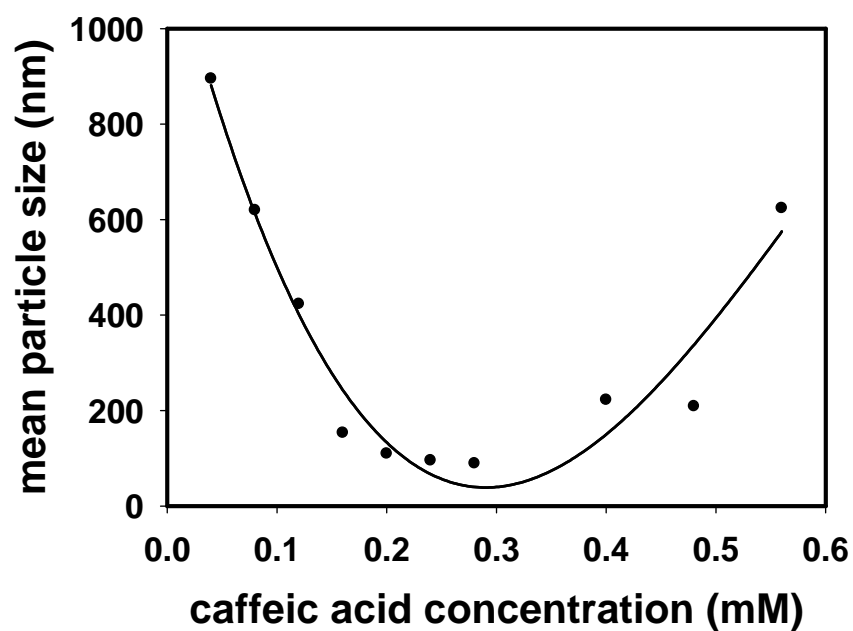
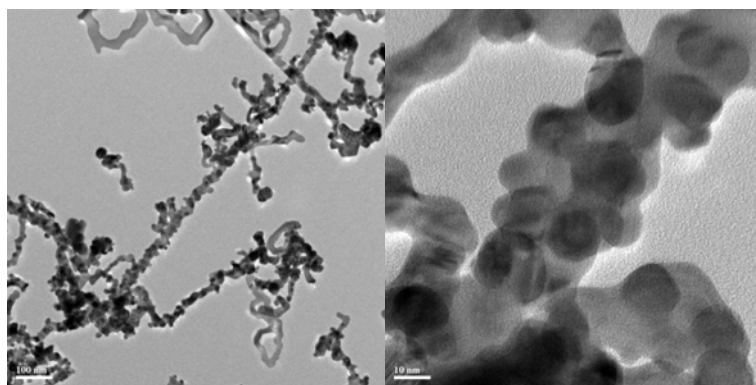


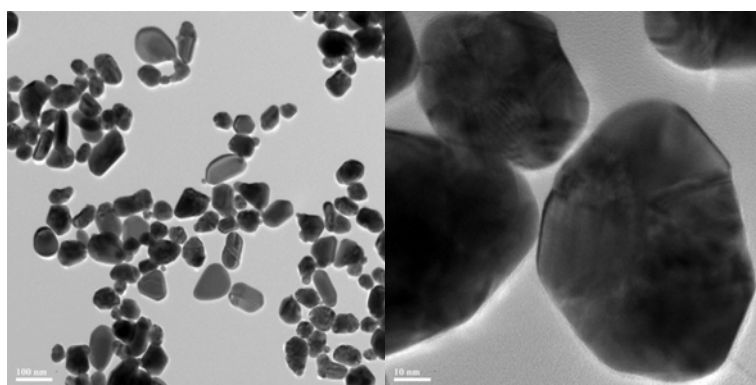
Figure 5.6 Relationship between mean particle size (nm) and caffeic acid concentration (mM)

Table 5.4 Mean particle size (nm) of AuNPs green synthesized using various concentrations of caffeic acid (mM)

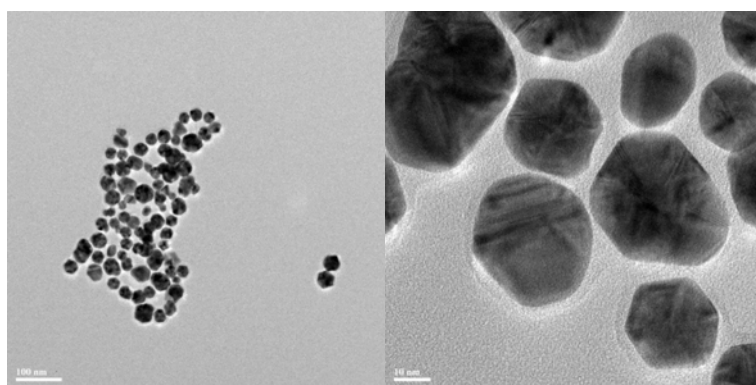
	0.008 mM	0.04 mM	0.08 mM	0.12 mM	0.16 mM	0.2 mM	0.24 mM	0.28 mM	0.4 mM	0.48 mM	0.56 mM
Mean particle size (nm)	50238.4	895.5	619.6	423.1	153.4	109.6	95.4	89.4	222.6	209.1	624.2



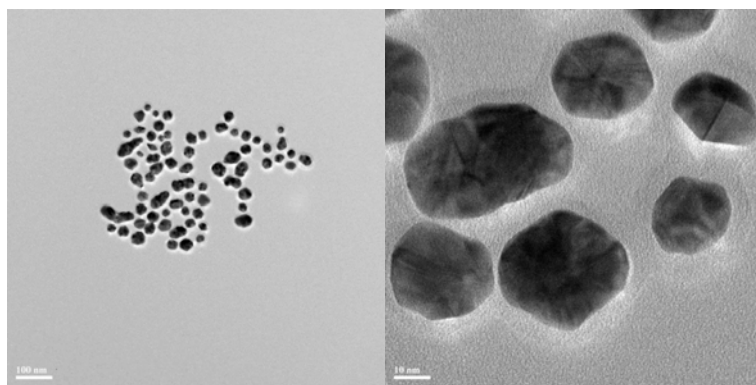
(a) 0.008 mM



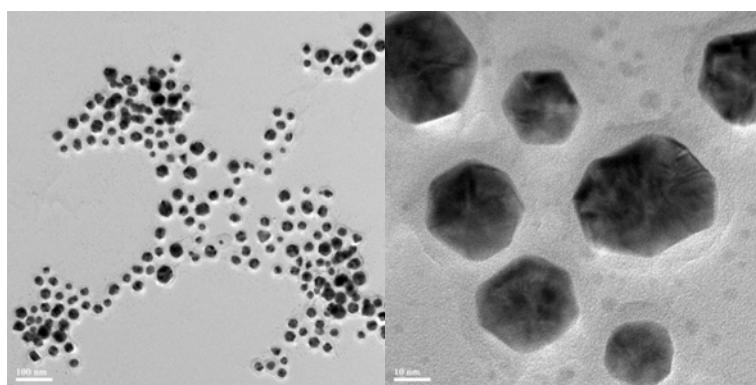
(b) 0.04 mM



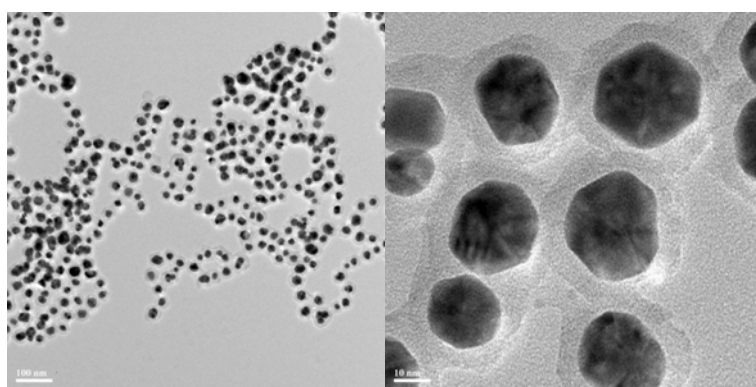
(c) 0.08 mM



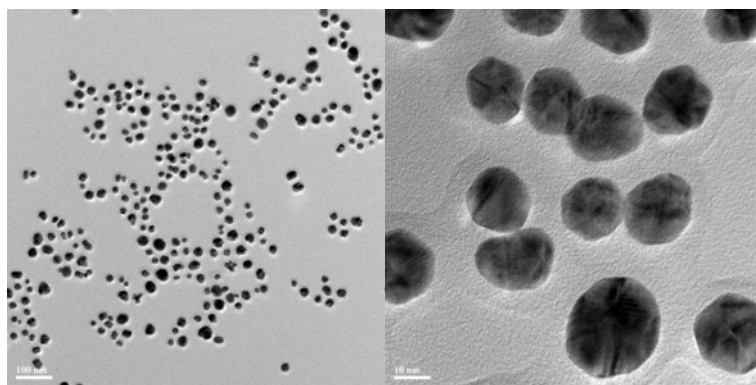
(d) 0.12 mM



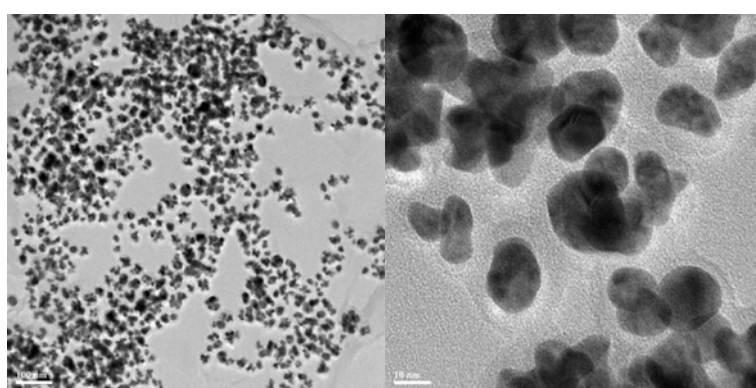
(e) 0.16 mM



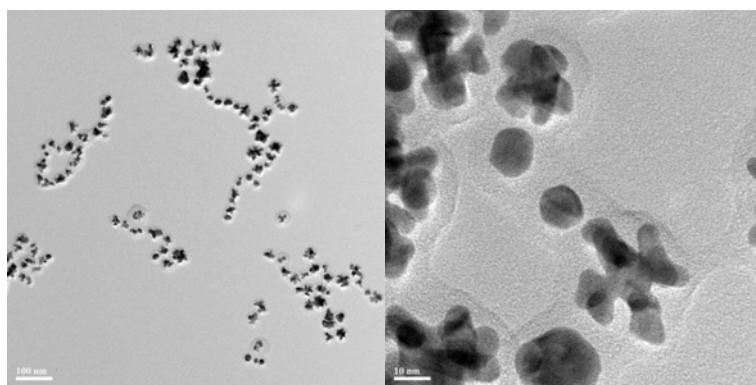
(f) 0.2 mM



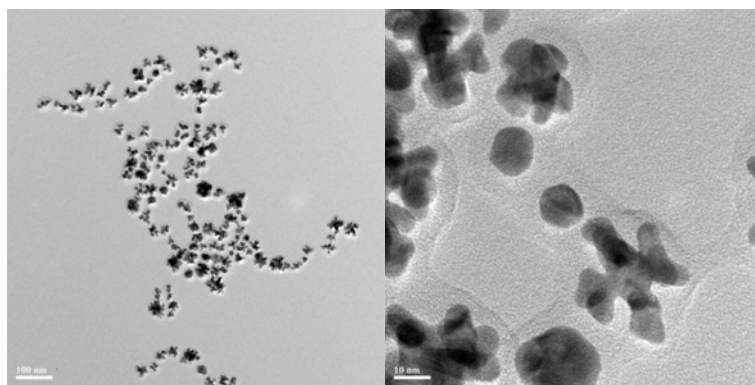
(g) 0.24 mM



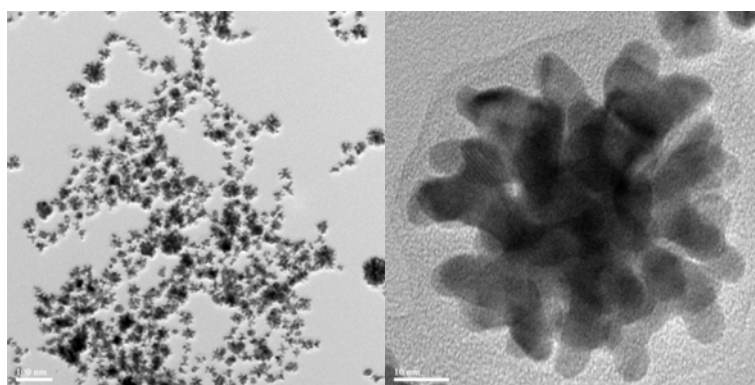
(h) 0.28 mM



(i) 0.4 mM



(j) 0.48 mM



(k) 0.56 mM

Figure 5.7 HR-TEM images of AuNPs. The final concentration of caffeic acid is (a) 0.008 mM, (b) 0.04 mM, (c) 0.08 mM, (d) 0.12 mM, (e) 0.16 mM, (f) 0.2 mM, (g) 0.24 mM, (h) 0.28 mM, (i) 0.4 mM, (j) 0.48 mM and (k) 0.56 mM. The scale bar for each image represents 100 nm (left) and 10 nm (right)

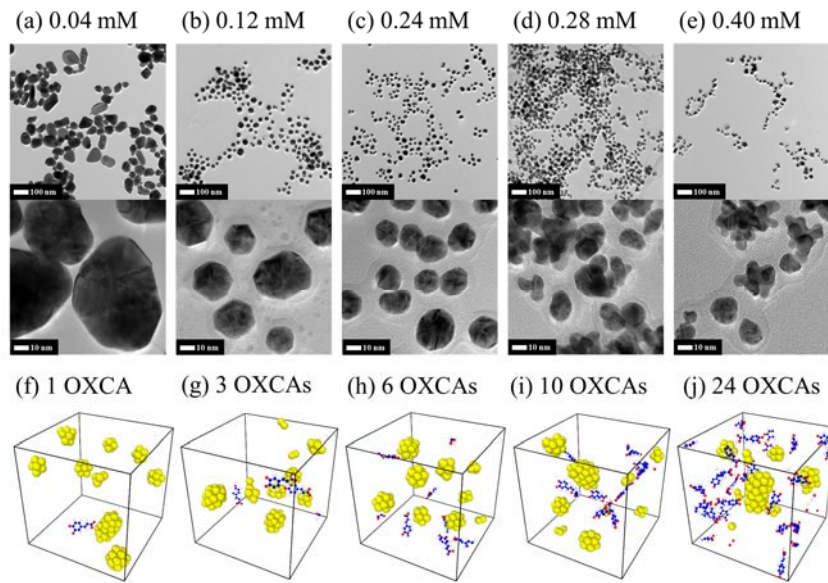
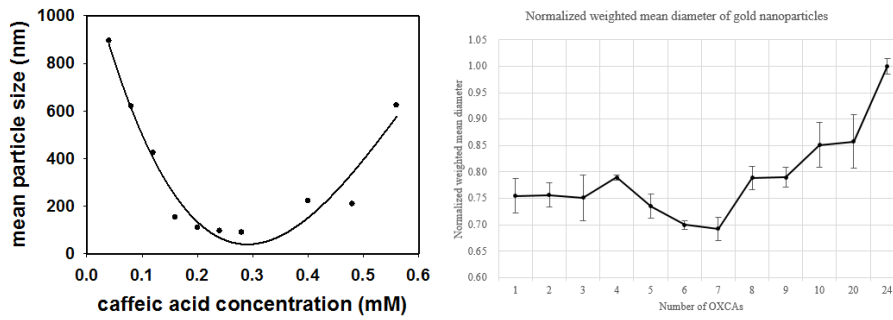


Figure 5.8 HR-TEM and MD simulation images of AuNPs. The final TEM image of caffeic acid is (a) 0.04 mM, (b) 0.12 mM, (c) 0.24 mM, (d) 0.24 mM and (e) 0.28 mM and final MD atomic configuration is (f) 1 OXCA, (g) 3 OXCAs, (h) 6 OXCAs, (i) 10 OXCAs and (j) 24 OXCAs. The scale bar for each image represents 100 nm and 10 nm



(a) experiment results

(b) MD simulation results

Figure 5.9 Qualitative comparison of (a) experiment and (b) MD simulation

5.2 Design optimization: unknown potential parameters

In this example, we perform deterministic design optimization to find unknown potential parameters between the interactions of nanoparticles and substrate. One of the source of uncertainty is potential parameter uncertainty which arises when some parameters defining the interatomic interactions in the MD simulations are not precisely known or due to the empirical nature of fitting the force field parameters to experimental observations. In this purpose, we find the optimal potential parameters between NPs and substrate by deterministic design optimization based on the sensitivity.

Gold and silver nanoparticles have brought interest in nanomedicine due to their versatile applications including drug delivery, medical diagnostics, biosensors, and cancer therapeutics (Dreaden et al., 2011, Sekhon and Kamboj, 2010). When the metallic nanoparticles were exposed to biological systems, many biological entities interact with the surface of nanoparticles through physical adsorptions. Therefore, the geometrical properties of metallic nanoparticles influence the binding and structure of biological entities which are closely related to their biological activities. The size and morphology of metallic nanoparticles are known to have significant effects on the structure and stability of the adsorbed proteins (Chakraborty et al., 2011, Gagner et al., 2011, Kaur and Forrest, 2012, Park et al., 2011a, Pal et al., 2007). Chakraborty et al. reported that gold nanorods induce protein unfolding at their surface compared with gold nanospheres that used bovine serum albumin as a model compound (Chakraborty et al., 2011). Both nanoparticle morphology and protein properties determine the final form of nanobioconjugates (Gagner et al., 2011). Hence the elucidation of nanoparticle morphology is critical in developing new nanobioconjugates for future biomedical, pharmaceutical, and therapeutic applications. In this paper, gold and silver nanoparticles are utilized to develop an image analysis method.

5.2.1 Optimization of nanoparticle-substrate force field parameters

To precisely mimic the nanoscale behavior observed from experiments with molecular dynamics, accurate modeling and interatomic potential parameters are essential. Especially, when substrates are involved, to consider the bulk characteristics of substrates, a sufficient number of layers are necessary even when we froze certain layers. In spite of efforts to reduce the size of substrate, usually the structure of substrate requires special treatments in interatomic force terms such as bonding, angle, dihedral, and improper ones. These kinds of special treatments generally leads to the tremendous increase of computation cost in MD simulation compared to the portion of simple metallic nanoparticles. Furthermore, only limited sort of substrates structures and force field parameters are reported due to the empirical nature of fitting reasonable parameters matching the bulk properties of targeted material. It is well known that these drawbacks makes it hard to fulfill the needs of those whom are interested in the field of correlating the molecular dynamics simulation to experiments, which are rapidly increasing since conventional continuum based approach cannot precisely represent the nanoscale behavior and the scale problem in ab initio based simulation approaches.

In this example, we will focus on the reduction of the computation cost due to the complicated structures of substrates by replacing it with a potential wall model based on Lennard-Jones potential with proper interatomic force field parameters which suitably mimics the behavior of the substrate found from optimization problem based on the developed adjoint design sensitivity. This approach is thought quite reasonable since when the substrates and the nanoparticles are consist of different materials, the interactions between the substrates and the nanoparticles are represented only by Lennard-Jones potential type interactions no matter what kind or type of interatomic potential and force field is utilized for each other. Let's consider a gold nanoparticle placed on a mica substrate as Figure 5.10-(a). The objective is to find proper Lennard-Jones force field parameters ϵ and σ , which are energy depth and collision diameter, of potential wall substrate as shown in Figure 5.10-(b). A design optimization problem is formulated as

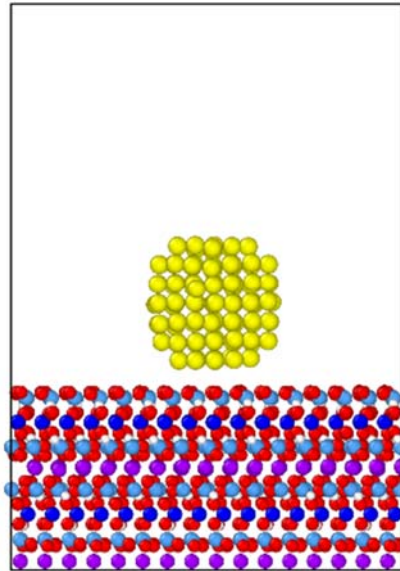
$$\text{Minimize} \quad \psi = \frac{1}{t_2 - t_1} \int_{t_1}^{t_2} \left\{ \Phi_{pot. wall}^m(t) - \Phi_{mica}^m(t) \right\}^2 dt, \quad (5.2.1)$$

$$\begin{aligned} \text{Subjected to} \quad & 0.0001 \leq \varepsilon \leq 100, \\ & 0.1 \leq \sigma \leq 100, \end{aligned} \quad (5.2.2)$$

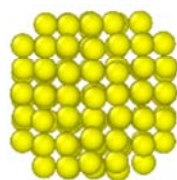
The objective function is the square difference of time averaged potential energy of gold nanoparticle from t_1 to t_2 , which are 9,000 and 10,000 steps, between mica substrate model and potential wall substrate model. It is unconstrained optimization problem with only side constraints to design variables ε and σ as shown in Equation (5.2.2). The initial value of design variables are $\varepsilon = 2.0$ (eV) and $\sigma = 5.0$ (Å). A gradient-based optimization algorithm for unconstrained optimization problem, Brydon-Fletcher-Goldfarb-Shanno (BFGS) is utilized to solve the above mentioned optimization problem where the required gradient values by the optimizer are provided from our developed adjoint design sensitivity analysis method (Users Manual, 1995).

The initial design of a gold nanoparticle and a mica substrate is obtained by utilizing open source molecular dynamics simulation package LAMMPS due to the complexity in the structure and force field type of mica substrate. The gold nanoparticle is thermally equilibrated independently at 300K for 1 ns with timestep size of 1 fs using Nose-Hoover thermostat. We utilized EAM (Embedded Atom Method) interatomic potential for gold atoms (Foiles et al., 1986). After thermal equilibration of a gold nanoparticle, it is carefully placed above the mica substrate which is consist of 5 atom types with total 2,688 atoms, 3 harmonic bond types with total 3,840 bonds, and 6 harmonic angle types with total 9,984 angles. Then an additional thermal equilibration is performed for 10 ps at 300K with timestep size of 1 fs using Nose-Hoover thermostat. Finally, geometry and velocity information of the gold nanoparticle is copied from the mica substrate model and placed on the potential wall substrate model to have the same initial condition and distance between the gold nanoparticle and the substrates. The detailed information of

pairwise, bond, and angle force field parameters are shown through Table 5.5 to Table 5.7. The pairwise terms for different atom types are obtained from Lorentz-Berthelot mixing rule. The Lennard-Jones parameters for gold is referred from Merabia et al. (2009).



(a) mica substrate



Potential wall

(b) 12-6 Lennard-Jones type potential wall

Figure 5.10 Two models of a gold nanoparticle on a substrate

Table 5.5 Pairwise force field parameters

Atom type	Epsilon (eV)	Sigma (Angstrom)
Al	0.00216820	3.74178000
H	0.00056370	0.97830000
K	0.00867290	3.38542000
O	0.00108410	3.11815000
Si	0.00216820	3.56359000

Table 5.6 Harmonic bond force field parameters

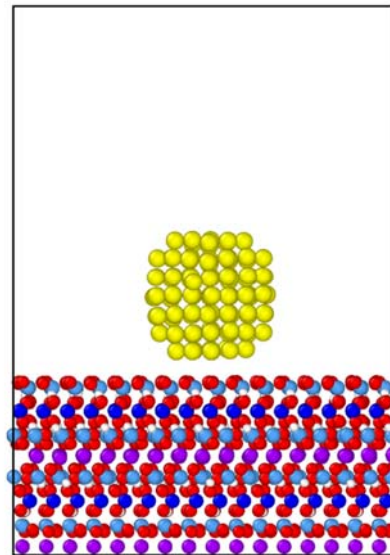
Bond type	K (eV/Å ²)	Equilibrium bond distance (Å)
Al - O	37.2935	1.9400
H - O	42.9309	0.9290
Si - O	37.2935	1.6400

Table 5.7 Harmonic angle force field parameters

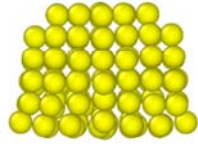
Angle type	K (eV/radian ²)	Equilibrium angle (degrees)
Al-O-Al	14.7440	109.5000
Al-O-H	0.9974	116.2000
Al-O-Si	14.7440	109.5000
O-Al-O	14.7440	95.0000
O-Si-O	14.7440	109.5000
Si-O-Si	14.7440	109.5000

The obtained optimal design, optimization results and optimization history are shown in Figure 5.11 to Figure 5.14 and Table 5.8 to Table 5.12. In Figure 5.11, the shapes of gold nanoparticle at terminal time (10,000 steps) for mica substrate model, initial design of potential wall model and optimal design of potential wall model. As we can see, an arbitrary choice of force field parameters may lead to awkward results. In Table 5.8, the time averaged potential energy of gold nanoparticle between 9,000 steps and 10,000 steps is compared for initial and optimal potential wall substrate model and mica substrate model. As a result of optimization, the agreement between the potential wall substrate model and the mica substrate model is considerably improved from 96.4% to 99.9%. To ensure the reliability of our in-house molecular dynamics simulation code, we compared the time averaged gold nanoparticle potential energy with LAMMPS as shown in Table 5.9. As we can see, the agreement between the in-house MD simulation code and LAMMPS is excellent for both initial and optimal design of potential wall substrate model. Furthermore, the optimal force field parameters ϵ and σ are shown in Table 5.10. The optimal value of ϵ is reduced to 0.01% and σ is reduced to 80% of initial arbitrary value. The optimization history and the objective function value as a result of optimization are shown in Figure 5.12 and Table 5.11. A sudden and monotonic drop of the objective function value as shown in Figure 5.12 indicates the developed adjoint design sensitivity is very accurate. The total function calls and gradient calls are 65 and 8 times, respectively. As a result of optimization based on the developed

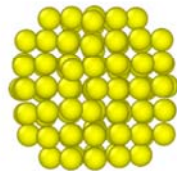
adjoint design sensitivity analysis method, the objective function, which is the square difference of time averaged gold nanoparticle potential energy in mica and potential wall substrate model, has been reduced about 99.9995%. Furthermore, the time history of the gold nanoparticle potential energy from the initial to the terminal time is shown in Figure 5.13. Even though we have targeted the matching time between 9,000 and 10,000 steps, the optimal design of potential wall substrate model agrees well with the mica substrate model. This is since the model of optimization model is well thermally equilibrated a prior to the optimization process.



(a) Gold nanoparticle on mica model



(b) Initial design of potential wall model



(c) Optimal design of potential wall model

Figure 5.11 Gold nanoparticle after 10,000 steps of MD simulation

Table 5.8 Comparison of initial and optimal design with mica model

Substrate type	Time averaged potential energy (eV)	Agreement with mica model (%)
Mica model	-408.0900	100.0000
Potential wall (initial)	-393.4290	96.4074
Potential wall (optimal)	-407.7514	99.9170

Table 5.9 Comparison of optimization results with LAMMPS

Substrate type	(a) In-house code	(b) LAMMPS	(a)/(b) (%)
Potential wall (initial)	-393.4290	-392.9745	100.1157
Potential wall (optimal)	-407.7514	-407.7514	100.0000

Table 5.10 Comparison of initial and optimal force field parameters

Design variable	(a) Potential Wall (initial)	(b) Potential Wall (optimal)	(b)/(a) (%)
epsilon	2.0000	0.000305	0.01527
sigma	5.0000	4.041460	80.8292

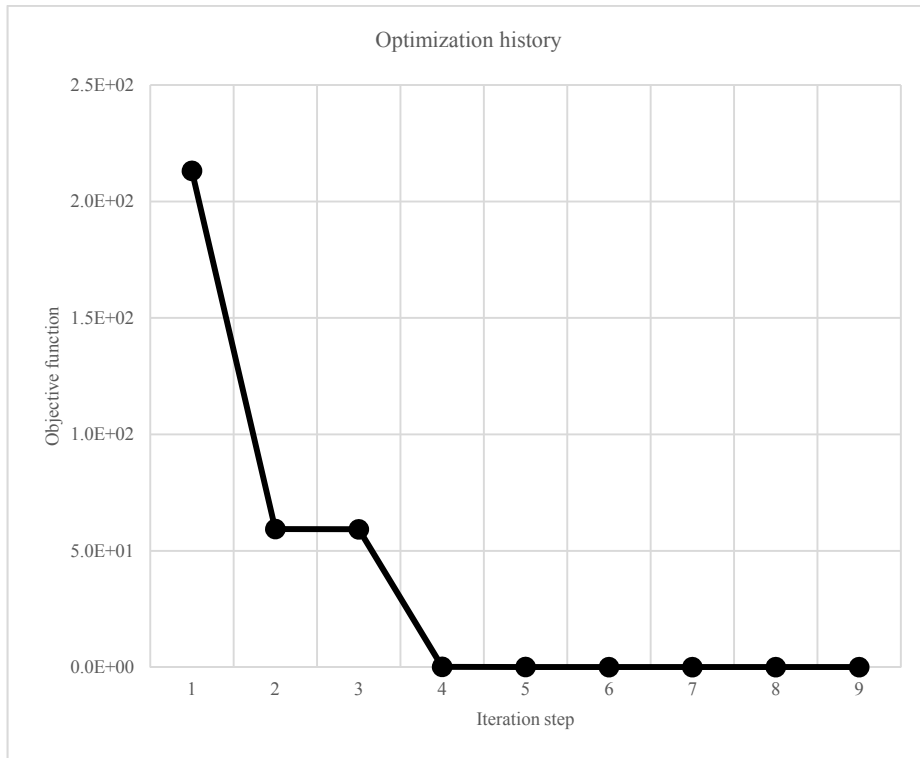


Figure 5.12 Optimization history of objective function

Table 5.11 Optimization results

	(a) Initial	(b) Optimal	(b)/(a) (%)
Objective function	2.1315E+02	1.0657E-01	0.0005

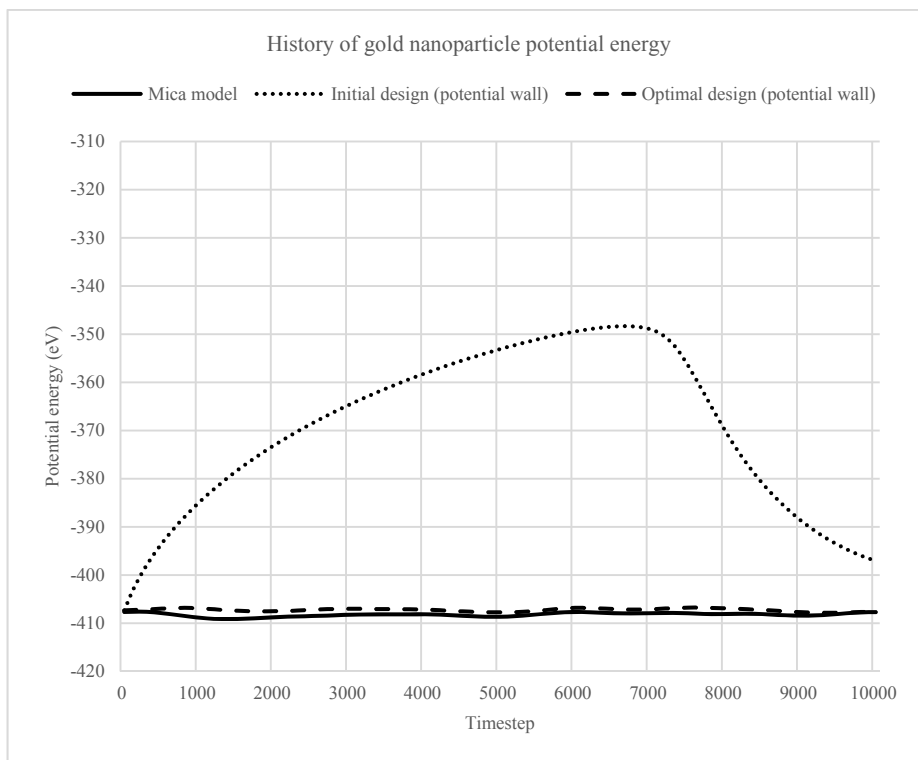


Figure 5.13 Time history of gold nanoparticle potential energy of initial and optimal design of potential wall and mica substrate model

Table 5.12 Radius of gyration comparison

Substrate type	Time averaged radius of gyration (Å)	Agreement with mica model (%)
Mica model	5.8399	100.00
Potential wall (initial)	5.8232	99.71
Potential wall (optimal)	5.8431	100.05

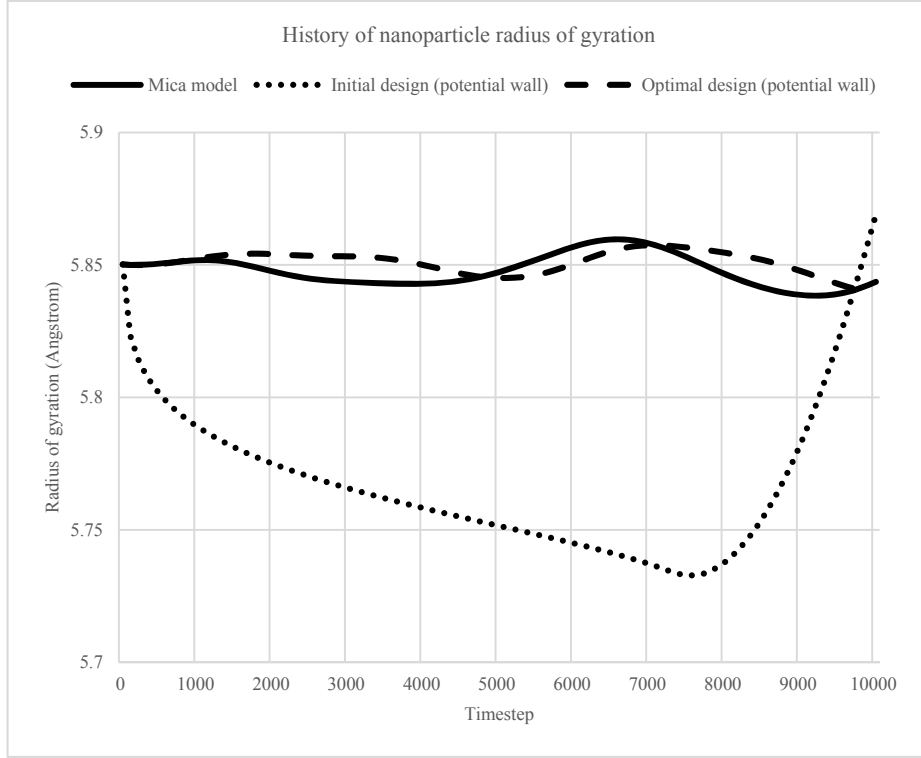


Figure 5.14 Time history of radius of gyration of initial and optimal design of potential wall and mica substrate model

One may be curious that what if we don't know the atomic structure or the force field of target substrate at all. To satisfy one's curiosity, we have change the objective function as

$$\text{Minimize} \quad \psi = \frac{1}{t_2 - t_1} \int_{t_1}^{t_2} \Phi_{pot. wall}^m(t) dt, \quad (5.2.3)$$

$$\text{Subjected to} \quad \begin{aligned} 0.0001 &\leq \varepsilon \leq 100, \\ 0.1 &\leq \sigma \leq 100, \end{aligned} \quad (5.2.4)$$

which means that by solving the above optimization problem, the time

averaged gold nanoparticle potential energy is minimized for targeted time interval. The side constraints of the design variables and all other conditions are exactly the same with the previous optimization problem. The optimization results are shown in Table 5.13 and Figure 5.15. To ease the understanding, the optimization problem that minimizes square difference of time averaged gold nanoparticle potential energy in mica and potential wall substrate model is labeled as ‘optimal design 1’ and the problem that we have assumed not knowing any atomic structure and force field information which minimizes the time averaged gold nanoparticle potential energy in potential wall substrate model is labeled as ‘optimal design 2’. As shown in Table 5.13, the optimization results are remarkably similar. Furthermore the time history of the gold nanoparticle potential energy for optimal designs also agrees well, as shown in Figure 5.15.

Finally, we will compare the computational cost of mica substrate, potential wall substrate, and optimization. The specification of computing hardware is 64bit Intel® Quadcore™ (8thread) i7 CPU 3.70 GHz with 48GB memory. However, to eliminate the effect of parallel algorithm scheme, no parallel computing methods are utilized since optimization is performed with the developed in-house MD simulation code and the analysis of mica substrate and potential wall substrate models are computed with LAMMPS. The normalized computational costs are shown in Table 5.14. As we can see, with only 34% computational cost of complex mica substrate model for finding the optimal force field parameters can reduce the computational cost 99.9925% in MD simulation of gold nanoparticle substrate. Furthermore, as shown above, by solving a simple optimization problem based on the developed adjoint design sensitivity we can not only reduce the computational cost tremendously but also assure the MD simulation accuracy over 99.9%.

Table 5.13 Comparison of optimal designs with mica substrate model

	Time averaged potential energy (eV)	Agreement with mica model
Mica	-408.0900	100.0000
Optimal design 1 (potential wall)	-407.7514	99.9170
Optimal design 2 (potential wall)	-407.7575	99.9185

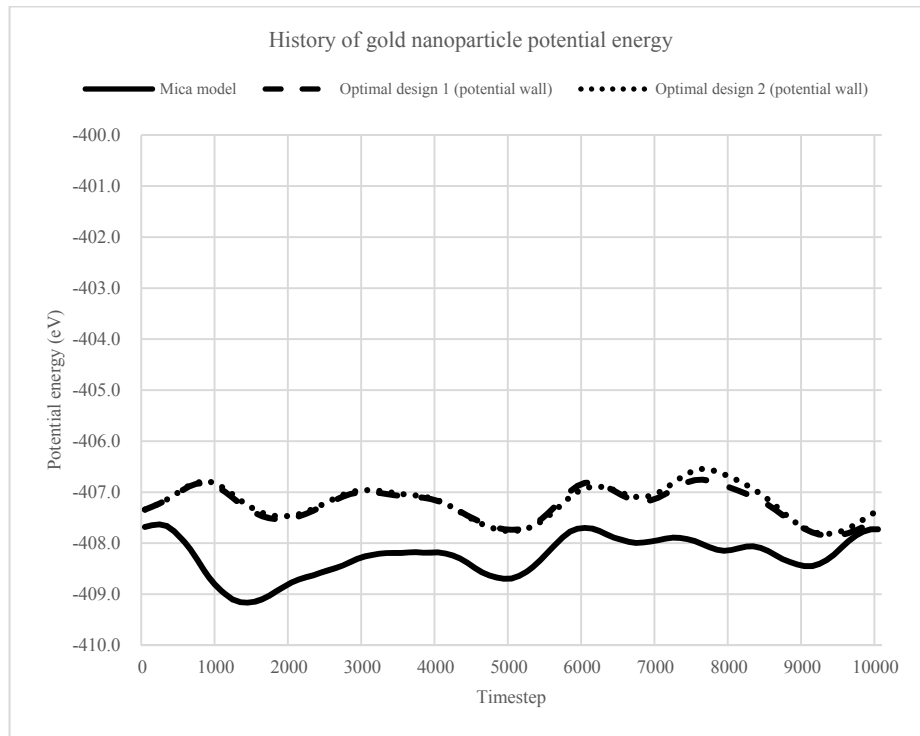


Figure 5.15 Time history of gold nanoparticle potential energy of optimal designs and mica substrate model

Table 5.14 Computational cost comparison

	(a) Mica substrate	(b) Potential wall	(c) Optimization
Normalized computational cost	1.0000	0.0075	0.3413

For a larger size nanoparticle problem, we enlarged the number of gold atoms consisting the nanoparticle to 959 from 116. Furthermore, the objective function is the square difference of time averaged potential energy of gold nanoparticle from t_1 to t_2 , which are 6,000 and 7,000 steps, between mica substrate model and potential wall substrate model.

$$\text{Minimize } \psi = \frac{1}{t_2 - t_1} \int_{t_1}^{t_2} \left\{ \Phi_{pot. wall}^m(t) - \Phi_{mica}^m(t) \right\}^2 dt, \quad (5.2.5)$$

$$\begin{aligned} \text{Subjected to } \quad & 0.0001 \leq \varepsilon \leq 100, \\ & 0.1 \leq \sigma \leq 100, \end{aligned} \quad (5.2.6)$$

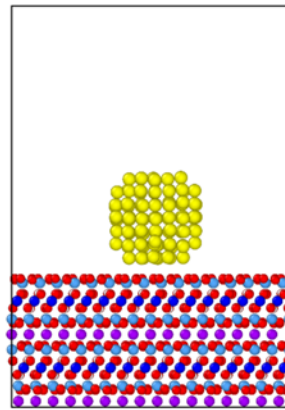
It is unconstrained optimization problem with only side constraints to design variables ε and σ as shown in Equation (5.2.2). The initial value of design variables are $\varepsilon = 2.0$ (eV) and $\sigma = 8.0$ (Å). A gradient-based optimization algorithm for unconstrained optimization problem, Brydon-Fletcher-Goldfarb-Shanno (BFGS) is utilized to solve the above mentioned optimization problem where the required gradient values by the optimizer are provided from our developed adjoint design sensitivity analysis method.

The initial design of a gold nanoparticle and a mica substrate is obtained by utilizing open source molecular dynamics simulation package LAMMPS due to the complexity in the structure and force field type of mica substrate. The gold nanoparticle is thermally equilibrated independently at 300K for 1 ns with timestep size of 1 fs using Nose-Hoover thermostat. We utilized EAM (Embedded Atom Method) interatomic potential for gold atoms (Foiles et al., 1986). After thermal equilibration of a gold nanoparticle, it is carefully placed above the mica substrate which is consist of 5 atom types with total 24,192 atoms, 3 harmonic bond types with total 34,560 bonds, and 6 harmonic angle types with total 89,856 angles. Then an additional thermal equilibration is performed for 10 ps at 300K with timestep size of 1 fs using Nose-Hoover thermostat. Finally, geometry and velocity information of the gold nanoparticle is copied from the mica substrate model and placed on the

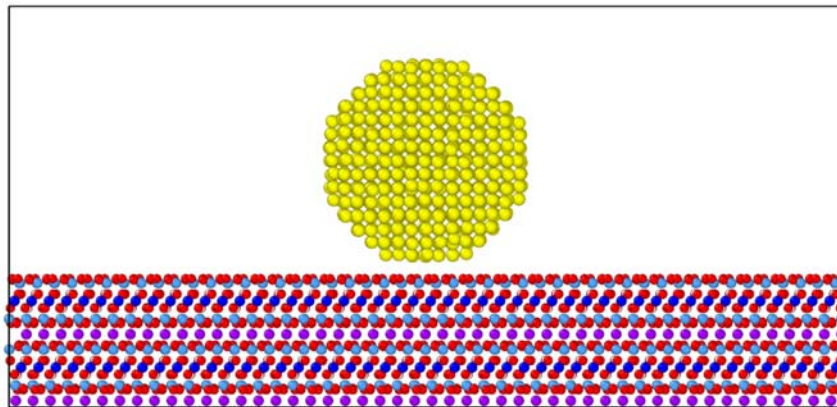
potential wall substrate model to have the same initial condition and distance between the gold nanoparticle and the substrates. The detailed information of pairwise, bond, and angle force field parameters are shown through Table 5.5 to Table 5.7. The pairwise terms for different atom types are obtained from Lorentz-Berthelot mixing rule. The Lennard-Jones parameters for gold is referred from Merabia et al. (2009).

The initial design, optimization results, optimization history and computation costs are shown in Figure 5.16 to Figure 5.19 and Table 5.15 to Table 5.17. In Figure 5.16, the shapes of gold nanoparticle at initial for 116 and 959 atoms on mica substrate model are shown. In Table 5.15, the time averaged potential energy of gold nanoparticle between 6,000 steps and 7,000 steps is compared for initial and optimal potential wall substrate model and mica substrate model. As a result of optimization, the agreement between the potential wall substrate model and the mica substrate model is considerably improved from 80.8% to 99.9%. The optimization history is shown in Figure 5.17. A sudden and monotonic drop of the objective function value as shown in Figure 5.17 indicates the developed adjoint design sensitivity is very accurate. The total function calls and gradient calls are 32 and 5 times, respectively. Furthermore, the time history of the gold nanoparticle potential energy from the initial to the terminal time is shown in Figure 5.18.

Finally, we will compare the computational cost of mica substrate, potential wall substrate, and optimization. The specification of computing hardware is 64bit Intel® Quadcore™ (8thread) i7 CPU 3.70 GHz with 48GB memory. However, to eliminate the effect of parallel algorithm scheme, no parallel computing methods are utilized since optimization is performed with the developed in-house MD simulation code and the analysis of mica substrate and potential wall substrate models are computed with LAMMPS. The normalized computational costs are shown in Table 5.17. As we can see, with only 64% computational cost of complex mica substrate model for finding the optimal force field parameters can reduce the computational cost 99.9939% in MD simulation of gold nanoparticle substrate.



(a) 116 gold atoms mica substrate model



(b) 959 gold atoms mica substrate model

Figure 5.16 Comparison of 116 and 959 gold atoms mica substrate model

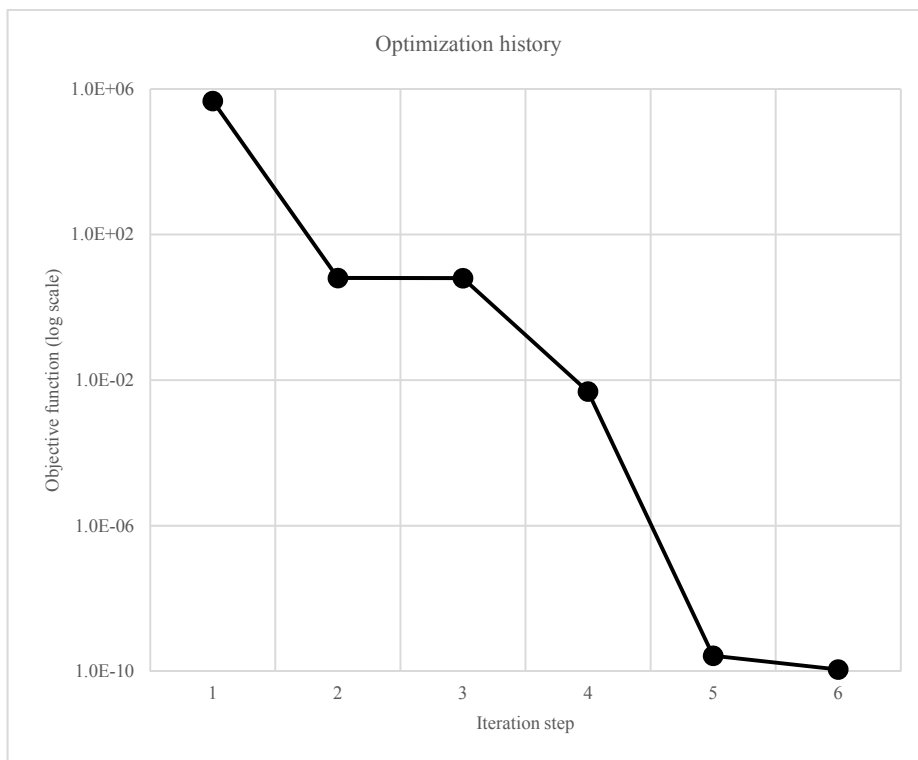


Figure 5.17 Optimization history of objective function

Table 5.15 Comparison of optimization results

Substrate type	Time averaged potential energy (eV)	Agreement with mica model (%)
Mica model	-3547.67	100.0000
Potential wall (initial)	-2866.23	80.7919
Potential wall (optimal)	-3547.60	99.9978

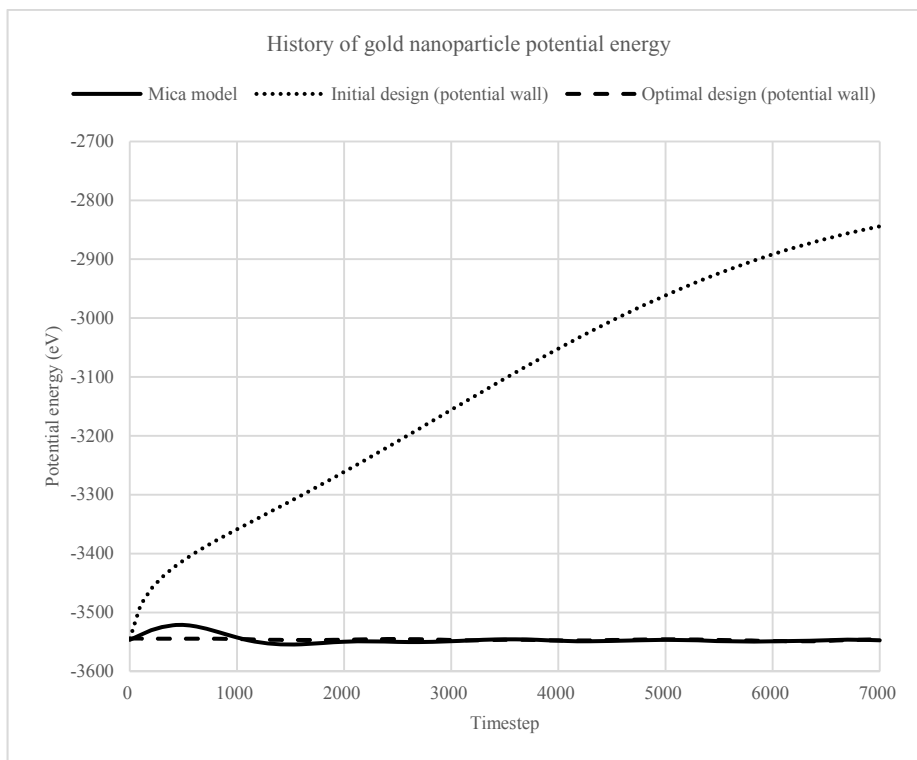


Figure 5.18 Time history of gold nanoparticle potential energy of initial and optimal design of potential wall and mica substrate model

Table 5.16 Radius of gyration comparison

Substrate type	Time averaged radius of gyration (Å)	Agreement with mica model (%)
Mica model	12.0933	100.00
Potential wall (initial)	12.0264	99.44
Potential wall (optimal)	12.1124	100.15

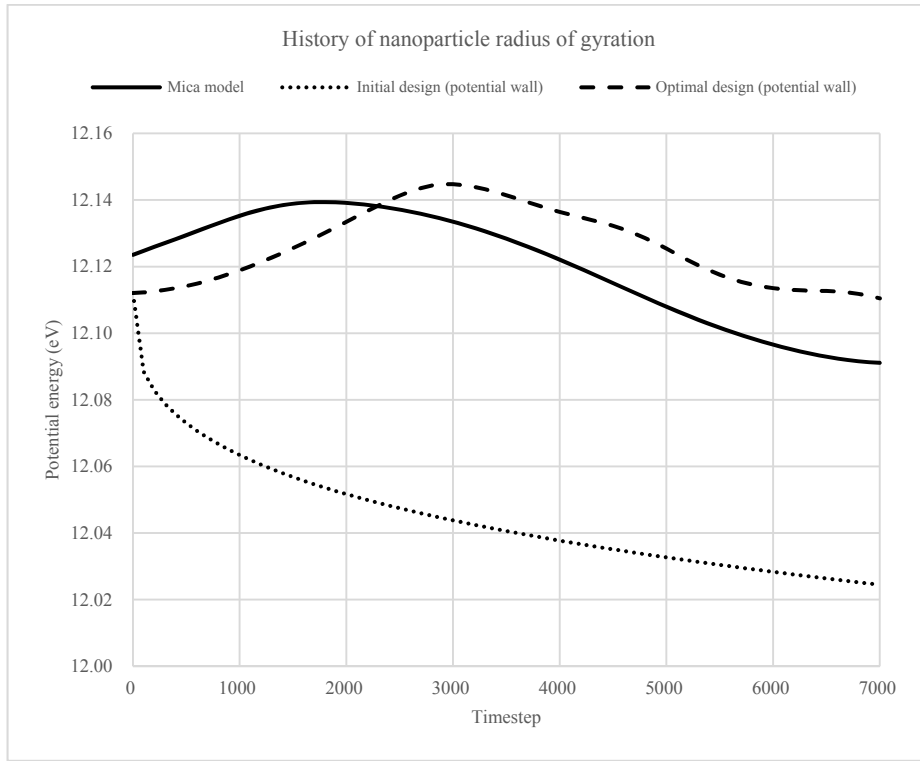


Figure 5.19 Time history of radius of gyration of initial and optimal design of potential wall and mica substrate model

Table 5.17 Computational cost comparison

	(a) Mica substrate	(b) Potential wall	(c) Optimization
Normalized computational cost	1.0000	0.0061	0.6424

5.2.2 Verification of developed design sensitivity

Here, we perform design sensitivity analysis for gold nanoparticle on a substrate problem to verify the accuracy of the developed adjoint design sensitivity and second order analytical sensitivity with respect to random and design variables by comparing it to the finite difference sensitivity. The initial temperature is considered as a random variable and the force field parameters ε and σ between the gold nanoparticle and the 12-6 Lennard-Jones potential wall substrate are considered as design variables. Embedded-Atom-Method (EAM) potential is utilized for gold interatomic potential and ε and σ are 0.5 (eV) and 3.0 (Å), respectively. The mean value of initial temperature is 300K. The performance measure is the time averaged gold nanoparticle potential energy in user defined time interval.

Through Table 5.18 to Table 5.21, the developed adjoint design sensitivity and second order analytical sensitivity is verified by comparing with finite difference sensitivity or direct differential sensitivity. The time interval to average the gold nanoparticle potential energy is between 9,000 – 10,000 steps. In Table 5.18, the accuracy of the developed adjoint design sensitivity with respect to the random initial velocity is shown by comparing it to the direct differential sensitivity and the finite difference sensitivity obtained from finite difference method by varying the perturbation amount from 1.e-2 to 1.e-10. In Table 5.19 and Table 5.20, adjoint design sensitivity with respect to the design variables, which are ε and σ between the gold nanoparticle and the 12-6 Lennard-Jones potential wall substrate, is verified through comparison to direct differential sensitivity and finite difference sensitivity. In most cases, the developed adjoint design sensitivity shows good agreement with both finite difference sensitivity and analytical sensitivity. However, when perturbation amount is 1.00E-7 for the sensitivity of design variable σ , agreement between adjoint sensitivity and finite difference sensitivity decreases to 72%. This is mainly due to numerical noise when finite difference method is utilized since the agreement between two analytical sensitivity, the adjoint sensitivity and the direct differential

sensitivity, is excellent.

Table 5.21 shows the accuracy of the analytical second order design sensitivity with respect to the random and design variable which are the initial velocity of gold nanoparticle and the interatomic force field parameter ε between the gold nanoparticle and the potential wall substrate, respectively. The finite difference sensitivity is obtained by varying the perturbation amount from 1.e-2 to 1.e-12. For the second order sensitivity, the finite difference sensitivity varies from 5 to 89% compared to the analytical sensitivity depending on the perturbation amount used. This indicates that the accuracy of the finite difference sensitivity is not assured since its accuracy depends on the perturbation amount. However, the analytical second order sensitivity gives converged when the perturbation amount is small enough.

Table 5.18 Verification of random initial velocity design sensitivity (9,000-10,000 steps)

Perturbation amount	(a) FDM	(b) DDM	(c) AVM	(c)/(a) (%)	(c)/(b) %
1.00E-02	1.3400E-01	1.4131E-01	1.4149E-01	105.5850	100.1227
1.00E-03	1.4134E-01	1.4131E-01	1.4149E-01	100.1017	100.1227
1.00E-04	1.3903E-01	1.4131E-01	1.4149E-01	101.7706	100.1227
1.00E-05	1.4131E-01	1.4131E-01	1.4149E-01	100.1282	100.1227
1.00E-06	1.4131E-01	1.4131E-01	1.4149E-01	100.1239	100.1227
1.00E-07	1.4131E-01	1.4131E-01	1.4149E-01	100.1261	100.1227
1.00E-08	1.4120E-01	1.4131E-01	1.4149E-01	100.2047	100.1227
1.00E-09	1.4097E-01	1.4131E-01	1.4149E-01	100.3663	100.1227
1.00E-10	1.3983E-01	1.4131E-01	1.4149E-01	101.1823	100.1227

Table 5.19 Verification of design variable ε design sensitivity (9,000-10,000 steps)

Perturbation amount	(a) FDM	(b) DDM	(c) AVM	(c)/(a) (%)	(c)/(b) %
1.00E-02	9.7653E-01	9.7642E-01	9.7661E-01	100.0088	100.0198
1.00E-03	9.7723E-01	9.7642E-01	9.7661E-01	99.9368	100.0198
1.00E-04	9.8371E-01	9.7642E-01	9.7661E-01	99.2787	100.0198
1.00E-05	9.6430E-01	9.7642E-01	9.7661E-01	101.2769	100.0198
1.00E-06	9.7554E-01	9.7642E-01	9.7661E-01	100.1096	100.0198
1.00E-07	9.7641E-01	9.7642E-01	9.7661E-01	100.0208	100.0198
1.00E-08	9.7640E-01	9.7642E-01	9.7661E-01	100.0218	100.0198
1.00E-09	9.7600E-01	9.7642E-01	9.7661E-01	100.0626	100.0198
1.00E-10	9.6975E-01	9.7642E-01	9.7661E-01	100.7078	100.0198

Table 5.20 Verification of design variable σ design sensitivity (9,000-10,000 steps)

Perturbation amount	(a) FDM	(b) DDM	(c) AVM	(c)/(a) (%)	(c)/(b) %
1.00E-02	-8.3844E+00	-7.7049E+00	-7.7069E+00	91.9194	100.0267
1.00E-03	-7.6454E+00	-7.7049E+00	-7.7069E+00	100.8053	100.0267
1.00E-04	-7.5921E+00	-7.7049E+00	-7.7069E+00	101.5128	100.0267
1.00E-05	-7.4706E+00	-7.7049E+00	-7.7069E+00	103.1637	100.0267
1.00E-06	-7.8294E+00	-7.7049E+00	-7.7069E+00	98.4363	100.0267
1.00E-07	-1.0606E+01	-7.7049E+00	-7.7069E+00	72.6689	100.0267
1.00E-08	-7.7049E+00	-7.7049E+00	-7.7069E+00	100.0263	100.0267
1.00E-09	-7.7050E+00	-7.7049E+00	-7.7069E+00	100.0249	100.0267
1.00E-10	-7.7102E+00	-7.7049E+00	-7.7069E+00	99.9571	100.0267

Table 5.21 Verification of 2nd order analytical sensitivity (9,000-10,000 steps)

Perturbation amount	(a) FDM	(b) Analytical	(b)/(a) (%)
1.00E-02	1.8833E-01	1.7586E-01	93.3786
1.00E-03	1.7514E-01	1.7586E-01	100.4111
1.00E-04	9.2988E-02	1.7586E-01	189.1212
1.00E-05	1.7547E-01	1.7586E-01	100.2232
1.00E-06	1.7432E-01	1.7586E-01	100.8834
1.00E-07	1.7578E-01	1.7586E-01	100.0455
1.00E-08	1.7516E-01	1.7586E-01	100.3996
1.00E-09	1.7580E-01	1.7586E-01	100.0341
1.00E-10	1.8243E-01	1.7586E-01	96.3986
1.00E-11	1.8689E-01	1.7586E-01	94.0981
1.00E-12	2.3592E-01	1.7586E-01	74.5422

Through Table 5.22 to Table 5.25, design sensitivity analysis results for gold nanoparticle on a potential wall substrate are shown for longer time interval, between 80,000 and 100,000 steps. Random and design variables are the initial velocity and force field parameters between gold nanoparticle and the substrate, respectively. Performance measure is time averaged potential energy of gold nanoparticles between time intervals. As we can see from the DSA results, analytical direct differential and adjoint sensitivities always shows good agreement regardless of the perturbation amount. Even for the second order sensitivity, as shown in Table 5.25, analytical sensitivity shows converged value independent to the perturbation amount. However, the finite difference sensitivity shows large variance not only for first order but also for second order sensitivity depending on the perturbation amount. Too much or small perturbation leads to numerical error in finite difference method. This indicates that the accuracy of the sensitivity obtained from finite difference method is not reliable. Therefore, we can conclude that the finite difference sensitivity is improper to be used for sensitivity analysis for nanomaterials.

Table 5.22 Verification of random initial velocity design sensitivity (80,000-100,000 steps)

Perturbation amount	(a) FDM	(b) DDM	(c) AVM	(c)/(a) (%)	(c)/(b) %
1.00E-02	3.1157E-01	2.4223E-01	2.4229E-01	77.7652	100.0246
1.00E-03	3.8226E-01	2.4223E-01	2.4229E-01	63.3836	100.0246
1.00E-04	2.8957E-01	2.4223E-01	2.4229E-01	83.6718	100.0246
1.00E-05	1.0550E+00	2.4223E-01	2.4229E-01	22.9663	100.0246
1.00E-06	2.8459E+00	2.4223E-01	2.4229E-01	8.5136	100.0246
1.00E-07	1.0512E+01	2.4223E-01	2.4229E-01	2.3049	100.0246
1.00E-08	2.4010E-01	2.4223E-01	2.4229E-01	100.9116	100.0246
1.00E-09	2.3601E-01	2.4223E-01	2.4229E-01	102.6591	100.0246
1.00E-10	2.0009E-01	2.4223E-01	2.4229E-01	121.0911	100.0246
1.00E-11	6.0254E-01	2.4223E-01	2.4229E-01	40.2114	100.0246
1.00E-12	-2.9559E+00	2.4223E-01	2.4229E-01	-8.1969	100.0246

Table 5.23 Verification of design variable ε design sensitivity (80,000-100,000 steps)

Perturbation amount	(a) FDM	(b) DDM	(c) AVM	(c)/(a) (%)	(c)/(b) %
1.00E-02	1.0385E+01	6.3578E+01	6.3578E+01	612.2153	99.9987
1.00E-03	7.5919E+01	6.3578E+01	6.3578E+01	83.7441	99.9987
1.00E-04	7.2787E+01	6.3578E+01	6.3578E+01	87.3474	99.9987
1.00E-05	7.0341E+01	6.3578E+01	6.3578E+01	90.3845	99.9987
1.00E-06	7.5057E+01	6.3578E+01	6.3578E+01	84.7056	99.9987
1.00E-07	9.5037E+01	6.3578E+01	6.3578E+01	66.8973	99.9987
1.00E-08	1.6025E+02	6.3578E+01	6.3578E+01	39.6740	99.9987
1.00E-09	6.3569E+01	6.3578E+01	6.3578E+01	100.0134	99.9987
1.00E-10	6.3530E+01	6.3578E+01	6.3578E+01	100.0741	99.9987
1.00E-11	6.2499E+01	6.3578E+01	6.3578E+01	101.7251	99.9987
1.00E-12	5.7014E+01	6.3578E+01	6.3578E+01	111.5122	99.9987

Table 5.24 Verification of design variable σ design sensitivity (80,000-100,000 steps)

Perturbation amount	(a) FDM	(b) DDM	(c) AVM	(c)/(a) (%)	(c)/(b) %
1.00E-02	1.5308E+00	-7.3708E+01	-7.3707E+01	-4814.7676	99.9984
1.00E-03	-2.2687E+01	-7.3708E+01	-7.3707E+01	324.8889	99.9984
1.00E-04	-7.6671E+01	-7.3708E+01	-7.3707E+01	96.1334	99.9984
1.00E-05	-8.2298E+01	-7.3708E+01	-7.3707E+01	89.5612	99.9984
1.00E-06	-9.3498E+01	-7.3708E+01	-7.3707E+01	78.8326	99.9984
1.00E-07	-9.6156E+01	-7.3708E+01	-7.3707E+01	76.6531	99.9984
1.00E-08	-7.0224E+01	-7.3708E+01	-7.3707E+01	104.9599	99.9984
1.00E-09	-7.3720E+01	-7.3708E+01	-7.3707E+01	99.9819	99.9984
1.00E-10	-7.3860E+01	-7.3708E+01	-7.3707E+01	99.7923	99.9984
1.00E-11	-7.3197E+01	-7.3708E+01	-7.3707E+01	100.6959	99.9984
1.00E-12	-7.0997E+01	-7.3708E+01	-7.3707E+01	103.8159	99.9984

Table 5.25 Verification of 2nd order analytical sensitivity (80,000-100,000 steps)

Perturbation amount	(a) FDM	(b) Analytical	(b)/(a) (%)
1.00E-02	-1.0792E+02	-2.5133E+02	232.8855
1.00E-03	-1.2055E+02	-2.5133E+02	208.4861
1.00E-04	-2.7657E+02	-2.5133E+02	90.8739
1.00E-05	3.7480E+01	-2.5133E+02	-670.5710
1.00E-06	5.9921E+02	-2.5133E+02	-41.9436
1.00E-07	3.4959E+03	-2.5133E+02	-7.1893
1.00E-08	-2.5152E+02	-2.5133E+02	99.9245
1.00E-09	-2.5701E+02	-2.5133E+02	97.7900
1.00E-10	-3.3948E+02	-2.5133E+02	74.0338
1.00E-11	-1.7551E+02	-2.5133E+02	143.1998
1.00E-12	-9.6989E+00	-2.5133E+02	2591.3248

5.2.3 Uncertainties from random initial velocity

We perform first-order reliability method (FORM) analysis to estimate the effect of random initial velocity to the variance of the performance measure and the sensitivity. The FORM analysis is directly carried out based on the sensitivity analysis from the previous section. The model is the gold nanoparticle on a potential wall substrate. The performance measure is the time averaged gold nanoparticle potential energy between time intervals between 9,000 and 10,000 steps. The uncertainty from random initial velocity is considered by assuming that it follows a normal distribution. The initial velocity of the gold nanoparticle is parameterized random variable \mathbf{X} as $\mathbf{v}(\mathbf{X}) = \mathbf{v}^0 (1 + \mathbf{X})^{\frac{1}{2}}$. The random variable has mean of 0 and the standard deviation of 10^{-2} , $\mathbf{X} \sim N(0, (10^{-2})^2)$. To verify the accuracy of the first-order reliability method analysis, an independent Monte Carlo MD simulation is performed with 1,000 samples for both the performance measure and the sensitivity.

The histogram of the performance measure and the sensitivity with corresponding normal distribution is shown in Figure 5.20 and Figure 5.21. Table 5.26 shows the comparison between FORM analysis and 1,000 Monte Carlo simulation for the performance measure. ψ and σ are the performance measure and the standard deviation of the performance measure. As we can see, the standard deviation of the performance measure obtained from FORM analysis excellently agrees with 1,000 Monte Carlo simulation results even though the sampling number is relatively small. Furthermore, the performance measure obtained from Monte Carlo simulation agrees well with the performance measure at the mean value of the random initial velocity. This indicates that, by performing a simple first-order reliability method analysis based on the developed design sensitivity, we can easily obtain the standard deviation of the performance measure of interest without tedious repetition of same simulation with different initial condition to insure the reliability of the simulation by standard error analysis. These results indicate

that performing FORM analysis based on the developed design sensitivity could accurately and efficiently estimate the variance of the performance measure due to uncertainties in the MD simulation.

Table 5.27 shows the comparison between FORM analysis and 1,000 Monte Carlo simulation for the sensitivity of the performance measure with respect to the random initial velocity. The superscript ()' indicates values of the sensitivity. As shown in the table, we can notice that the FORM analysis using the second order sensitivity to estimate the variance of the sensitivity also works well compared to the Monte Carlo simulation with about 90% agreement. Accuracy slightly decreases in the FORM analysis for the sensitivity compared to the performance measure one. This is because we need to use the second order sensitivity to obtain the variance of the sensitivity in FORM analysis.

Table 5.26 Accuracy of FORM analysis for performance measure

(a) σ_{FORM}	(b) $\sigma_{1,000}$	(b)/(a) (%)	(c) $\psi_{at\ mean}$	(d) $\psi_{1,000}$	(d)/(c) (%)
1.4131E-03	1.4268E-03	100.97	-4.0768E+02	-4.0768E+02	100.00

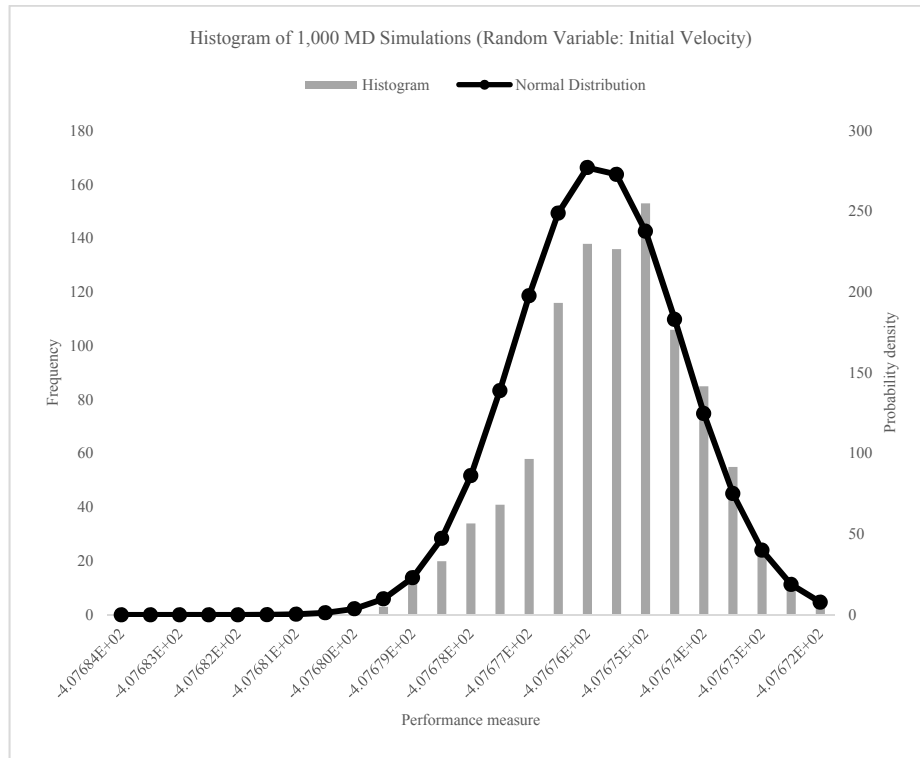


Figure 5.20 Performance measure histogram of 1,000 MD simulations and its normal distribution graph

Table 5.27 Accuracy of FORM analysis for sensitivity

(a) σ'_{FORM}	(b) $\sigma'_{1,000}$	(b)/(a) (%)	(c) ψ'_{atmean}	(d) $\psi'_{1,000MC}$	(d)/(c) (%)
1.7586E-03	1.8807E-03	106.95	9.7642E-01	9.7645E-01	100.00

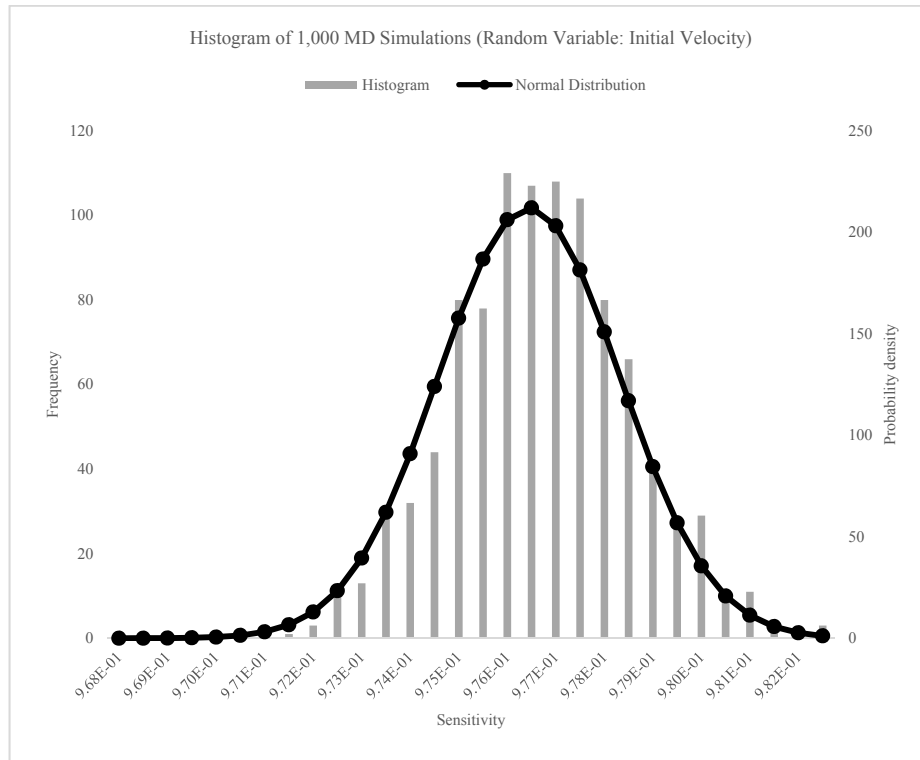


Figure 5.21 Sensitivity histogram of 1,000 MD simulations and its normal distribution graph

5.3 Atomic Mass Uncertainty: 3-D Gas Diffusion Problem

In this example, as shown in Figure 5.22, a 3-dimensional gas diffusion problem consist of 500 atoms is considered to verify the developed adjoint design sensitivity analysis method and to show the variance of performance measure and sensitivity due the uncertainty from mass and force field parameter. In this problem, a 12-6 Lennard-Jones (L-J) is utilized as an interatomic potential as

$$\Phi = 4\varepsilon \left\{ \left(\frac{\sigma}{r} \right)^{12} - \left(\frac{\sigma}{r} \right)^6 \right\}, \quad (5.3.1)$$

where r , σ and ε are $r = |r_i - r_j|$, collision diameter and energy depth, respectively. The velocity Verlet algorithm is employed for the temporal integration scheme since it can provide displacement and velocity information at the same time. In the 3-dimensional gas diffusion problem, the performance measure of interest is the diffusivity of gas at the terminal time of t_T MD simulation as

$$\psi = D(\mathbf{u}, \dot{\mathbf{u}}) = \frac{1}{3N_a} \mathbf{u}^T \dot{\mathbf{u}} \Big|_{t=t_T}, \quad (5.3.2)$$

where N_a , \mathbf{u} and $\dot{\mathbf{u}}$ are number of atoms, displacement and velocity vectors, respectively. For simplicity, 1.0 is employed for collision diameter, energy depth, and atomic mass. This example is prepared for academic demonstration purpose.

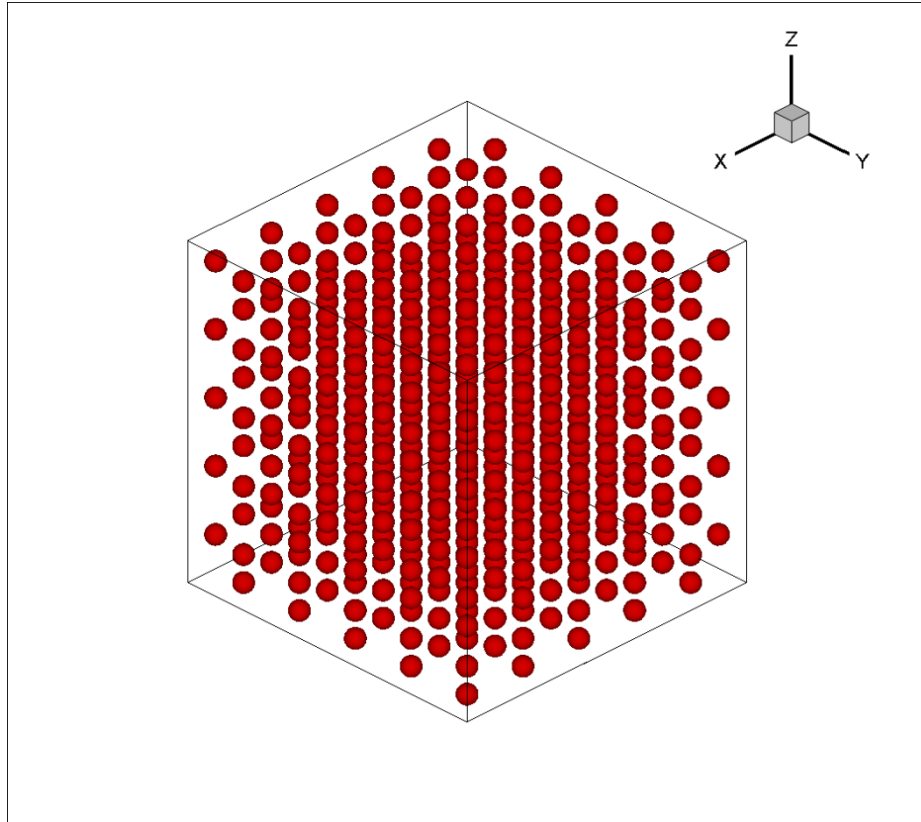


Figure 5.22 Initial configuration of 3-dimensional gas atoms

5.3.1 Verification of developed design sensitivity

Here, we perform design sensitivity analysis to verify the accuracy of the developed adjoint design sensitivity and second order analytical sensitivity with respect to random and design variables which are atomic mass and energy depth ε by comparing it to the finite difference sensitivity. The performance measure is the above mentioned terminal time diffusivity of gas atoms, 1,000 steps. We utilized 0.1fs as time step size. The results are shown through Table 5.28 to Table 5.30. The accuracy of the developed adjoint design sensitivity with respect to the random atomic mass and design variable is shown in Table 5.28 and Table 5.29 by comparison between the finite

difference sensitivity obtained from finite difference method. The perturbation amount varies from 1.e-2 to 1.e-15. The developed analytical adjoint design sensitivity shows good agreement with the sensitivity obtained from the finite difference method regardless of the perturbation amount.

Table 5.28 Verification of random initial velocity design sensitivity

Perturbation amount	Perturbed design	Original design	(a) FDM	(b) AVM	(b)/(a) (%)
1.00E-02	-4.0559E-03	-4.0925E-03	3.6546E-03	5.3289E-03	145.8113
1.00E-03	-4.0869E-03	-4.0925E-03	5.5627E-03	5.3289E-03	95.7965
1.00E-04	-4.0919E-03	-4.0925E-03	5.6772E-03	5.3289E-03	93.8639
1.00E-05	-4.0924E-03	-4.0925E-03	6.1381E-03	5.3289E-03	86.8157
1.00E-06	-4.0925E-03	-4.0925E-03	4.6154E-03	5.3289E-03	115.4594
1.00E-07	-4.0925E-03	-4.0925E-03	5.3288E-03	5.3289E-03	100.0004
1.00E-08	-4.0925E-03	-4.0925E-03	5.3289E-03	5.3289E-03	99.9999
1.00E-09	-4.0925E-03	-4.0925E-03	5.3289E-03	5.3289E-03	99.9996
1.00E-10	-4.0925E-03	-4.0925E-03	5.3298E-03	5.3289E-03	99.9825
1.00E-11	-4.0925E-03	-4.0925E-03	5.3351E-03	5.3289E-03	99.8840
1.00E-12	-4.0925E-03	-4.0925E-03	5.3499E-03	5.3289E-03	99.6071

Table 5.29 Verification of design variable ε design sensitivity

Perturbation amount	Perturbed design	Original design	(a) FDM	(b) AVM	(b)/(a) (%)
1.00E-02	-4.1696E-03	-4.0925E-03	-7.7137E-03	-5.3289E-03	69.0835
1.00E-03	-4.0984E-03	-4.0925E-03	-5.9675E-03	-5.3289E-03	89.2986
1.00E-04	-4.0930E-03	-4.0925E-03	-5.7279E-03	-5.3289E-03	93.0334
1.00E-05	-4.0925E-03	-4.0925E-03	-6.3380E-03	-5.3289E-03	84.0784
1.00E-06	-4.0925E-03	-4.0925E-03	-7.0656E-03	-5.3289E-03	75.4203
1.00E-07	-4.0925E-03	-4.0925E-03	-5.3289E-03	-5.3289E-03	99.9996
1.00E-08	-4.0925E-03	-4.0925E-03	-5.3289E-03	-5.3289E-03	100.0000
1.00E-09	-4.0925E-03	-4.0925E-03	-5.3288E-03	-5.3289E-03	100.0014
1.00E-10	-4.0925E-03	-4.0925E-03	-5.3284E-03	-5.3289E-03	100.0087
1.00E-11	-4.0925E-03	-4.0925E-03	-5.3220E-03	-5.3289E-03	100.1298
1.00E-12	-4.0925E-03	-4.0925E-03	-5.2501E-03	-5.3289E-03	101.4995

Table 5.30 shows the accuracy of the analytical second order design sensitivity with respect to the random and design variable which are the atomic mass and the potential parameter ε . The finite difference sensitivity is obtained by varying the perturbation amount from 1.e-2 to 1.e-15. For the second order sensitivity, the finite difference sensitivity is extremely sensitivity compared to the analytical sensitivity regarding to the perturbation amount. This indicates that the finite difference sensitivity is not applicable in MD simulation problems since its accuracy depends on the perturbation amount. Therefore, we can conclude that the development of the analytical sensitivity analysis method is essential for precise nanoscale design problems.

Table 5.30 Verification of second order analytical sensitivity

Perturbation amount	(a) FDM	(b) analytical	(b)/(a) (%)
1.00E-02	4.0590E-01	4.0338E-01	99.3791
1.00E-03	4.0478E-01	4.0338E-01	99.6559
1.00E-04	5.0684E-01	4.0338E-01	79.5882
1.00E-05	1.9984E+01	4.0338E-01	2.0186
1.00E-06	2.4502E+03	4.0338E-01	0.0165
1.00E-07	3.9925E-01	4.0338E-01	101.0359
1.00E-08	-1.4745E-01	4.0338E-01	-273.5697
1.00E-09	-5.9848E+01	4.0338E-01	-0.6740
1.00E-10	-7.8063E+03	4.0338E-01	-0.0052
1.00E-11	-1.1276E+06	4.0338E-01	0.0000
1.00E-12	-1.7347E+07	4.0338E-01	0.0000

5.3.2 Uncertainties from random atomic mass

We perform first-order reliability method (FORM) analysis to estimate the effect of random atomic mass to the variance of the performance measure and the sensitivity. The FORM analysis is directly carried out based on the obtained analytical sensitivity from the previous section. The uncertainty from randomness of atomic mass is considered by assuming that it follows a normal distribution. The random mass distribution of gas atoms is parameterized as $m_a = 1.0 + \mathbf{X}$ where random variable \mathbf{X} has mean of 0 and the standard deviation of 10^{-2} , $\mathbf{X} \sim N\left(0, (10^{-2})^2\right)$. To compare the accuracy of first-order reliability method analysis based on the developed sensitivity, an independent Monte Carlo MD simulation is performed with 1,000 samples for both the performance measure and the sensitivity.

Table 5.31 shows the comparison between FORM analysis and 1,000 Monte Carlo simulation for the performance measure which is the terminal time gas diffusion. ψ and σ are the performance measure and the standard deviation of the performance measure. As we can see, the standard deviation of the performance measure obtained from FORM analysis excellently agrees with 1,000 Monte Carlo simulation results even though the sampling number is relatively small compared to the conventional ones. Furthermore, the performance measure obtained from Monte Carlo simulation agrees well with the performance measure at the mean value of the random initial velocity. This indicates that, by performing a simple first-order reliability method analysis based on the developed design sensitivity, we can easily obtain the standard deviation of the performance measure of interest without tedious repetition of same simulation with different initial condition to insure the reliability of the simulation by standard error analysis. Table 5.32 shows the comparison between FORM analysis and 1,000 Monte Carlo simulation for the sensitivity of the performance measure with respect to the random initial velocity. As shown in the table, we can notice that the FORM analysis using the second order sensitivity to estimate the variance of the sensitivity also works well compared to the Monte Carlo simulation.

These results indicate that performing FORM analysis based on the developed design sensitivity could not only accurately estimate the variance of the performance measure due to uncertainties but also liberate the tremendous computation cost to insure the reliability of the MD simulation which is almost always a burden work. In Table 5.33, the normalized computation cost for Monte Carlo simulation and FORM analysis for performance measure and sensitivity is shown. For evaluation of the variance of the performance measure, it only takes 0.16% computation cost for sensitivity based FORM analysis compared to the Monte Carlo simulation. For the evaluation of the impact of uncertainty in DSA of MD it take only 0.11% computation cost compared to the 1,000 Monte Carlo simulation. This indicates that, since the first order sensitivity with respect to random variable is necessary for calculation of the second order sensitivity, we can simultaneously evaluate the uncertainty effect in both MD simulation and DSA of MD with computation cost about only 1 additional MD simulation.

Table 5.31 Accuracy of FORM analysis for performance measure

(a) σ_{FORM}	(b) $\sigma_{1,000}$	(b)/(a) (%)	(c) $\Psi_{at\ mean}$	(d) $\Psi_{1,000}$	(d)/(c) (%)
5.3289E-05	6.0724E-05	113.95	-4.0925E-03	-4.1128E-03	100.50

Table 5.32 Accuracy of FORM analysis for sensitivity

(a) σ'_{FORM}	(b) $\sigma'_{1,000}$	(b)/(a) (%)	(c) $\Psi'_{at\ mean}$	(d) $\Psi'_{1,000MC}$	(d)/(c) (%)
4.0338E-03	3.2830E-03	99.06	-5.3289E-03	-5.1192E-03	96.07

Table 5.33 Comparison of computation cost

	MC for analysis	FORM for analysis	MC for DSA	FORM for sensitivity
Normalized computation cost	1.00	0.0016	1.00	0.0011

5.4 1-Dimensional Harmonic Oscillator Problem

In this example, as shown in Figure 5.23, a simple 1-dimensional harmonic oscillator problem consist of 201 atoms is considered to verify the developed adjoint design sensitivity analysis method and to show the variance of performance measure and sensitivity due the uncertainty from random initial velocity. In the 1-dimensional harmonic oscillator problem, an impulse is applied at the center as an initial velocity $v_0^{101}(\mathbf{X})$. The performance measure of interest is the terminal time displacement of 151th atom $\psi(\mathbf{b}, \mathbf{X}) = u^{151}(t_T)$.

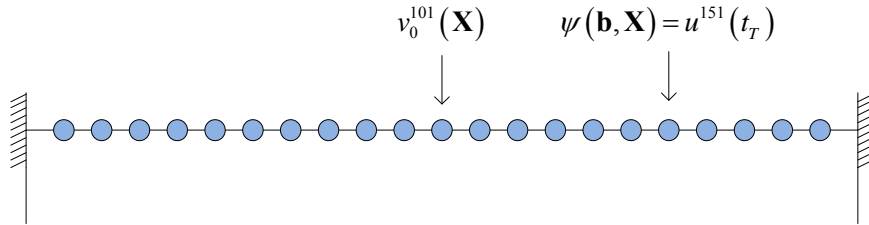


Figure 5.23 1-D harmonic oscillator with impulse at the center

In this problem, a following simple harmonic potential Φ is utilized as

$$\Phi = \sum_{i,j} \frac{1}{2} k (u_j - u_i)^2, \quad (5.4.1)$$

where k is the stiffness and u_i indicates the displacement of i^{th} atom.

The force acting on each i^{th} atom is easily obtained as a derivative of the harmonic potential with respect to its displacement as

$$f_i = -\frac{\partial\Phi}{\partial u_i} = ku_{i-1} - 2ku_i + ku_{i+1}. \quad (5.4.2)$$

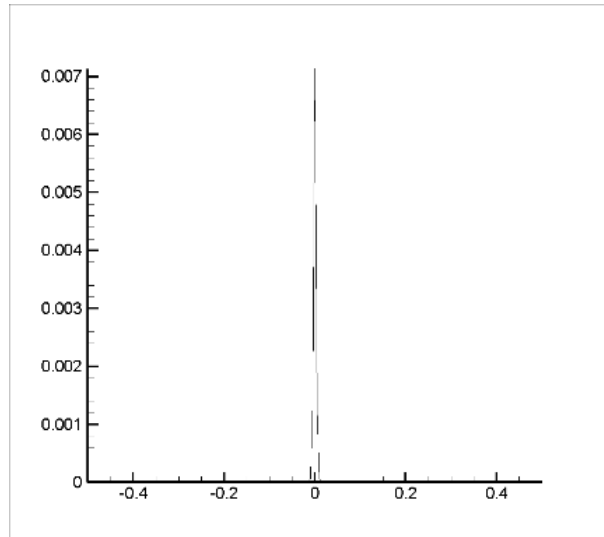
Then the equation of motion for the i^{th} atom is written as

$$m\ddot{u}_i = f_i. \quad (5.4.3)$$

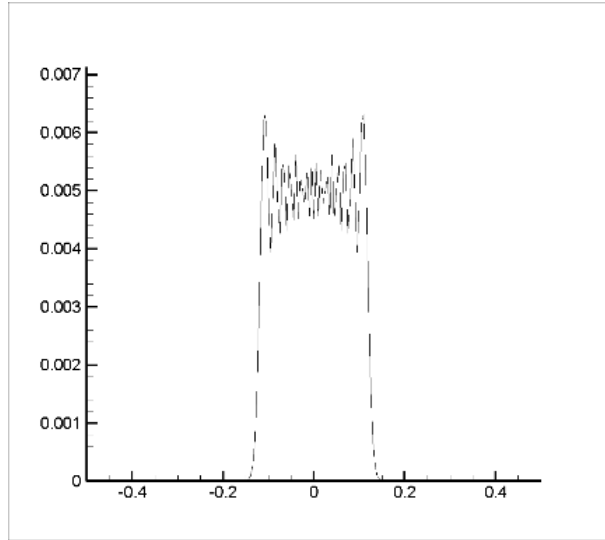
With the following initial displacement and velocity conditions

$$u_i(t_0) = u_i^0, \quad \dot{u}_i(t_0) = \dot{u}_i^0. \quad (5.4.4)$$

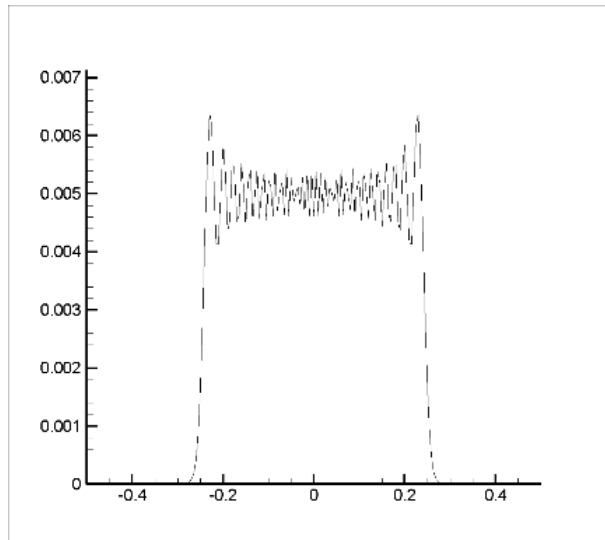
Figure 5.24 shows the displacement profile at 1, 500, and 1,000 steps of the 1-dimensional harmonic oscillator with an impulse on the center.



(a) 1 step



(b) 500 step



(c) 1,000 step

Figure 5.24 Displacement profile of 1-dimensional harmonic oscillator

5.4.1 Verification of developed design sensitivity

Here, we perform design sensitivity analysis to verify the accuracy of the developed adjoint design sensitivity and second order analytical sensitivity with respect to random and design variables by comparing it to the finite difference sensitivity. The initial velocity of the centered atom in the 1-dimensional harmonic oscillator is considered as the random variable and the stiffness of the atoms is considered as the design variable. For simplicity, we utilize dimensionless atomic mass $m=1.0$, stiffness $k=1.0$, and timestep size $\Delta t=0.05$. The performance measure is the above mentioned terminal time displacement of 151th atom. Terminal time of the simulation is 1,000 steps. For the verification purpose, the mean value $v_0^{101}(\mathbf{X})=0.01$ is utilized for the random initial velocity of centered atom in the 1-dimensional harmonic oscillator.

Table 5.34 shows the accuracy of the developed adjoint design sensitivity with respect to the random initial velocity compared to the finite difference sensitivity obtained from finite difference method by varying the perturbation amount from 1.e-2 to 1.e-15. The developed analytical adjoint design sensitivity shows excellent agreement with the sensitivity obtained from the finite difference method regardless of the perturbation amount used in it. This is due to the simplicity of the harmonic potential utilized for the atomic interactions.

Table 5.34 Verification of random initial velocity design sensitivity

Perturbation amount	Perturbed design	Original design	(a) FDM	(b) AVM	(b)/(a) (%)
1.00E-02	3.2944E-03	1.6472E-03	1.6472E-01	1.6472E-01	100.0000
1.00E-03	1.8119E-03	1.6472E-03	1.6472E-01	1.6472E-01	100.0000
1.00E-04	1.6637E-03	1.6472E-03	1.6472E-01	1.6472E-01	100.0000
1.00E-05	1.6488E-03	1.6472E-03	1.6472E-01	1.6472E-01	100.0000
1.00E-06	1.6474E-03	1.6472E-03	1.6472E-01	1.6472E-01	100.0000
1.00E-07	1.6472E-03	1.6472E-03	1.6472E-01	1.6472E-01	100.0000
1.00E-08	1.6472E-03	1.6472E-03	1.6472E-01	1.6472E-01	100.0000
1.00E-09	1.6472E-03	1.6472E-03	1.6472E-01	1.6472E-01	100.0000
1.00E-10	1.6472E-03	1.6472E-03	1.6472E-01	1.6472E-01	100.0000
1.00E-11	1.6472E-03	1.6472E-03	1.6472E-01	1.6472E-01	100.0001
1.00E-12	1.6472E-03	1.6472E-03	1.6472E-01	1.6472E-01	100.0001
1.00E-13	1.6472E-03	1.6472E-03	1.6470E-01	1.6472E-01	100.0115
1.00E-14	1.6472E-03	1.6472E-03	1.6499E-01	1.6472E-01	99.8341
1.00E-15	1.6472E-03	1.6472E-03	1.6003E-01	1.6472E-01	102.9319

Table 5.35 shows the accuracy of the analytical second order design sensitivity with respect to the random and design variable which are the initial velocity of centered atom and the stiffness of atoms consisting the 1-dimensional harmonic oscillator, respectively. Once again the finite difference sensitivity is obtained by varying the perturbation amount from 1.e-2 to 1.e-15. For the second order sensitivity, the finite difference sensitivity varies from 5 to 16% compared to the analytical sensitivity regarding to the perturbation amount used. This indicates that how simple the problem is, the finite difference sensitivity is not quite reliable since its accuracy depends on the perturbation amount. Furthermore, since we can see that the analytical sensitivity always gives converged sensitivity compared to the finite difference one, the development of the analytical sensitivity analysis method is essential for precise nanoscale design problems.

Table 5.35 Verification of second order analytical sensitivity

Perturbation amount	Perturbed design	Original design	(a) FDM	(b) analytical	(b)/(a) (%)
1.00E-02	1.8900E-03	1.6472E-03	2.4281E-02	2.3288E-02	95.9119
1.00E-03	1.6706E-03	1.6472E-03	2.3389E-02	2.3288E-02	99.5698
1.00E-04	1.6495E-03	1.6472E-03	2.3298E-02	2.3288E-02	99.9568
1.00E-05	1.6474E-03	1.6472E-03	2.3289E-02	2.3288E-02	99.9957
1.00E-06	1.6472E-03	1.6472E-03	2.3288E-02	2.3288E-02	99.9996
1.00E-07	1.6472E-03	1.6472E-03	2.3288E-02	2.3288E-02	100.0000
1.00E-08	1.6472E-03	1.6472E-03	2.3288E-02	2.3288E-02	100.0000
1.00E-09	1.6472E-03	1.6472E-03	2.3288E-02	2.3288E-02	100.0000
1.00E-10	1.6472E-03	1.6472E-03	2.3288E-02	2.3288E-02	100.0002
1.00E-11	1.6472E-03	1.6472E-03	2.3288E-02	2.3288E-02	100.0006
1.00E-12	1.6472E-03	1.6472E-03	2.3290E-02	2.3288E-02	99.9922
1.00E-13	1.6472E-03	1.6472E-03	2.3200E-02	2.3288E-02	100.3810
1.00E-14	1.6472E-03	1.6472E-03	2.3007E-02	2.3288E-02	101.2230
1.00E-15	1.6472E-03	1.6472E-03	1.9949E-02	2.3288E-02	116.7365

5.4.2 Uncertainties from random initial velocity

We perform first-order reliability method (FORM) analysis to estimate the effect of random initial velocity to the variance of the performance measure and the sensitivity. The FORM analysis is directly carried out based on the sensitivity analysis from the previous section. The model is above mentioned 1-dimensional harmonic oscillator where an impulse is applied as an initial velocity of the centered atom. The performance measure is the terminal time displacement of 151th atom where random variable is the initial velocity of 101th atom and the design variable is the stiffness of the atoms consisting the 1-dimensional harmonic oscillator. The uncertainty from random initial velocity is considered by assuming that it follows a normal distribution. The initial velocity of the centered atom is parameterized as $v_0^{101} = 0.01 + \mathbf{X}$ where random variable \mathbf{X} has mean of 0 and the standard deviation of 10^{-4} , $\mathbf{X} \sim N\left(0, (10^{-4})^2\right)$. To verify the accuracy of first-order reliability method analysis based on the developed sensitivity, an independent Monte Carlo MD simulation is performed with 1,000 samples for both the performance measure and the sensitivity. The histogram of the performance measure and the sensitivity with corresponding normal distribution is shown in Figure 5.25 and Figure 5.26. Table 5.36 shows the comparison between FORM analysis and 1,000 Monte Carlo simulation for the performance measure which is the terminal time displacement of the 151th atom. μ and σ are the performance measure and the standard deviation of the performance measure. As we can see, the standard deviation of the performance measure obtained from FORM analysis excellently agrees with 1,000 Monte Carlo simulation results even though the sampling number is relatively small compared to the conventional ones. Furthermore, the performance measure obtained from Monte Carlo simulation agrees well with the performance measure at the mean value of the random initial velocity. This indicates that, by performing a simple first-order reliability method analysis based on the developed adjoint design sensitivity, we can easily obtain the standard deviation of the performance measure of interest without

tedious repetition of same simulation with different initial condition to insure the reliability of the simulation by standard error analysis.

Table 5.37 shows the comparison between FORM analysis and 1,000 Monte Carlo simulation for the sensitivity of the performance measure with respect to the random initial velocity. The superscript ()' indicates values of the sensitivity. As shown in the table, we can notice that the FORM analysis using the second order sensitivity to estimate the variance of the sensitivity also works well compared to the Monte Carlo simulation with excellent agreement.

Now, we show the efficiency of FORM analysis based on the developed design sensitivity by comparing the computation time of MD simulation and DSA of MD. In Table 5.38, the normalized computation cost for Monte Carlo simulation and FORM analysis for performance measure and sensitivity is shown. For evaluation of the variance of the performance measure, it only takes 0.014% computation cost for sensitivity based FORM analysis compared to the Monte Carlo simulation. For the evaluation of the impact of uncertainty in DSA of MD it take only 0.016% computation cost compared to the 1,000 Monte Carlo simulation. For a simple 1-D harmonic oscillator problem, only 0.16% of additional computation cost to the simulation is required to simultaneously evaluate the uncertainty effect in both MD simulation and DSA of MD. This indicates that the developed method is very efficient with precise accuracy.

Table 5.36 Accuracy of FORM analysis for performance measure

(a) σ_{FORM}	(b) $\sigma_{1,000}$	(b)/(a) (%)	(c) $\Psi_{at\ mean}$	(d) $\Psi_{1,000}$	(d)/(c) (%)
1.6263E-05	1.6263E-05	100.00	1.6472E-03	1.6472E-03	100.00

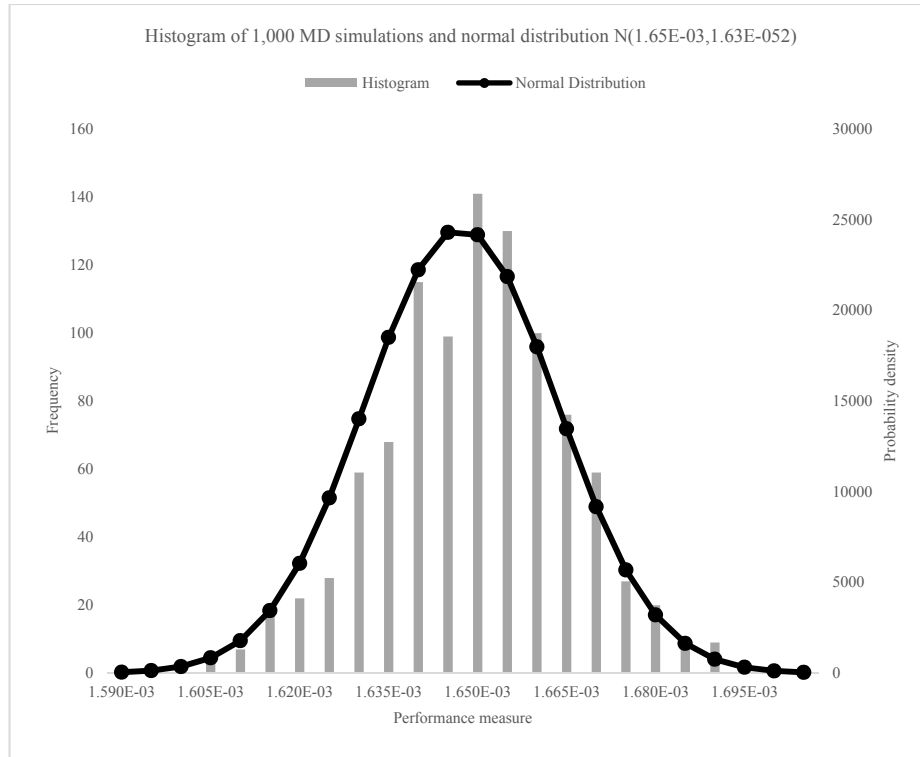


Figure 5.25 Performance measure histogram of 1,000 MD simulations and its normal distribution graph

Table 5.37 Accuracy of FORM analysis for sensitivity

(a) σ'_{FORM}	(b) $\sigma'_{1,000}$	(b)/(a) (%)	(c) $\psi'_{at\ mean}$	(d) $\psi'_{1,000MC}$	(d)/(c) (%)
2.3288E-04	2.2993E-04	101.28	2.3288E-02	2.3288E-02	100.00

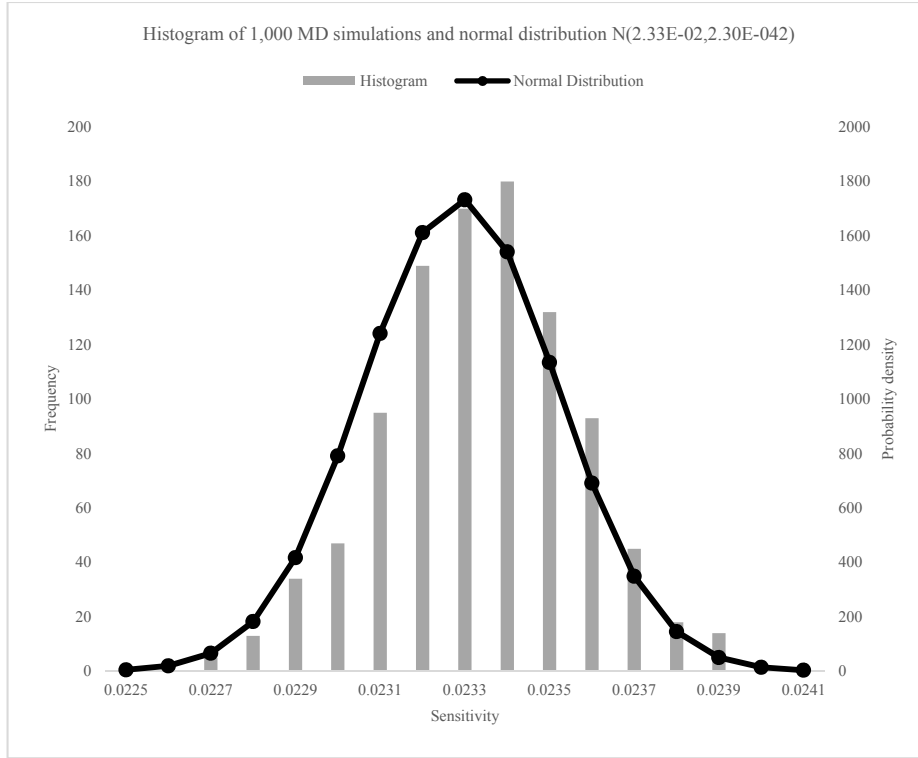


Figure 5.26 Sensitivity histogram of 1,000 MD simulations and its normal distribution graph

Table 5.38 Comparison of computational cost

	MC for analysis	FORM for analysis	MC for DSA	FORM for sensitivity
Normalized computation cost	1.00	0.00014	1.00	0.00016

5.4.3 Reliability based sensitivity analysis

For the reliable and robust design of the MD system consider a aforementioned 1-D harmonic oscillator with 1-D Gaussian wave propagation. The region designated for MD simulation is $-1nm \leq x \leq 1nm$ and there are 201 atoms in the region. The initial condition for the displacement is Gaussian pulse of amplitude A and width h . The pulse is ranged at $-L_c \leq x \leq L_c$, and includes fine scale perturbation $(1+b\cos(2\pi x/H))$, where H is a length scale that is small compared to h . b is the relative amplitude of the perturbation. The initial displacement is

$$u(x, t=0) = \begin{cases} A \frac{e^{-(x/h)^2} - z_c}{1 - z_c} \left\{ 1 + b \cos\left(\frac{2\pi x}{H}\right) \right\} & \text{if } |x| \leq L_c \\ 0 & \text{if } |x| > L_c \end{cases}, \quad (5.4.5)$$

and the parameters for initial condition are $A = h_a = 0.01$ (nm), $b = 0.01$ (nm), $h = 20h_a$, $H = h/4$ (nm) and $L_c = 5h$ (nm).

A harmonic potential $\Phi(u) = \sum_{i \neq j} \frac{1}{2} k (u_j - u_i)^2$ is utilized and $k = 1$ for simplicity. Only the nearest neighborhood interactions are assumed. Design variables are taken to the mass values of atoms, $b_i = m_i$, ($i = 1, \dots, 201$). Performance measure is selected as the mean squared displacement (MSD) at terminal time, 1,000 steps, with time step size of $\Delta t = 0.05$. The uncertainties of MD results are due to the random initial velocities of atoms. Thus we consider that random variables are initial velocity $\mathbf{v}_0 = \mathbf{X} \in \mathbf{R}^{201}$ and all the random initial velocities are assumed statistically independent and normally distributed random variables which can be represented as $X_i \sim N\left(0, (10^{-4})^2\right)$, ($i = 1, \dots, 201$). For the reliable and robust design of the MD system, a probabilistic constraint related to the performance measure is additionally considered.

$$P_f = P[g(\mathbf{b}, \mathbf{X}) \leq 0] \leq P_f^{Tar}, \quad (5.4.6)$$

where the limit state function $g(\mathbf{b}, \mathbf{u})$ is given by

$$g(\mathbf{b}, \mathbf{X}) = \frac{\psi}{\psi_0} - 1 = \frac{\psi}{\alpha \psi \Big|_{\substack{\mathbf{b}=\mathbf{b}_0 \\ \mathbf{X}=\mathbf{X}_\mu}}} - 1, \quad (5.4.7)$$

where $\alpha=0.9$, meaning 90% of mean performance measure at initial design point. The target probability of failure, P_f^{Tar} , is not needed at DSA stage.

Transformation of \mathbf{X} into U -space

$$\mathbf{U} = \mathbf{T}(\mathbf{X}) = \Sigma^{-1}(\mathbf{X} - \mathbf{X}_\mu), \quad (5.4.8)$$

or

$$U_i = T_i(X_i) = \frac{X_i - \mu_i}{\sigma_i} = \frac{X_i}{10^{-4}}, \quad (i=1, \dots, 201), \text{ and } X_i = \sigma_i U_i. \quad (5.4.9)$$

The reliability analysis and sensitivity analysis of the reliability index β are performed: first, find most probable point (MPP) and evaluate the sensitivity of reliability index β at the MPP point. To find the MPP point, we performed a sub-optimization problem by utilizing modified most feasible direction method (MMFD) as

$$\text{Find } \mathbf{U}, \quad (5.4.10)$$

$$\text{Minimize } \|\mathbf{U}^T \mathbf{U}\|, \quad (5.4.11)$$

$$\text{Subject to } G(\mathbf{U}, \tilde{\mathbf{b}}) = 0, \quad (5.4.12)$$

where $\tilde{\mathbf{b}}$ denotes that the design point is fixed to the current design. The equality constraint in Equation (5.4.12) is rewritten as two inequality constraints and the sub-optimization problem is rewritten as

$$\text{Minimize } \|\mathbf{U}^T \mathbf{U}\|, \quad (5.4.13)$$

$$\text{Subject to } G(\mathbf{U}, \tilde{\mathbf{b}}) \leq 0, \quad -G(\mathbf{U}, \tilde{\mathbf{b}}) \leq 0 \quad (5.4.14)$$

After finding the MPP point, the sensitivity of the reliability index β is evaluated. Recall Equation (4.3.8),

$$\frac{\partial \beta}{\partial \mathbf{b}} = \frac{1}{\|\nabla g(\mathbf{U}^*, \mathbf{b})\|} \frac{\partial g^T(\mathbf{U}^*, \mathbf{b})}{\partial \mathbf{b}}, \quad (4.3.8)$$

where the norm of gradient $\|\nabla g(\mathbf{U}^*, \mathbf{b})\|$ is already available in the last iteration of sub-optimization problem and the gradient with respect to the design variables $\partial g^T(\mathbf{U}^*, \mathbf{b})/\partial \mathbf{b}$ is efficiently obtained by employing the adjoint variable method at the MPP point \mathbf{U}^* . To verify the adjoint sensitivity overall FDM is performed with various design optimization tool (DOT) parameters as Table 5.39.

Table 5.39 Verification of design variable ε design sensitivity (80,000-100,000 steps)

Design variable	g_U	δU^{\max}	(a) AVM $d\beta/db$	(b) FDM $\Delta\beta/\Delta b$	(a)/(b) (%)
101	1.00E-03	1.00E-06	1.1133E-01	1.0614E-01	104.89
	1.00E-04	1.00E-06	1.1134E-01	1.1107E-01	100.24
	1.00E-03	1.00E-11	1.1133E-01	2.2154E-01	50.25
	1.00E-04	1.00E-11	1.1134E-01	7.7455E-02	143.74

5.5 Agglomeration of nanoparticles on a substrate

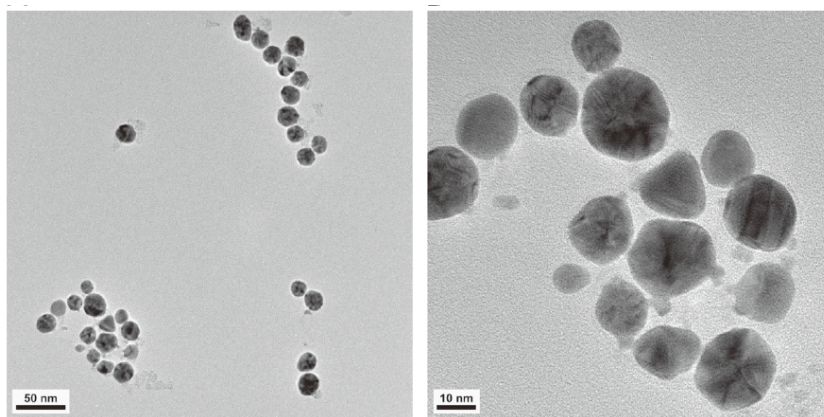
In this section, we show the accuracy and the efficiency of the developed method in evaluation of uncertainty effect to agglomeration of nanoparticles on a substrate phenomenon observed through cutting-edge microscopes. For a better understanding of the nanoscale phenomenon, other types of microscopes are utilized since an optical microscope has a limited capability in measuring and manipulating the nanoscale structures. To characterize the nanoscale geometry, there are two major types of measuring devices to obtain the nanoscale properties. One uses an electron beam which interacts with the atoms that make up the signals about the sample, such as scanning electron microscopy (SEM) and transmission electron microscopy (TEM). The other type is atomic force microscopy (AFM) that uses the deflection of cantilever according to the force between the specimen and the probe at the end of cantilever is one of the foremost tools for imaging, measuring, and manipulating in nanoscale. It is a very high-resolution type of scanning probe microscopy with a demonstrated resolution on the order of a nanometer which is more than 1,000 times better than the optical diffraction limit. The AFM gathers information by scanning the surface with a mechanical probe and provides high resolution images of the height and phase in nanoscale.

5.5.1 Experimental observation of nanoparticle agglomeration

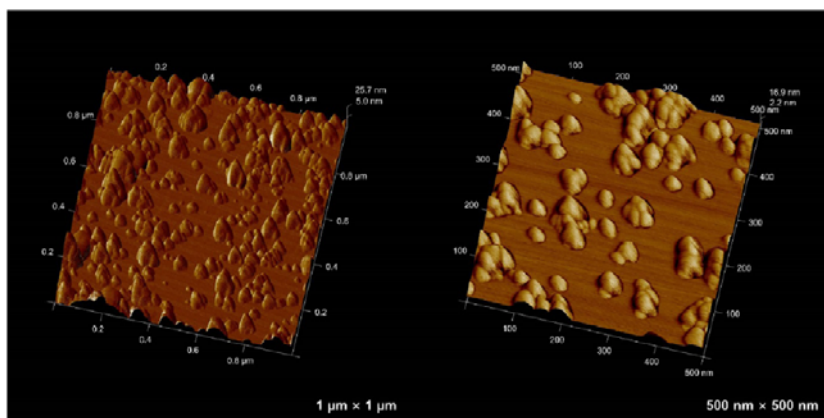
To precisely characterize the nanoscale geometry of nanoparticles, we experimentally observed the morphology of metallic nanoparticles with above mentioned cutting-edge microscopes, High Resolution-TEM (HR-TEM), Field Emission-SEM (FE-SEM), and AFM. As shown in Figure 5.27-(a) to Figure 5.27-(c), spherical and irregularly shaped gold nanoparticles were observed in all images and it corroborate each other. Furthermore, in Figure 5.27-(d), we measured the averaged diameters of AuNPs to be around about 20 to 50 nm. In addition to gold nanoparticles, we also observed the

morphology of silver nanoparticles (AgNPs) as shown in Figure 5.28-(a) and Figure 5.28-(b). In Figure 5.28-(c), a section analysis was performed on the AFM images of AgNPs to obtain the height information for the nanoparticles. Normally, a stabilized nanoparticles are known to have a spherical shape.

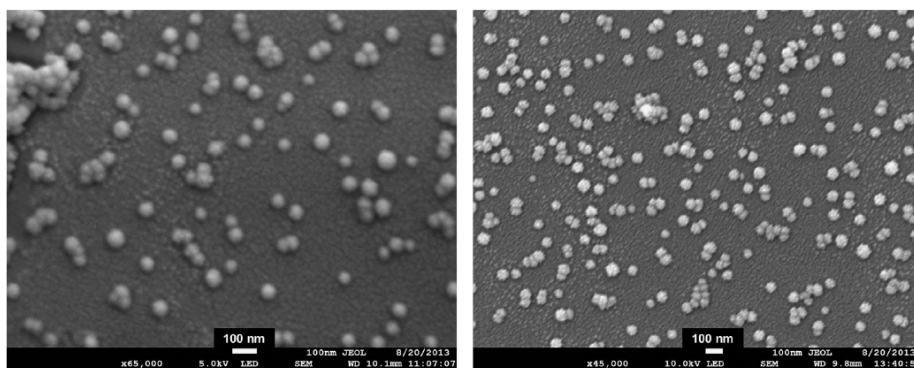
However, a large difference in the diameters between FE-SEM, AFM, and HR-TEM images in both Figure 5.27-(d) and Figure 5.28-(d). This difference mainly comes from the stabilization of nanoparticles depending on the type of substrate we utilized in the experiment. In HR-TEM observation, we used a grid type substrate. On the other hand, in FE-SEM and AFM observation we utilized a silica type substrate, mica. Due to the nature of aggregation in metallic materials at nanoscale, without any additional kinematic energies applied, the synthesized nanoparticles agglomerates on the substrate even after the chemical reaction until it is stabilized at ambient condition. Consequently, the diameter gets larger until the equilibrium is reached on the mica substrate due to the horizontal agglomeration while the height remains similar with the average diameter as observed in the HR-TEM images.



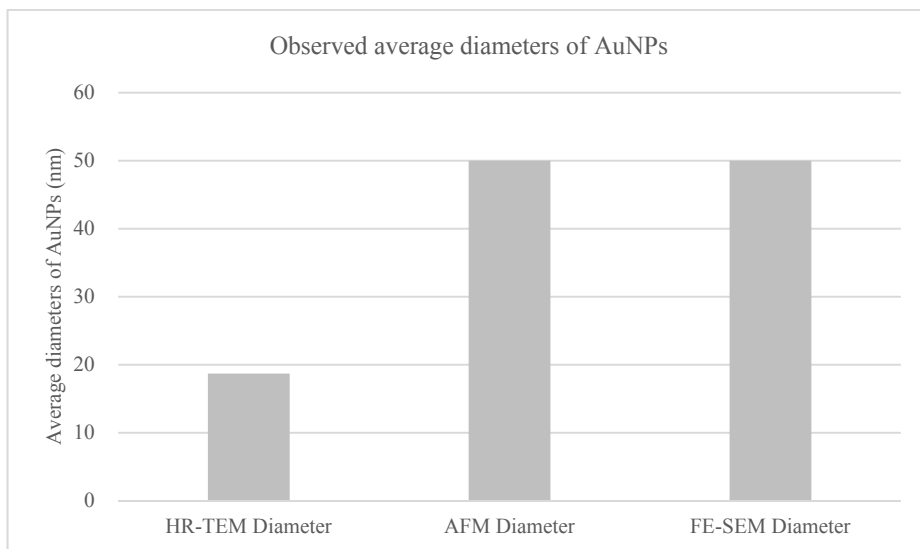
(a) HR-TEM image of AuNPs ($D:18.71 \pm 2.90\text{nm}$)



(b) AFM image of AuNPs (D: 50 ± 5.70 nm, H: 16.3 ± 2.50 nm)

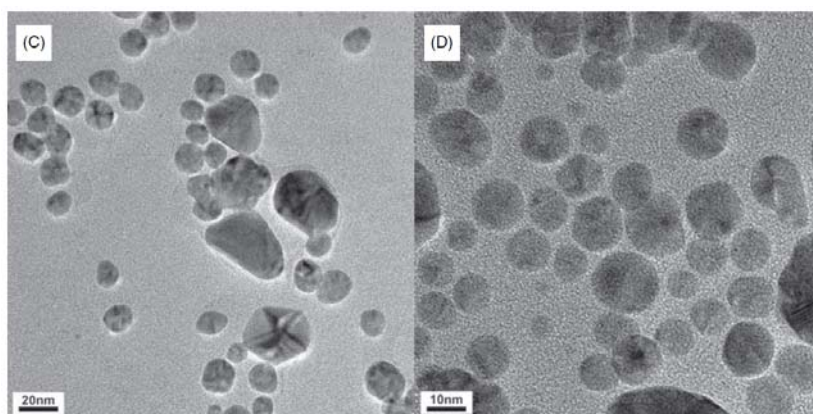


(c) FE-SEM image of AuNPs (D: ~ 50 nm)

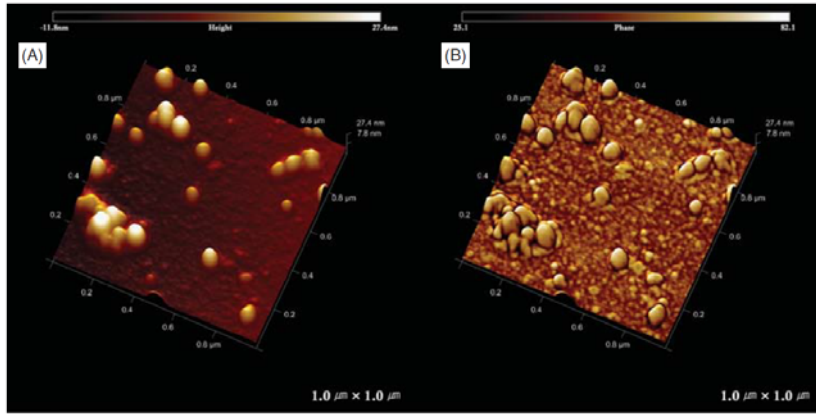


(d) Average observed diameters of AuNPs

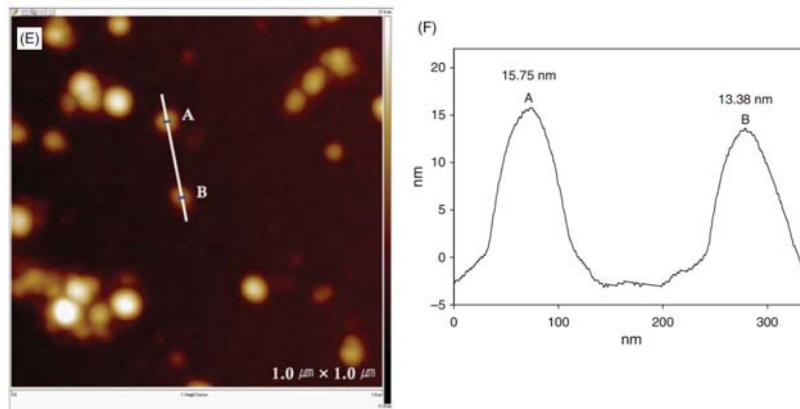
Figure 5.27 Morphology observation of AuNPs with various microscopes



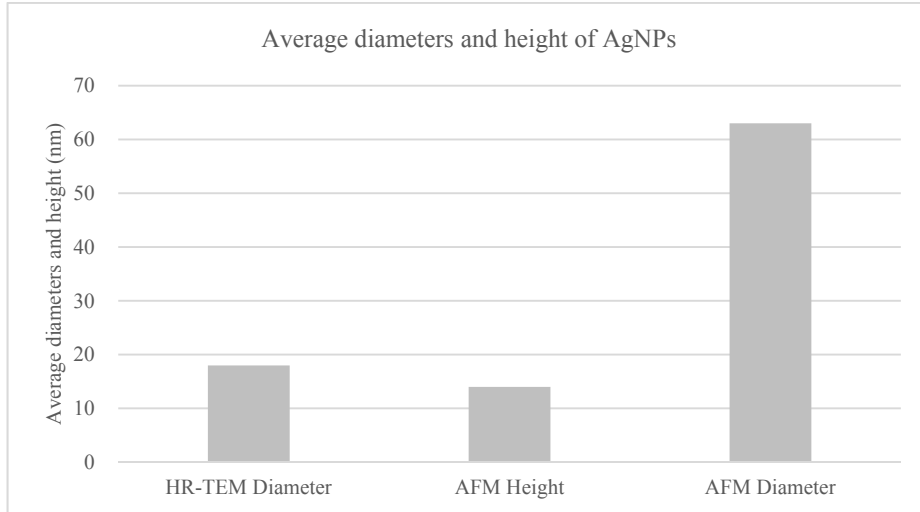
(a) HR-TEM image of AgNPs ($D:17.97 \pm 8.63$ nm)



(b) AFM images of AgNPs ($D: 63 \pm 5.63 \text{ nm}$)



(c) Section analysis of two AgNPs



(d) Average diameters and height of AgNPs

Figure 5.28 Morphology observation of AgNPs with various microscopes

5.5.2 Uncertainties from random initial velocity

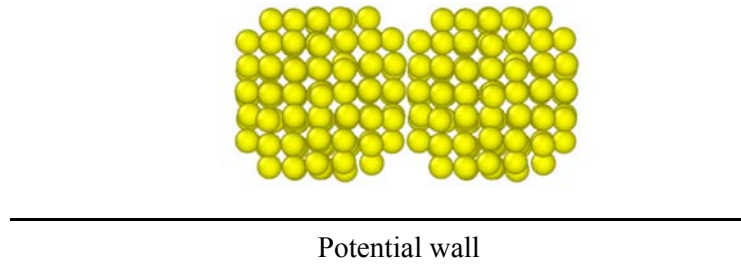
Here, to elucidate the agglomeration of metallic nanoparticles, we consider two AuNPs on a potential wall substrate as shown in Figure 5.29-(a). After 100,000 steps of MD simulations, as shown in Figure 5.29-(c), the two gold nanoparticles agglomerate into one gold nanoparticle which has a similar height and larger width compared to the initial gold nanoparticle.

We verified the developed DSA method for agglomeration problem of AuNPs on the substrate. The accuracy of the developed design sensitivity and second order analytical sensitivity with respect to random and design variables is shown by comparing it to the finite difference sensitivity. The initial velocity of nanoparticles is considered as a random variable and the force field parameters ε and σ between the gold nanoparticles and the 12-6 Lennard-Jones potential wall substrate are considered as design variables. Potential parameters ε and σ are 0.5 (eV) and 3.0 (\AA), respectively.

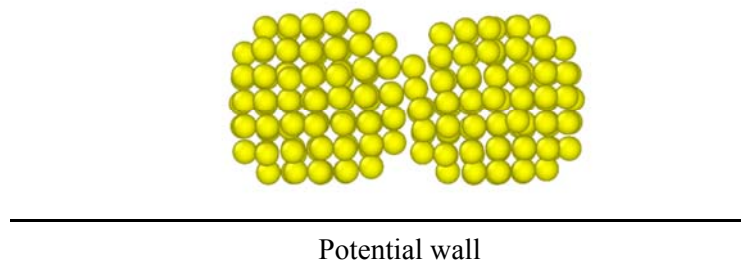
EAM potential is utilized for gold-gold interatomic potential. The desired initial temperature is 300K. The performance measure is the time averaged potential energy of gold nanoparticles in user defined time interval.

Through Table 5.40 to Table 5.41, the developed design sensitivity and second order analytical sensitivity is verified by comparing with finite difference sensitivity or direct differential sensitivity. The time interval to average the potential energy of gold nanoparticles is between 9,000 – 10,000 steps. The MD simulation time is selected when the cold-welding phenomenon just starts as shown in Figure 5.29-(b). In Table 5.40, the accuracy of the developed design sensitivity with respect to the random initial velocity is shown by comparing it to the direct differential sensitivity and the finite difference sensitivity obtained from finite difference method by varying the perturbation amount from 1.e-2 to 1.e-10. In Table 5.41 and Table 5.42, design sensitivity with respect to the design variables, which are ϵ and σ between the gold nanoparticle and the 12-6 Lennard-Jones potential wall substrate, is verified through comparison to direct differential sensitivity and finite difference sensitivity. In most cases, the developed design sensitivity shows good agreement with both finite difference sensitivity and analytical sensitivity. However, again we can see that the accuracy of the FDM sensitivity depends on the perturbation amount.

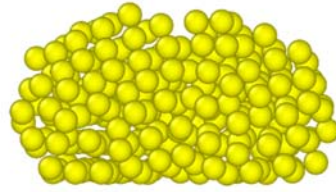
Table 5.43 shows the accuracy of the analytical second order design sensitivity with respect to the random and design variable which are the initial velocity of gold nanoparticles and the interatomic force field parameter ϵ between the gold nanoparticle and the potential wall substrate, respectively. The finite difference sensitivity is obtained by varying the perturbation amount from 1.e-2 to 1.e-12. The FDM second order sensitivity gives very poor accuracy compared to the analytical second order sensitivity. Therefore we can conclude that the developed analytical DSA method works well for the cold-welding problems.



(a) initial model of cold welding problem



(b) after 10,000 steps of MD simulation



Potential wall

(c) after 100,000 steps of MD simulation

Figure 5.29 Cold welding of gold nanoparticles on a potential wall substrate

Table 5.40 Verification of random initial velocity design sensitivity (9,000-10,000 steps)

Perturbation amount	(a) FDM	(b) DDM	(c) AVM	(c)/(a) (%)	(c)/(b) %
1.00E-02	1.9320E-01	2.0248E-01	2.0266E-01	104.8956	100.0900
1.00E-03	1.9978E-01	2.0248E-01	2.0266E-01	101.4424	100.0900
1.00E-04	2.0257E-01	2.0248E-01	2.0266E-01	100.0438	100.0900
1.00E-05	2.0296E-01	2.0248E-01	2.0266E-01	99.8514	100.0900
1.00E-06	2.0248E-01	2.0248E-01	2.0266E-01	100.0903	100.0900
1.00E-07	2.0248E-01	2.0248E-01	2.0266E-01	100.0895	100.0900
1.00E-08	2.0260E-01	2.0248E-01	2.0266E-01	100.0294	100.0900
1.00E-09	2.0191E-01	2.0248E-01	2.0266E-01	100.3729	100.0900
1.00E-10	2.1942E-01	2.0248E-01	2.0266E-01	92.3639	100.0900

Table 5.41 Verification of design variable ε design sensitivity (9,000-10,000 steps)

Perturbation amount	(a) FDM	(b) DDM	(c) AVM	(c)/(a) (%)	(c)/(b) %
1.00E-02	1.0649E+00	1.0596E+00	1.0600E+00	99.5320	100.0308
1.00E-03	1.0615E+00	1.0596E+00	1.0600E+00	99.8582	100.0308
1.00E-04	1.0645E+00	1.0596E+00	1.0600E+00	99.5760	100.0308
1.00E-05	1.0653E+00	1.0596E+00	1.0600E+00	99.5016	100.0308
1.00E-06	1.0596E+00	1.0596E+00	1.0600E+00	100.0307	100.0308
1.00E-07	1.0596E+00	1.0596E+00	1.0600E+00	100.0301	100.0308
1.00E-08	1.0598E+00	1.0596E+00	1.0600E+00	100.0150	100.0308
1.00E-09	1.0600E+00	1.0596E+00	1.0600E+00	99.9946	100.0308
1.00E-10	1.0596E+00	1.0596E+00	1.0600E+00	100.0375	100.0308

Table 5.42 Verification of design variable σ design sensitivity (9,000-10,000 steps)

Perturbation amount	(a) FDM	(b) DDM	(c) AVM	(c)/(a) (%)	(c)/(b) %
1.00E-02	1.9271E+00	2.1582E+00	2.1603E+00	112.0993	100.0940
1.00E-03	2.0855E+00	2.1582E+00	2.1603E+00	103.5863	100.0940
1.00E-04	2.1180E+00	2.1582E+00	2.1603E+00	101.9968	100.0940
1.00E-05	2.0343E+00	2.1582E+00	2.1603E+00	106.1919	100.0940
1.00E-06	2.4774E+00	2.1582E+00	2.1603E+00	87.1974	100.0940
1.00E-07	1.7823E+00	2.1582E+00	2.1603E+00	121.2035	100.0940
1.00E-08	2.1582E+00	2.1582E+00	2.1603E+00	100.0955	100.0940
1.00E-09	2.1599E+00	2.1582E+00	2.1603E+00	100.0149	100.0940
1.00E-10	2.1600E+00	2.1582E+00	2.1603E+00	100.0096	100.0940

Table 5.43 Verification of 2nd order analytical sensitivity (9,000-10,000 steps)

Perturbation amount	(a) FDM	(b) Analytical	(b)/(a) (%)
1.00E-02	2.1251E-01	2.1306E-01	100.2579
1.00E-03	2.0381E-01	2.1346E-01	104.7366
1.00E-04	2.1231E-01	2.1363E-01	100.6245
1.00E-05	-1.9590E-02	2.1363E-01	-1090.4652
1.00E-06	2.1336E-01	2.1363E-01	100.1268
1.00E-07	2.1293E-01	2.1363E-01	100.3260
1.00E-08	2.0711E-01	2.1363E-01	103.1476
1.00E-09	2.1351E-01	2.1363E-01	100.0552
1.00E-10	2.2040E-01	2.1363E-01	96.9277
1.00E-11	1.8401E-01	2.1363E-01	116.0968
1.00E-12	1.1990E-01	2.1363E-01	178.1657

We perform first-order reliability method (FORM) analysis to estimate the effect of random initial velocity to the variance of the performance measure and the sensitivity. The FORM analysis is directly carried out based on the sensitivity analysis from the previous section. The model is the gold nanoparticle on a potential wall substrate. The performance measure is the time averaged gold nanoparticle potential energy between time intervals between 9,000 and 10,000 steps. The uncertainty from random initial velocity is considered by assuming that it follows a normal distribution. The initial velocity of the gold nanoparticle is parameterized random variable \mathbf{X} as $\mathbf{v}(\mathbf{X}) = \mathbf{v}^0 (1 + \mathbf{X})^{\frac{1}{2}}$. The random variable has mean of 0 and the standard deviation of 10^{-2} , $\mathbf{X} \sim N(0, (10^{-2})^2)$. To verify the accuracy of the first-order reliability method analysis, an independent Monte Carlo MD simulation is performed with 1,000 samples for both the performance measure and the

sensitivity.

The histogram of the performance measure and the sensitivity with corresponding normal distribution is shown in Figure 5.30 and Figure 5.31. Table 5.44 shows the comparison between FORM analysis and 1,000 Monte Carlo simulation for the performance measure. ψ and σ are the performance measure and the standard deviation of the performance measure. As we can see, the standard deviation of the performance measure obtained from FORM analysis excellently agrees with 1,000 Monte Carlo simulation results even though the sampling number is relatively small. Furthermore, the performance measure obtained from Monte Carlo simulation agrees well with the performance measure at the mean value of the random initial velocity. This indicates that, by performing a simple first-order reliability method analysis based on the developed design sensitivity, we can easily obtain the standard deviation of the performance measure of interest without tedious repetition of same simulation with different initial condition to insure the reliability of the simulation by standard error analysis. These results indicate that performing FORM analysis based on the developed design sensitivity could accurately and efficiently estimate the variance of the performance measure due to uncertainties in the MD simulation.

Table 5.45 shows the comparison between FORM analysis and 1,000 Monte Carlo simulation for the sensitivity of the performance measure with respect to the random initial velocity. The superscript ()' indicates values of the sensitivity. As shown in the table, we can notice that the FORM analysis using the second order sensitivity to estimate the variance of the sensitivity also works well compared to the Monte Carlo simulation with about 90% agreement. Accuracy slightly decreases in the FORM analysis for the sensitivity compared to the performance measure one. This is because we need to use the second order sensitivity to obtain the variance of the sensitivity in FORM analysis.

Table 5.44 Accuracy of FORM analysis for performance measure

(a) σ_{FORM}	(b) $\sigma_{1,000}$	(b)/(a) (%)	(c) $\psi_{at\ mean}$	(d) $\psi_{1,000}$	(d)/(c) (%)
2.0248E-03	2.0288E-03	100.20	-8.2162E+02	-8.2162E+02	100.00

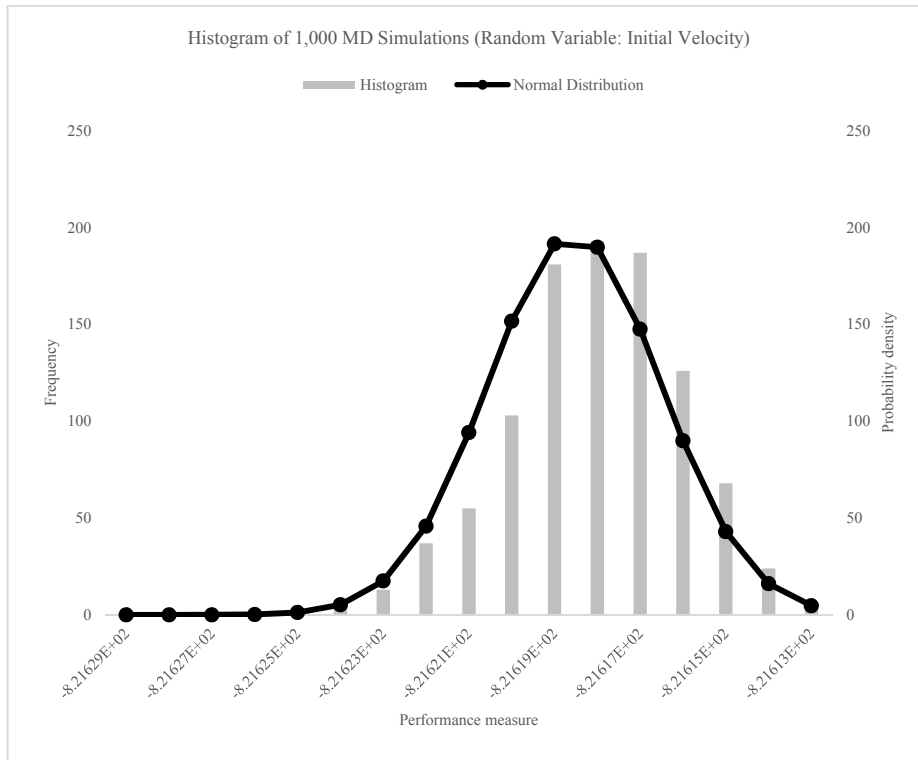


Table 5.45 Accuracy of FORM analysis for sensitivity

(a) σ'_{FORM}	(b) $\sigma'_{1,000}$	(b)/(a) (%)	(c) ψ'_{atmean}	(d) $\psi'_{1,000MC}$	(d)/(c) (%)
2.1363E-03	2.1082E-03	98.68	1.0596E+00	1.0596E+00	100.00

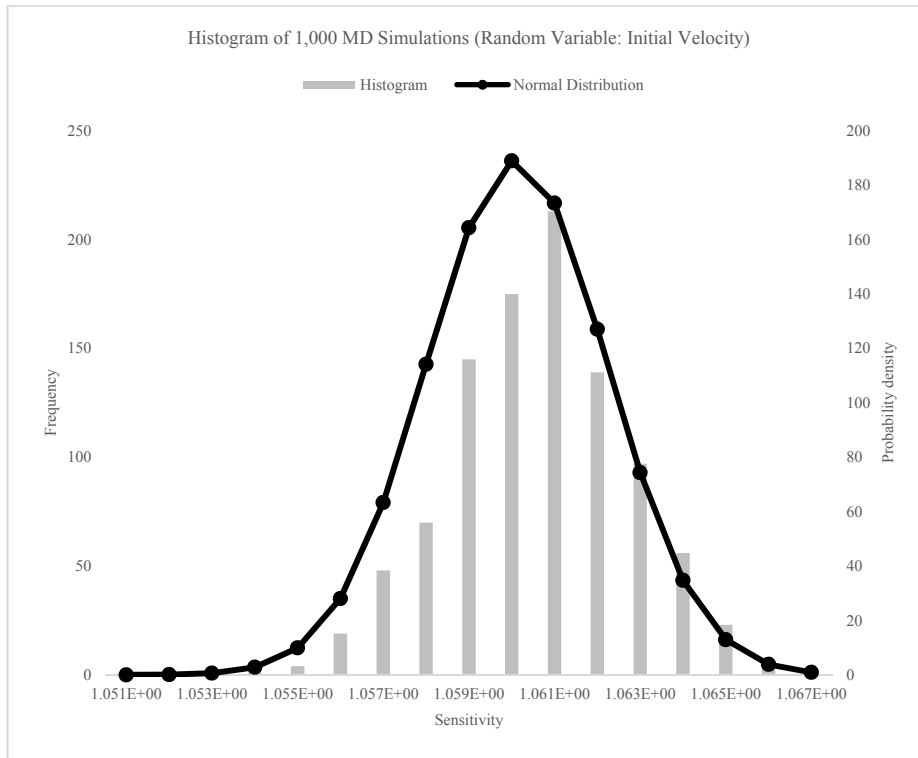


Figure 5.31 Sensitivity histogram of 1,000 MD simulations and its normal distribution graph

The efficiency of FORM analysis based on the developed design sensitivity is shown by comparing the computation time of MD simulation and DSA of MD. In Table 5.46, the normalized computation cost for Monte Carlo simulation and FORM analysis for performance measure and sensitivity is shown. For evaluation of the variance of the performance measure, it only takes 0.11% computation cost for sensitivity based FORM analysis compared to the Monte Carlo simulation. For the evaluation of the impact of uncertainty in DSA of MD it takes only 0.13% computation cost compared to the 1,000 Monte Carlo simulation. This indicates that, since the first order sensitivity with respect to random variable is necessary for calculation of the second order sensitivity, we can simultaneously evaluate the uncertainty effect in both MD simulation and DSA of MD with computation cost about only 1 additional MD simulation.

Table 5.46 Comparison of computational cost

	MC for analysis	FORM for analysis	MC for DSA	FORM for sensitivity
Normalized computation cost	1.00	0.0011	1.00	0.0013

Through Table 5.47 to Table 5.50, design sensitivity analysis results for cold-welding of gold nanoparticles are shown for longer time interval, between 80,000 and 100,000 steps. The MD simulation time is selected when the cold-welding phenomenon is ended as shown in Figure 5.29-(c). Random and design variables are the initial velocity and force field parameters between gold nanoparticles and the substrate, respectively. As we can see from the DSA results, analytical DDM and AVM sensitivities always shows good agreement regardless of the perturbation amount. For the second order sensitivity, as shown in Table 5.48, analytical sensitivity shows converged value independent to the perturbation amount. However, the finite difference sensitivity shows large variance not only for first order but also for second order sensitivity depending on the perturbation amount. Too much or small

perturbation leads to numerical error in finite difference method. This indicates that the accuracy of the sensitivity obtained from finite difference method is not reliable. Therefore, we can conclude that the finite difference sensitivity is improper to be used for sensitivity analysis for designing of nanomaterials.

Table 5.47 Verification of random initial velocity design sensitivity (80,000-100,000 steps)

Perturbation amount	(a) FDM	(b) DDM	(c) AVM	(c)/(a) (%)	(c)/(b) %
1.00E-02	-1.3179E-01	-1.5589E-01	-1.5584E-01	118.2486	99.9695
1.00E-03	-1.2445E-01	-1.5589E-01	-1.5584E-01	125.2223	99.9695
1.00E-04	-1.5650E-01	-1.5589E-01	-1.5584E-01	99.5821	99.9695
1.00E-05	-9.9010E-02	-1.5589E-01	-1.5584E-01	157.4027	99.9695
1.00E-06	-1.3425E-01	-1.5589E-01	-1.5584E-01	116.0807	99.9695
1.00E-07	-1.5592E-01	-1.5589E-01	-1.5584E-01	99.9518	99.9695
1.00E-08	-1.5530E-01	-1.5589E-01	-1.5584E-01	100.3528	99.9695
1.00E-09	-1.5700E-01	-1.5589E-01	-1.5584E-01	99.2628	99.9695
1.00E-10	-1.6939E-01	-1.5589E-01	-1.5584E-01	92.0013	99.9695
1.00E-11	1.0232E-01	-1.5589E-01	-1.5584E-01	-152.3132	99.9695
1.00E-12	-1.9327E+00	-1.5589E-01	-1.5584E-01	8.0636	99.9695

Table 5.48 Verification of design variable ε design sensitivity (80,000-100,000 steps)

Perturbation amount	(a) FDM	(b) DDM	(c) AVM	(c)/(a) (%)	(c)/(b) %
1.00E-02	7.9275E+00	6.6385E+00	6.6405E+00	83.7657	100.0300
1.00E-03	7.7571E+00	6.6385E+00	6.6405E+00	85.6054	100.0300
1.00E-04	7.2749E+00	6.6385E+00	6.6405E+00	91.2795	100.0300
1.00E-05	7.5999E+00	6.6385E+00	6.6405E+00	87.3763	100.0300
1.00E-06	9.8606E+00	6.6385E+00	6.6405E+00	67.3437	100.0300
1.00E-07	6.3164E+00	6.6385E+00	6.6405E+00	105.1322	100.0300
1.00E-08	5.5293E+00	6.6385E+00	6.6405E+00	120.0969	100.0300
1.00E-09	6.6331E+00	6.6385E+00	6.6405E+00	100.1126	100.0300
1.00E-10	6.6507E+00	6.6385E+00	6.6405E+00	99.8473	100.0300
1.00E-11	7.0031E+00	6.6385E+00	6.6405E+00	94.8226	100.0300
1.00E-12	7.0486E+00	6.6385E+00	6.6405E+00	94.2108	100.0300

Table 5.49 Verification of design variable σ design sensitivity (80,000-100,000 steps)

Perturbation amount	(a) FDM	(b) DDM	(c) AVM	(c)/(a) (%)	(c)/(b) %
1.00E-02	2.0325E+01	-7.4047E+00	-7.4094E+00	-36.4542	100.0640
1.00E-03	5.0570E+00	-7.4047E+00	-7.4094E+00	-146.5177	100.0640
1.00E-04	-5.2657E+00	-7.4047E+00	-7.4094E+00	140.7120	100.0640
1.00E-05	-5.2105E+00	-7.4047E+00	-7.4094E+00	142.2014	100.0640
1.00E-06	-6.0854E+00	-7.4047E+00	-7.4094E+00	121.7575	100.0640
1.00E-07	3.9652E+00	-7.4047E+00	-7.4094E+00	-186.8612	100.0640
1.00E-08	-2.4454E+01	-7.4047E+00	-7.4094E+00	30.2996	100.0640
1.00E-09	-7.4100E+00	-7.4047E+00	-7.4094E+00	99.9925	100.0640
1.00E-10	-7.4692E+00	-7.4047E+00	-7.4094E+00	99.1996	100.0640
1.00E-11	-7.2987E+00	-7.4047E+00	-7.4094E+00	101.5173	100.0640
1.00E-12	-7.9581E+00	-7.4047E+00	-7.4094E+00	93.1059	100.0640

Table 5.50 Verification of 2nd order analytical sensitivity (80,000-100,000 steps)

Perturbation amount	(a) FDM	(b) Analytical	(b)/(a) (%)
1.00E-02	5.0351E+04	2.2192E+05	440.8473
1.00E-03	6.4376E+04	2.2192E+05	344.8048
1.00E-04	3.8339E+04	2.2192E+05	578.9715
1.00E-05	1.2755E+05	2.2192E+05	174.0212
1.00E-06	2.1508E+04	2.2192E+05	1032.0577
1.00E-07	3.8224E+05	2.2192E+05	58.0711
1.00E-08	7.1904E+05	2.2192E+05	30.8705
1.00E-09	7.7695E+05	2.2192E+05	28.5698
1.00E-10	2.2934E+05	2.2192E+05	96.7855
1.00E-11	2.6476E+05	2.2192E+05	83.8377
1.00E-12	1.2719E+06	2.2192E+05	17.4520

5.5.3 Reliability based design sensitivity analysis

The failure function is defined as

$$g(\mathbf{b}, \mathbf{X}) = \frac{\psi(\mathbf{b}, \mathbf{X})}{\psi_{fail}} - 1, \quad (5.5.1)$$

where ψ is the time averaged potential energy in the selected interval, between 9,000 and 10,000 steps. ψ_{fail} is the constant which is taken to be $\psi_{fail} = -406.0$ where the performance measure evaluated at the mean value is $\psi(\mathbf{b}, \mathbf{X})|_{\mathbf{b}=\mathbf{0}} \approx -407.76$. The random variables are related to the initial velocity component of all atoms consisting the gold nanoparticle as

$$\mathbf{v}(t=0) = \mathbf{v}^0 \cdot (1 + \mathbf{x}), \quad (5.5.2)$$

where \mathbf{x} is a random variable vector. Therefore, the number of random variables are $n_a \times n_d = 348$, where n_a and n_d are the number of atoms and dimension number, respectively. Same procedure is performed as the previous 1-dimensional harmonic oscillator problem. First, we find the MPP point utilizing the MMFD algorithm. The gradient of 348 random variables are obtained from adjoint DSA efficiently. And then the sensitivity of reliability index β with respect to the design variable ε of the potential wall is evaluated at the MPP. For the FDM, same sub-optimization problem is solved from the perturbed design variables, ε and σ . Since the limit state function is highly nonlinear, the FDM sensitivity is sensitive with respect to the parameters for optimization algorithm as shown in Table 5.51.

Table 5.51 Verification of β sensitivity ($\Delta b = 10^{-9}$ for FDM)

	perturbed	original	(a) FDM	(b) AVM	(b)/(a) (%)
ε	1.1526E+00	1.1526E+00	4.4080E-02	4.2164E-02	95.65
σ	1.1526E+00	1.1526E+00	5.8205E-01	5.4571E-01	93.76

Chapter 6. Conclusions and Future Works

6.1 Conclusions

A design sensitivity analysis method considering ensemble and potential parameter uncertainty using MD simulation for nanomaterials is developed. By utilizing the FORM concept based on the developed design sensitivity, we suggest an efficient and accurate method to evaluate the uncertainty effect to both MD simulation and DSA of MD. For applications to practical nanoscale design problems of various nanomaterials, a constant temperature MD simulation is considered by using Nose-Hoover thermostat.

Uncertainty have a significant impact on observations and predictions in both MD simulation and design sensitivity of nanomaterials. We identify the origin of uncertainty as ensemble and potential parameters. The uncertainty from ensemble parameters is inherently present in atomistic systems due to the random initial velocities. The potential parameter uncertainty arises when some parameters defining the interatomic interactions in MD simulations are unknown. By utilizing the first-order reliability method based on the developed analytical first and second order sensitivities with respect to random and design variables, the effect of uncertainty to MD simulation and DSA of MD is efficiently and accurately evaluated.

Developed DSA method is applied to investigate the behavior of agglomeration phenomenon of nanoparticles on a substrate which is observed in experiments. Furthermore, a design optimization is performed based on the developed sensitivity to find unknown interatomic potential parameters between the nanoparticle and the substrate. Consequently, we achieve efficiency in MD simulation of nanoparticle and substrate problem by replacing the complex substrate to simple potential wall.

6.2 Future works

As an extension to this thesis, future studies include the following:

- (1) In this research, we developed a DSA method for nanomaterials considering uncertainty from ensemble and potential parameters. The developed method is applicable for various pair and many-body potentials. However, for further extension to the design of various nanomaterials, nanocomposites, biomolecules and to correlate with experiments, a development of DSA method considering bond, angle, and dihedral forces is necessary.
- (2) In the experimental environment, not only the temperature but also the pressure of the system plays a significant role. For a comparative study of experiment and MD simulation to design nanomaterials, a development of DSA method under isothermal-isobaric (NPT) ensemble is essential. Furthermore, to reproduce the aqueous environment in experiment, the effect from water molecules also need to be taken into account.

Bibilography

- ALFREDO, H.-S. A. & WILSON, H. 1975. Probability concepts in engineering planning and design. *John Wily and Sons*.
- ANDERSEN, H. C. 1980. Molecular dynamics simulations at constant pressure and/or temperature. *The Journal of chemical physics*, 72, 2384-2393.
- BERBER, S., KWON, Y.-K. & TOMANEK, D. 2000. Unusually high thermal conductivity of carbon nanotubes. *Physical review letters*, 84, 4613.
- BERENDSEN, H. J., POSTMA, J. P. M., VAN GUNSTEREN, W. F., DINOLA, A. & HAAK, J. 1984. Molecular dynamics with coupling to an external bath. *The Journal of chemical physics*, 81, 3684-3690.
- CAI, W., DE KONING, M., BULATOV, V. V. & YIP, S. 2000. Minimizing boundary reflections in coupled-domain simulations. *Physical Review Letters*, 85, 3213.
- CERIOTTI, M., BUSSI, G. & PARRINELLO, M. 2009. Langevin equation with colored noise for constant-temperature molecular dynamics simulations. *Physical review letters*, 102, 020601.
- CHAKRABORTY, S., JOSHI, P., SHANKER, V., ANSARI, Z., SINGH, S. P. & CHAKRABARTI, P. 2011. Contrasting effect of gold nanoparticles and nanorods with different surface modifications on the structure and activity of bovine serum albumin. *Langmuir*, 27, 7722-7731.
- CHANG, W.-J. & FANG, T.-H. 2003. Influence of temperature on tensile and fatigue behavior of nanoscale copper using molecular dynamics simulation. *Journal of Physics and Chemistry of Solids*, 64, 1279-1283.
- CHO, S. & CHOI, K. 2000a. Design sensitivity analysis and optimization of non-linear transient dynamics. Part I—sizing design. *International Journal for Numerical Methods in Engineering*, 48, 351-373.
- CHO, S. & CHOI, K. 2000b. Design sensitivity analysis and optimization of non-linear transient dynamics. Part II—configuration design. *International Journal for Numerical Methods in Engineering*, 48, 375-399.
- CHOI, K. K. & KIM, N. H. 2006a. *Structural Sensitivity Analysis and Optimization 1: Linear Systems*, Springer.

- CHOI, K. K. & KIM, N. H. 2006b. *Structural Sensitivity Analysis and Optimization 2: Nonlinear Systems and Applications*, Springer.
- CORNELL, C. A. A probability-based structural code*. ACI Journal Proceedings, 1969. ACI.
- DAW, M. S., FOILES, S. M. & BASKES, M. I. 1993. The embedded-atom method: a review of theory and applications. *Materials Science Reports*, 9, 251-310.
- DITLEVSEN, O. & MADSEN, H. O. 1996. *Structural reliability methods*, Wiley New York.
- DREADEN, E. C., MACKEY, M. A., HUANG, X., KANG, B. & EL-SAYED, M. A. 2011. Beating cancer in multiple ways using nanogold. *Chemical Society Reviews*, 40, 3391-3404.
- E, W. & HUANG, Z. 2001. Matching Conditions in Atomistic-Continuum Modeling of Materials. *Physical Review Letters*, 87.
- E, W. & HUANG, Z. 2002. A Dynamic Atomistic–Continuum Method for the Simulation of Crystalline Materials. *Journal of Computational Physics*, 182, 234-261.
- EVSTIGNEEV, M. & REIMANN, P. 2010. Langevin equation for a system nonlinearly coupled to a heat bath. *Physical Review B*, 82, 224303.
- FOILES, S., BASKES, M. & DAW, M. 1986. Embedded-atom-method functions for the fcc metals Cu, Ag, Au, Ni, Pd, Pt, and their alloys. *Physical Review B*, 33, 7983-7991.
- FRENKEL, D. & SMIT, B. 2001. *Understanding Molecular Simulation: From Algorithms to Applications*, Elsevier Science.
- FREUDENTHAL, A. M. 1956. Safety and the probability of structural failure. *American Society of Civil Engineers Transactions*.
- FU, B., CHEN, N., XIE, Y., YE, X. & GU, X. 2013. Size and temperature dependence of the tensile mechanical properties of zinc blende CdSe nanowires. *Physics Letters A*, 377, 2681-2686.
- FUJII, M., ZHANG, X., XIE, H., AGO, H., TAKAHASHI, K., IKUTA, T., ABE, H. & SHIMIZU, T. 2005. Measuring the Thermal Conductivity of a Single Carbon Nanotube. *Physical Review Letters*, 95.
- GAGNER, J. E., LOPEZ, M. D., DORDICK, J. S. & SIEGEL, R. W. 2011. Effect of gold nanoparticle morphology on adsorbed protein structure and function. *Biomaterials*, 32, 7241-7252.
- GAO, Z., MA, Y. & ZHUANG, H. 2008. Optimal shape design for the time-dependent Navier–Stokes flow. *International journal for numerical methods in fluids*, 57, 1505-1526.
- HASOFER, A. 1974. Reliability index and failure probability. *Journal*

- of Structural Mechanics*, 3, 25-27.
- HASOFER, A. M. & LIND, N. C. 1974. Exact and invariant second-moment code format. *Journal of the Engineering Mechanics division*, 100, 111-121.
- HIRANO, A., KAMEDA, T., SHINOZAKI, D., ARAKAWA, T. & SHIRAKI, K. 2013. Molecular dynamics simulation of the arginine-assisted solubilization of caffeic acid: intervention in the interaction. *J Phys Chem B*, 117, 7518-27.
- HOCKNEY, R. W. & EASTWOOD, J. W. 1988. *Computer simulation using particles*, Taylor & Francis, Inc.
- HOLIAN, B. L. & RAVELO, R. 1995. Fracture simulations using large-scale molecular dynamics. *Physical Review B*, 51, 11275.
- HONE, J., LLAGUNO, M., NEMES, N., JOHNSON, A., FISCHER, J., WALTERS, D., CASAVANT, M., SCHMIDT, J. & SMALLEY, R. 2000. Electrical and thermal transport properties of magnetically aligned single wall carbon nanotube films. *Applied Physics Letters*, 77, 666-668.
- HONE, J., WHITNEY, M., PISKOTI, C. & ZETTL, A. 1999. Thermal conductivity of single-walled carbon nanotubes. *Physical Review B*, 59, R2514.
- HOOVER, W. G. 1985. Canonical dynamics: equilibrium phase-space distributions. *Physical Review A*, 31, 1695.
- HSIEH, C. & ARORA, J. 1984. Design sensitivity analysis and optimization of dynamic response. *Computer methods in applied mechanics and engineering*, 43, 195-219.
- HU, Y. & SINNOTT, S. B. 2004. Constant temperature molecular dynamics simulations of energetic particle–solid collisions: comparison of temperature control methods. *Journal of Computational Physics*, 200, 251-266.
- HUANG, D., ZHANG, Q. & QIAO, P. 2011. Molecular dynamics evaluation of strain rate and size effects on mechanical properties of FCC nickel nanowires. *Computational Materials Science*, 50, 903-910.
- HULKOTI, N. I. & TARANATH, T. 2014. Biosynthesis of nanoparticles using microbes—a review. *Colloids and Surfaces B: Biointerfaces*, 121, 474-483.
- HUMPHREY, W., DALKE, A. & SCHULTEN, K. 1996. VMD: visual molecular dynamics. *Journal of molecular graphics*, 14, 33-38.
- IJIMA, S. 1991. Helical microtubules of graphitic carbon. *nature*, 354, 56-58.
- JAKALIAN, A., JACK, D. B. & BAYLY, C. I. 2002. Fast, efficient

- generation of high-quality atomic charges. AM1-BCC model: II. Parameterization and validation. *J Comput Chem*, 23, 1623-41.
- JIANG, S., ZHANG, H., ZHENG, Y. & CHEN, Z. 2009. Atomistic study of the mechanical response of copper nanowires under torsion. *Journal of Physics D: applied physics*, 42, 135408.
- JONES, J. E. 1924a. On the Determination of Molecular Fields. II. From the Equation of State of a Gas. *Proceedings of the Royal Society of London. Series A, Containing Papers of a Mathematical and Physical Character*, 106, 463-477.
- JONES, J. E. 1924b. On the Determination of Molecular Fields. I. From the Variation of the Viscosity of a Gas with Temperature. *Proceedings of the Royal Society of London. Series A, Containing Papers of a Mathematical and Physical Character*, 106, 441-462.
- KARPOV, E. G., WAGNER, G. J. & LIU, W. K. 2005. A Green's function approach to deriving non-reflecting boundary conditions in molecular dynamics simulations. *International Journal for Numerical Methods in Engineering*, 62, 1250-1262.
- KAUR, K. & FORREST, J. A. 2012. Influence of particle size on the binding activity of proteins adsorbed onto gold nanoparticles. *Langmuir*, 28, 2736-2744.
- KIM, M.-G., JANG, H.-L. & CHO, S. 2013a. Adjoint design sensitivity analysis of reduced atomic systems using generalized Langevin equation for lattice structures. *Journal of Computational Physics*, 240, 1-19.
- KIM, M., JANG, H., KIM, H. & CHO, S. 2013b. Multiscale adjoint design sensitivity analysis of atomistic-continuum dynamic systems using bridging scale decomposition. *Modelling and Simulation in Materials Science and Engineering*, 21, 035005.
- KIM, P., SHI, L., MAJUMDAR, A. & MCEUEN, P. 2001. Thermal Transport Measurements of Individual Multiwalled Nanotubes. *Physical Review Letters*, 87.
- KOH, S., LEE, H., LU, C. & CHENG, Q. 2005. Molecular dynamics simulation of a solid platinum nanowire under uniaxial tensile strain: Temperature and strain-rate effects. *Physical Review B*, 72.
- LEITCH, R. D. 1995. *Reliability analysis for engineers: an introduction*, Oxford University Press New York.
- LI, X. & WEINAN, E. 2005. Variational boundary conditions for molecular dynamics simulations of solids at low temperature.
- LIANG, W. & ZHOU, M. 2004. Response of copper nanowires in

- dynamic tensile deformation. *Proceedings of the Institution of Mechanical Engineers, Part C: Journal of Mechanical Engineering Science*, 218, 599-606.
- LIANG, W. & ZHOU, M. 2005. Pseudoelasticity of Single Crystalline Cu Nanowires Through Reversible Lattice Reorientations. *Journal of Engineering Materials and Technology*, 127, 423.
- LU, L., LI, S. & LU, K. 2001. An abnormal strain rate effect on tensile behavior in nanocrystalline copper. *Scripta Materialia*, 45, 1163-1169.
- LU, Y., HUANG, J. Y., WANG, C., SUN, S. & LOU, J. 2010. Cold welding of ultrathin gold nanowires. *Nature Nanotechnology*, 5, 218-224.
- MADSEN, H. O., KRENK, S. & LIND, N. C. 1986. *Methods of structural safety*, New Jersey, Prentice-Hall.
- MARTINEZ, L., ANDRADE, R., BIRGIN, E. G. & MARTINEZ, J. M. 2009. PACKMOL: a package for building initial configurations for molecular dynamics simulations. *J Comput Chem*, 30, 2157-64.
- MARTYNA, G. J., KLEIN, M. L. & TUCKERMAN, M. 1992. Nosé-Hoover chains: the canonical ensemble via continuous dynamics. *The Journal of chemical physics*, 97, 2635-2643.
- MERABIA, S., SHENOGIN, S., JOLY, L., KEBLINSKI, P. & BARRAT, J.-L. 2009. Heat transfer from nanoparticles: A corresponding state analysis. *Proceedings of the National Academy of Sciences*, 106, 15113-15118.
- NOSE, S. 1984a. A molecular dynamics method for simulations in the canonical ensemble. *Molecular physics*, 52, 255-268.
- NOSE, S. 1984b. A unified formulation of the constant temperature molecular dynamics methods. *The Journal of Chemical Physics*, 81, 511-519.
- PAL, S., TAK, Y. K. & SONG, J. M. 2007. Does the antibacterial activity of silver nanoparticles depend on the shape of the nanoparticle? A study of the gram-negative bacterium *Escherichia coli*. *Applied and environmental microbiology*, 73, 1712-1720.
- PARK, H. & JI, C. 2006. On the thermomechanical deformation of silver shape memory nanowires. *Acta Materialia*, 54, 2645-2654.
- PARK, H. & ZIMMERMAN, J. 2005. Modeling inelasticity and failure in gold nanowires. *Physical Review B*, 72.
- PARK, H. S., KARPOV, E. G., LIU †, W. K. & KLEIN, P. A. 2005. The

- bridging scale for two-dimensional atomistic/continuum coupling. *Philosophical Magazine*, 85, 79-113.
- PARK, M. V., NEIGH, A. M., VERMEULEN, J. P., DE LA FONTEYNE, L. J., VERHAREN, H. W., BRIED, J. J., VAN LOVEREN, H. & DE JONG, W. H. 2011a. The effect of particle size on the cytotoxicity, inflammation, developmental toxicity and genotoxicity of silver nanoparticles. *Biomaterials*, 32, 9810-9817.
- PARK, Y., HONG, Y., WEYERS, A., KIM, Y. & LINHARDT, R. 2011b. Polysaccharides and phytochemicals: a natural reservoir for the green synthesis of gold and silver nanoparticles. *Nanobiotechnology, IET*, 5, 69-78.
- PEREIRA, Z. S. & DA SILVA, E. Z. 2011. Cold Welding of Gold and Silver Nanowires: A Molecular Dynamics Study. *The Journal of Physical Chemistry C*, 115, 22870-22876.
- PLIMPTON, S. 1995. Fast parallel algorithms for short-range molecular dynamics. *Journal of computational physics*, 117, 1-19.
- POP, E., MANN, D., WANG, Q., GOODSON, K. & DAI, H. 2005. Thermal Conductance of an Individual Single-Wall Carbon Nanotube above Room Temperature. *Nano Letters*, 6, 96-100.
- PRICE, D. J. & BROOKS, C. L., 3RD 2004. A modified TIP3P water potential for simulation with Ewald summation. *J Chem Phys*, 121, 10096-103.
- RIZZI, F., NAJM, H., DEBUSSCHERE, B., SARGSYAN, K., SALLOUM, M., ADALSTEINSSON, H. & KNIO, O. 2012. Uncertainty quantification in MD simulations. Part I: Forward propagation. *Multiscale Modeling & Simulation*, 10, 1428-1459.
- ROBERT, E. 1999. Structural reliability analysis and prediction. *Baffins Lane, Chichester, West Sussex, England: Wiley*.
- RYCKAERT, J.-P., CICCOTTI, G. & BERENDSEN, H. J. 1977. Numerical integration of the cartesian equations of motion of a system with constraints: molecular dynamics of *n*-alkanes. *Journal of Computational Physics*, 23, 327-341.
- SEKHON, B. S. & KAMBOJ, S. R. 2010. Inorganic nanomedicine—part 2. *Nanomedicine: Nanotechnology, Biology and Medicine*, 6, 612-618.
- SEVIK, C., SEVIN LI, H., CUNIBERTI, G. & CAGIN, T. 2011. Phonon engineering in carbon nanotubes by controlling defect concentration. *Nano letters*, 11, 4971-4977.
- SHINOZUKA, M. 1983. Basic analysis of structural safety. *Journal of*

- Structural Engineering*, 109, 721-740.
- SLATER, J. C. 1964. Atomic radii in crystals. *The Journal of Chemical Physics*, 41, 3199-3204.
- SPERLING, R. A., GIL, P. R., ZHANG, F., ZANELLA, M. & PARAK, W. J. 2008. Biological applications of gold nanoparticles. *Chemical Society Reviews*, 37, 1896-1908.
- SUTRAKAR, V. K. & MAHAPATRA, D. R. 2009. Coupled effect of size, strain rate, and temperature on the shape memory of a pentagonal Cu nanowire. *Nanotechnology*, 20, 045701.
- TERSOFF, J. 1986. New empirical model for the structural properties of silicon. *Physical Review Letters*, 56, 632-635.
- TERSOFF, J. 1988a. New empirical approach for the structure and energy of covalent systems. *Physical Review B*, 37, 6991-7000.
- TERSOFF, J. 1988b. Empirical Interatomic Potential for Carbon, with Applications to Amorphous Carbon. *Physical Review Letters*, 61, 2879-2882.
- TOBIAS, D. J., MARTYNA, G. J. & KLEIN, M. L. 1993. Molecular dynamics simulations of a protein in the canonical ensemble. *The Journal of Physical Chemistry*, 97, 12959-12966.
- TORTORELLI, D. A., HABER, R. B. & LU, S. C. 1989. Design sensitivity analysis for nonlinear thermal systems. *Computer Methods in Applied Mechanics and Engineering*, 77, 61-77.
- TSAY, J. & ARORA, J. 1990. Nonlinear structural design sensitivity analysis for path dependent problems. Part 1: General theory. *Computer Methods in Applied Mechanics and Engineering*, 81, 183-208.
- TUCKERMAN, M. E., LIU, Y., CICCOTTI, G. & MARTYNA, G. J. 2001. Non-Hamiltonian molecular dynamics: Generalizing Hamiltonian phase space principles to non-Hamiltonian systems. *The Journal of Chemical Physics*, 115, 1678-1702.
- USERS MANUAL, D. O. T. 1995. *Vanderplaats Research & Development. Inc. Version*, 4, 20.
- WAGNER, G. J., KARPOV, E. G. & LIU, W. K. 2004. Molecular dynamics boundary conditions for regular crystal lattices. *Computer Methods in Applied Mechanics and Engineering*, 193, 1579-1601.
- WAGNER, G. J. & LIU, W. K. 2003. Coupling of atomistic and continuum simulations using a bridging scale decomposition. *Journal of Computational Physics*, 190, 249-274.
- WANG, J., WANG, W., KOLLMAN, P. A. & CASE, D. A. 2006. Automatic atom type and bond type perception in molecular

- mechanical calculations. *J Mol Graph Model*, 25, 247-60.
- WANG, J., WOLF, R. M., CALDWELL, J. W., KOLLMAN, P. A. & CASE, D. A. 2004. Development and testing of a general amber force field. *Journal of computational chemistry*, 25, 1157-1174.
- WANG, W.-D., YI, C.-L. & FAN, K.-Q. 2013. Molecular dynamics study on temperature and strain rate dependences of mechanical tensile properties of ultrathin nickel nanowires. *Transactions of Nonferrous Metals Society of China*, 23, 3353-3361.
- WANG, X., YANG, D.-P., HUANG, P., LI, M., LI, C., CHEN, D. & CUI, D. 2012. Hierarchically assembled Au microspheres and sea urchin-like architectures: formation mechanism and SERS study. *Nanoscale*, 4, 7766-7772.
- WEN, Y.-H., ZHU, Z.-Z. & ZHU, R.-Z. 2008. Molecular dynamics study of the mechanical behavior of nickel nanowire: Strain rate effects. *Computational Materials Science*, 41, 553-560.
- WHITESIDES, G. M. & BONCHEVA, M. 2002. Beyond molecules: Self-assembly of mesoscopic and macroscopic components. *Proceedings of the National Academy of Sciences*, 99, 4769-4774.
- YEBRA, D. M., KIIL, S. & DAM-JOHANSEN, K. 2004. Antifouling technology—past, present and future steps towards efficient and environmentally friendly antifouling coatings. *Progress in organic coatings*, 50, 75-104.
- YEH, Y.-C., CRERAN, B. & ROTELLO, V. M. 2012. Gold nanoparticles: preparation, properties, and applications in bionanotechnology. *Nanoscale*, 4, 1871-1880.
- YU, C., JANG, W., HANRATH, T., KIM, D., YAO, Z., KORGEL, B., SHI, L., WANG, Z. L., LI, D. & MAJUMDAR, A. Thermal and thermoelectric measurements of low dimensional nanostructures. ASME 2003 Heat Transfer Summer Conference, 2003. American Society of Mechanical Engineers, 77-82.
- YU, C., SHI, L., YAO, Z., LI, D. & MAJUMDAR, A. 2005. Thermal Conductance and Thermopower of an Individual Single-Wall Carbon Nanotube. *Nano Letters*, 5, 1842-1846.
- ZHU, L. & LI, B. 2014. Low thermal conductivity in ultrathin carbon nanotube (2, 1). *Scientific reports*, 4.

양상불과 포텐셜 변수들의 불확실성을 고려한 나노재료의 설계민감도 해석

김 현 석

산업 · 조선공학부

공과대학

서울대학교

초 록

본 연구에서는 양상불과 포텐셜 변수들의 불확실성을 고려하여 분자동역학 (molecular dynamics)을 이용한 나노재료의 설계민감도 해석 방법론을 개발하였다. 불확실성을 고려한 설계민감도를 바탕으로 하는 1차 신뢰성 방법 (First-Order Reliability Method)의 개념을 도입하여 불확실성이 분자동역학 해석과 그 설계민감도 해석에 미치는 영향을 효율적이고 정확하게 분석하였다. 실제적인 나노스케일에서의 문제에의 적용을 위해 노제-후버 온도 조절 장치 (Nose-Hoover thermostat)을 이용한 항온 분자동역학 전산모사를 수행하였다.

최근 조선해양공학 분야의 전반에서는 기존 연속체 기반 해석법의 한계를 뛰어넘고자 분자 레벨에서의 해석과 설계에 대한 연구가 활발하게 진행되고 있다. 나노스케일에서의 동적 그리고 열역학적 특성을 실험을 통해 관측하는 것은 매우 어렵거나 불가능하다. 하지만, 분자동역학 전산모사는 분자 레벨에서 물리적으로 복잡한 현상들의 이해에 있어 적합한 프레임워크 (framework)를 제공한다. 분자동역학 전산모사에서 불확실성의 영향은 잘 알려져 있다. 이러

한 불확실성은 앙상블 (ensemble) 과 포텐셜 (potential) 변수들에서 기인한다. 앙상블 변수로부터의 불확실성은 임의의 초기 속도에 따라 발생한다. 포텐셜 변수에 의한 불확실성은 분자동역학 전산모사에서 분자 간 포텐셜이 알려져 있지 않음에 따라 발생한다. 기존에는 이러한 불확실성에 따른 영향을 초기 속도 조건 또는 포텐셜 변수들을 바꿔가면서 반복적인 분자동역학 해석을 통해 분석하였다.

이러한 불확실성이 분자동역학 전산모사와 설계민감도 해석에서 미치는 영향을 개발한 설계민감도 바탕의 일차신뢰성방법을 활용하여 효율적이고 정확하게 분석하였다. 분자동역학 전산모사에서 설계민감도 해석에는 효율성과 정확성을 위해 분석적인(analytical) 설계민감도 해석기법을 적용하였다. 유한차분법과 같은 근사화된 설계민감도 해석법은 비선형성이 높은 설계 변수들을 포함하는 분자동역학 전산모사에서 그 정확성과 효율성을 보장하기 힘들다.

나노 재료는 조선해양분야뿐만 아니라 다양한 분야에서 그 활용도가 매우 높다. 본문에 수록한 예제들을 통해 다양한 나노 재료들에 대하여 개발한 불확실성을 고려한 설계민감도 해석기법을 적용하였고, 분자동역학 전산모사와 그 설계민감도에서 불확실성의 영향을 분석하였다. 또한 나노입자와 나노구조물 사이의 알려지지 않은 포텐셜 변수들을 찾기 위해 설계민감도를 바탕으로 한 최적 설계를 수행하였고 의미 있는 결과를 얻을 수 있었다.

주요어: 분자동역학, 앙상블 불확실성, 포텐셜 불확실성, 나노재료, 설계민감도 해석, 최적설계

학번: 2008-21214